JOURNAL OF GEOPHYSICAL RESEARCH, VOL. 114, B12203, doi:10.1029/2008JB006186, 2009

An assessment of upper mantle heterogeneity based on abyssal peridotite isotopic compositions

J. M. Warren,[1,2] N. Shimizu,[3] C. Sakaguchi,[4] H. J. B. Dick,[3] and E. Nakamura[4]

Received 2 November 2008; revised 11 July 2009; accepted 7 August 2009; published 17 December 2009.

[1] Abyssal peridotites, the depleted solid residues of ocean ridge melting, are the most direct samples available to assess upper oceanic mantle composition. We present detailed isotope and trace element analyses of pyroxene mineral separates from Southwest Indian Ridge abyssal peridotites and pyroxenites in order to constrain the size and length scale of mantle heterogeneity. Our results demonstrate that the mantle can be highly heterogeneous to <1 km and even <0.1 m length scales. Examination of Nd isotopes in relation to modal, trace, and major element compositions indicate that the length scales and amplitudes of heterogeneities in abyssal peridotites reflect both ancient mantle heterogeneity and recent modification by melting, melt-rock reaction and melt crystallization. The isotopic and trace element compositions of pyroxenite veins in this study indicate that they are not direct remnants of recycled oceanic crust, but instead are formed by recent melt crystallization. Combined with existing data sets, the results show that the average global isotopic composition of peridotites is similar to that of mid-ocean ridge basalts, though peridotites extend to significantly more depleted $^{143}Nd/^{144}Nd$ and $^{87}Sr/^{86}Sr$. Standard isotope evolution models of upper mantle composition do not predict the full isotopic range observed among abyssal peridotites, as they do not account adequately for the complexities of ancient and recent melting processes.

Citation: Warren, J. M., N. Shimizu, C. Sakaguchi, H. J. B. Dick, and E. Nakamura (2009), An assessment of upper mantle heterogeneity based on abyssal peridotite isotopic compositions, *J. Geophys. Res.*, *114*, B12203, doi:10.1029/2008JB006186.

1. Introduction

[2] The mantle is the largest geochemical reservoir on the planet; its compositional heterogeneities are of fundamental importance to understanding mantle dynamics and long-term evolution of the Earth's interior. In this study, we use abyssal peridotites to assess the amplitudes and length scales of chemical and isotopic heterogeneities within the upper mantle. Abyssal peridotites are the depleted solid residues of mantle melting that are exposed on the seafloor at ocean ridges. Due to their geochemically depleted character and the scarcity of seafloor samples, abyssal peridotites have been under utilized as tracers of mantle composition and evolution. However, recent sampling of peridotites from ultraslow spreading ridges [e.g., *Dick et al.*, 2003], combined with improved analytical techniques, increasingly allow the mantle to be studied from the perspective of the solid residue, in addition to that of basaltic melts.

[3] Studies of radiogenic isotope ratios in basalts from mid-ocean ridges (MORB) and ocean islands (OIB) have found that basalts are highly variable [e.g., *Hart et al.*, 1973; *Hart*, 1984; *Meyzen et al.*, 2007], demonstrating that chemical heterogeneity in the mantle has persisted for long periods of time and indicating that convective mixing of the mantle is relatively inefficient at removing heterogeneities [e.g., *Zindler and Hart*, 1986]. Ranges in isotopic compositions for individual systems (such as a given OIB suite or a specific mid-ocean ridge segment) have led to debate over the form and size of the distinct mantle reservoirs involved. A still significant gap exists between observational geochemistry and numerical models of mantle dynamics [e.g., *van Keken et al.*, 2002], partly because geochemical observations of the length scales and amplitudes of chemical and isotopic heterogeneities in the mantle are inadequate. At small length scales, basalts effectively "smooth-out" heterogeneities, as they are mixtures of melt fractions derived from large areas of the mantle that have undergone variable degrees of melting. Nevertheless, basalts from individual dredges at some mid-ocean ridge localities reveal significant variations in isotopic compositions, suggesting that high-amplitude heterogeneities exist at length scales <2 km [*Dosso et al.*, 1999]. Large variations in Pb isotopic compositions among olivine-hosted melt inclusions from individual MORB and OIB samples [*Saal et al.*, 1998; *Shimizu and Layne*, 2003; *Kobayashi et al.*, 2004; *Shimizu et al.*, 2005; *Maclennan*, 2008] provide additional clear evidence for the existence of higher-amplitude heterogeneities at small length scales.

[1] MIT/WHOI Joint Program, Woods Hole Oceanographic Institution, Woods Hole, Massachusetts, USA.
[2] Now at Department of Terrestrial Magnetism, Carnegie Institution of Washington, Washington, D. C., USA.
[3] Department of Geology and Geophysics, Woods Hole Oceanographic Institution, Woods Hole, Massachusetts, USA.
[4] Institute for Study of the Earth's Interior, Okayama University at Misasa, Misasa, Japan.

0148-0227/09/2008JB006186$09.00

[4] As the solid residues of melting, abyssal peridotites are ideal for looking at scales and amplitudes of mantle heterogeneity, as well as the lithological identities of heterogeneities. Abyssal peridotites are among the few direct samples available of the Earth's interior, providing a window into the oceanic upper mantle. While they come from the uppermost extreme of the subaxial melting regime, their isotopic composition should reflect preexisting variations in asthenospheric mantle composition. In addition, at ultraslow upwelling rates (equivalent to <20 mm/yr full ridge spreading rate), conductive cooling limits mantle melting [*Sleep*, 1975; *Reid and Jackson*, 1981; *Bown and White*, 1994; *Dick et al.*, 2003]. Hence, peridotites exposed on the seafloor at ultraslow ridges, such as the Southwest Indian Ridge (SWIR) and Gakkel Ridge, are expected to have experienced limited degrees of melting. Thus, ultraslow spreading peridotites should represent the closest approach to asthenospheric mantle composition.

[5] Previous studies of abyssal peridotites have demonstrated that the mantle is highly heterogeneous in some regions, similar to conclusions reached from basalts. Major element and mineralogical variations in peridotites from the easternmost SWIR have been interpreted as indicating initial mantle heterogeneity, consisting of refractory peridotite with some fertile regions [*Seyler et al.*, 2003, 2004]. Osmium isotopic data of bulk peridotites from the Gakkel Ridge and the Mid-Atlantic Ridge (MAR) also indicate heterogeneous mantle, some of which has undergone ancient depletion events [*Brandon et al.*, 2000; *Liu et al.*, 2008]. *Harvey et al.* [2006] found considerable osmium isotopic heterogeneity among individual sulfide grains from a MAR peridotite, indicating a component of ancient depletion. However, as the majority of Os is hosted in sulfides in peridotites [*Burton et al.*, 1999], constraints on long-term evolution of the silicate mantle are best provided by Nd and Sr isotopes.

[6] Due to hydrothermal alteration and the geochemically depleted character of abyssal peridotites, Nd and Sr radiogenic isotope data have been collected in only four previous studies: *Snow et al.* [1994], *Kempton and Stephens* [1997], *Salters and Dick* [2002], and *Cipriani et al.* [2004]. These studies attempted to reconcile the isotopic composition of peridotites to regionally associated basalts, generally over length scales of 10–1000 km. From analysis of SWIR peridotites, *Salters and Dick* [2002] suggested that a "missing" pyroxenite component is present in the mantle, in order to explain differences in the isotopic compositions of peridotites and basalts. In contrast, *Snow et al.* [1994] and *Cipriani et al.* [2004] concluded that the isotopic range of MORBs is matched by the peridotite isotopic range. In addition, *Cipriani et al.* [2004] found small-scale (<10 km) Nd isotopic heterogeneity, which they related to recent melt-rock reaction with enriched melts.

[7] In this study, we present a detailed analysis of Nd and Sr isotope variations at the subdredge and subsample scales, to constrain the origin of compositional anomalies in the mantle. The present study is different from previous abyssal peridotite studies in two important ways. First, we focus on lithologically mixed samples that include some of the very few peridotites recovered from a ridge axis and one of the only sets of abyssal pyroxenites. Second, we describe in detail geochemical variations among and within peridotite samples from individual dredges. Sampling length scales of individual dredges can be estimated from dredge wire tension records and the dredges in this study represent length scales of <1 km. At this length scale, in an upwelling and partially melting system, mantle peridotites experience the same pressure and temperature conditions. Any chemical and isotopic variations observed among peridotites from a single dredge must be due to either initial (premelting) heterogeneities or recent melt-rock reaction.

[8] Finally, to look at the evolution of mantle heterogeneity, we compare all existing isotope data for abyssal peridotites to mantle isotope evolution models. As discussed above, studies of both peridotite and basalt compositions indicate that the mantle is heterogeneous in composition. However, MORB generation is often discussed with reference to a single, average upper mantle composition: the depleted MORB mantle (DMM). Mantle isotopic evolution is then modeled using DMM as a constraint. We assess the degree to which models of this type can predict the entire spectrum of mantle compositions, as observed among abyssal peridotites. The composition of DMM has most recently been estimated by *Salters and Stracke* [2004] and *Workman and Hart* [2005], using the average isotopic composition of MORB to constrain the composition of DMM. As the estimate of *Workman and Hart* [2005] includes determinations of the trace and major element compositions of individual mineral phases, we use their DMM estimate as a benchmark for average source composition, for comparison to abyssal peridotite compositions.

2. Geologic Setting

[9] Samples in this study are from two areas of the ultraslow spreading SWIR: the Oblique 9°–16°E Segment and the Atlantis II Fracture Zone (Figure 1). Peridotites are relatively abundant in both localities, due to the local geodynamic setting. Along the Oblique Segment, the obliquity of the angle of spreading to the direction of plate motion (Figure 1) results in slower upwelling and a thicker lithospheric lid, and thus reduced degrees of melting. The effective full spreading rate (the component of spreading perpendicular to the ridge trend) varies along the segment from 7.5 to 14 mm/yr, at the lowest end of the spectrum of global ridge spreading rates. Peridotites from the Atlantis II Fracture Zone (14 mm/yr full spreading rate) are also expected to have undergone low degrees of melting, due to an ultraslow spreading rate combined with the thermal influence of the old lithospheric plate at the ridge-transform intersection.

[10] Both the Oblique Segment and the Atlantis II Fracture Zone have been extensively sampled. Figure 1 shows the locations and lithologies of dredges from each area and Table 1 lists the locations of the five dredges used in this study. We focus in detail on two on-axis Oblique Segment dredges, one of which contains abundant pyroxenite (dredge Van7-96), while the other contains typical depleted peridotite (dredge Van7-85). In addition, we look at one Atlantis II Fracture Zone dredge in detail, RC27-9-6, as it contains a clinopyroxenite-veined peridotite. The regional-scale isotopic variations for peridotite mineral separates from the Oblique Segment and the Atlantis II Fracture Zone were determined by *Salters and Dick* [2002] and provide a framework for our dredge-scale data sets.

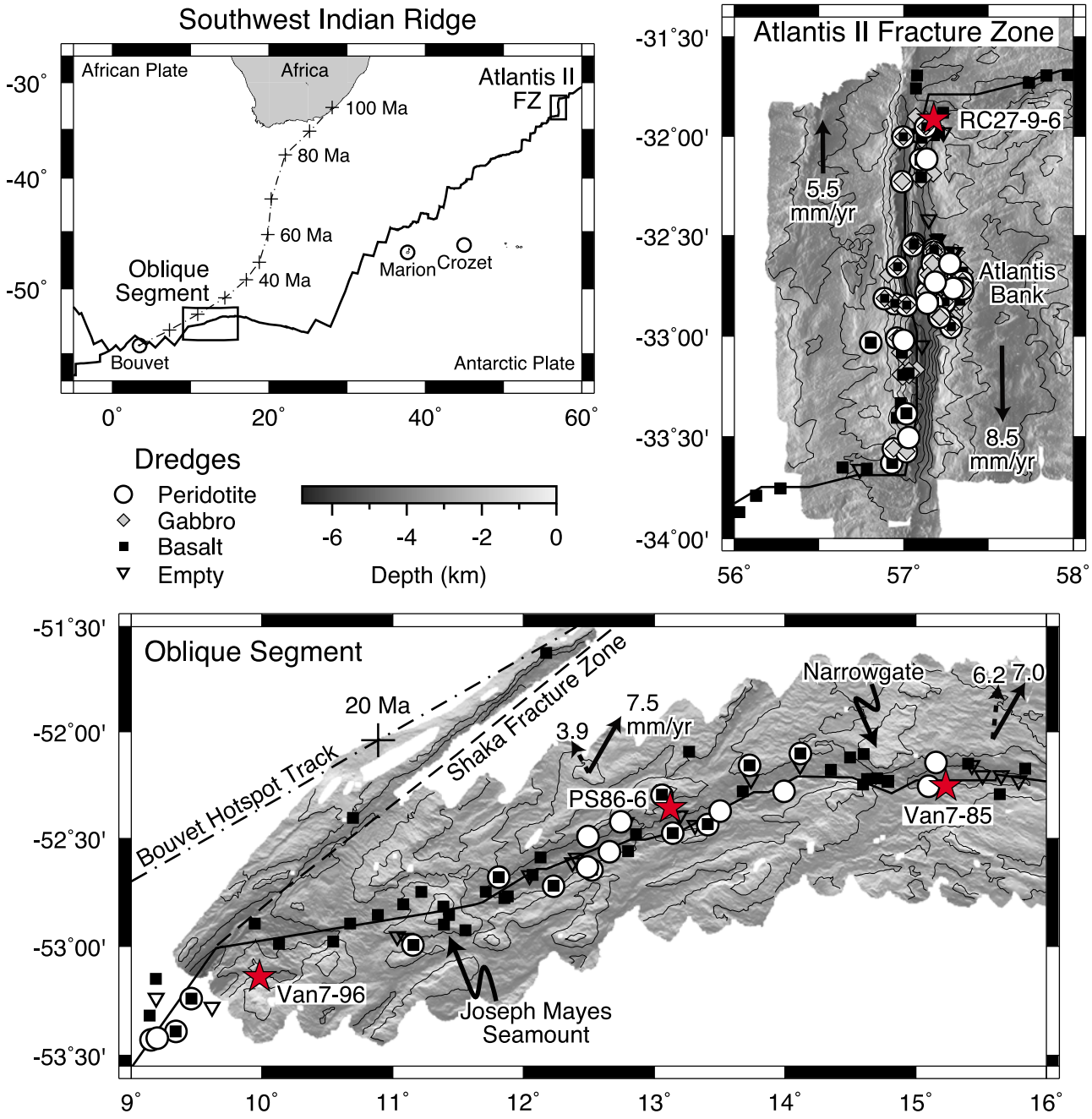

Figure 1. Maps of the Southwest Indian Ridge, Oblique Segment, and Atlantis II Fracture Zone. Bouvet, Marion, and Crozet are hot spots associated with the SWIR. The dashed-dotted line indicates the path of Bouvet Hotspot, calculated by *Hartnady and le Roex* [1985] using finite reconstruction poles from *Morgan* [1983]. Bouvet Hotspot passed along the trace of the Shaka Fracture Zone (dashed line) at the eastern end of the Oblique Segment from 15–25 Ma. No hot spot tracks are associated with the Atlantis II Fracture Zone. Atlantis Bank is an uplifted gabbroic massif located under the large cluster of dredges along the Atlantis II Fracture Zone. Solid arrows indicate the direction of plate motion. On the Oblique Segment, dashed arrows indicate the obliquity of the spreading direction to the plate direction.

[11] The Oblique Segment was sampled during the 1976 *ARA Islas Orcadas* IO11/76 cruise, the 1981 *SA Agulhas* AG22 cruise, the 1986 R/V *Polar Stern* PS86 cruise, the 2001 R/V *Knorr* Kn162 cruise, and the 2003 R/V *Melville* Van7 cruise. Basalts from these cruises have been analyzed by *le Roex et al.* [1983, 1992], *Mahoney et al.* [1992], *Janney et al.* [2005], *Standish* [2006], and *Standish et al.* [2008]. As shown in Figure 1, the western end of the Oblique Segment is coincident with the path of the Bouvet Hotspot, which passed along this region at 15–25 Ma [*Hartnady and le Roex*, 1985].

[12] The Atlantis II Fracture Zone was sampled during the 1976 R/V *Atlantis II* AII93-5 cruise, the 1986 R/V *Conrad*

Table 1. Dredge Locations

Dredge	Contents	Wt (kg)	On/Off Bottom			FSR[a]	Angle[a]	ESR[a]	Location
			Latitude (°S)	Longitude (°E)	Depth (m)	(mm/yr)		(mm/yr)	
				Oblique Supersegment, SWIR					
Van7-85	Peridotite, dunite, diabase	90	52.25/52.27	15.23/15.23	4190/3547	14.22	32.5°	11.99	S wall of axial trough, east of Narrowgate
Van7-86	Dunite, peridotite	146	52.14/52.13	15.16/15.15	3765/3128	14.21	32.6°	11.97	N wall of axial trough, east of Narrowgate
Van7-96	Cataclastites, perid, pyroxenite, diabase	81	53.14/53.15	9.98/9.97	3134/2527	14.06	28.5°	12.36	SW wall of axial trough at Shaka FZ intersection
PS86-6	Peridotite, basalt, gabbro-veined perid	187	52.44/52.33	13.13/13.15	4509/3073	14.14	51.4°	8.82	N wall of axial trough, midway along segment
				Atlantis II Fracture Zone, SWIR					
RC27-9-6	Peridotite, dunite	37	31.92/31.93	57.18/57.18	4010/3500	14.00[b]	0.0°	14.00	E wall of transform, at ridge intersection

[a]The effective spreading rate (ESR) is calculated from the full spreading rate (FSR) and angle of obliquity, following the method of *Abelson and Agnon* [1997].
[b]Due to asymmetrical spreading, the half spreading rate is 8.5 mm/yr to the south [*Hosford et al.*, 2003].

RC27-9 cruise, and the 1998 RRS *James Clark Ross* JR31 cruise. Atlantis Bank, an uplifted gabbro massif located along the transform fault, formed by detachment faulting between 9.5 and 13 Ma [*Dick et al.*, 1991], has been the focus of Ocean Drilling Program (ODP) Leg 118 in 1987, Leg 176 in 1997 and Leg 179 in 1998 and of dives using the manned submersible Shinkai 6500 in 1998 and 2001 and the remotely operated vehicle Kaiko in 2000. Atlantis II Fracture Zone basalts have been analyzed by *Mahoney et al.* [1989], *Dick et al.* [1991], *Kempton et al.* [1991], *Snow* [1993], and *Coogan et al.* [2004]. In addition, 1.5 km of gabbro from Hole 735B (drilled on Atlantis Bank during ODP Legs 118 and 176) have been analyzed for isotopic compositions by *Kempton et al.* [1991], *Hart et al.* [1999], and *Holm* [2002].

3. Methods

[13] Analysis of modal compositions, trace element concentrations, and Nd and Sr isotopes were carried out on sixteen samples: eleven peridotites, three pyroxenite veined peridotites, and two pyroxenites. Clinopyroxene (Cpx) mineral separates were analyzed for isotopes in all samples and orthopyroxene (Opx) for isotopes in six samples. In the veined samples, Cpx from the vein and matrix were measured separately. Cpx from three peridotites were successfully analyzed for Pb isotopes. The only basalt recovered in any of the same dredges as the peridotites (a glass fragment in a breccia from dredge Van7-96) was also analyzed. Trace element and isotope analyses were carried out at the Pheasant Memorial Laboratory at the Institute for Study of the Earth's Interior in Japan.

3.1. Sample Selection and Characteristics

[14] Peridotites were analyzed from five dredges, listed in Table 1, with a focus on two dredges: Van7-85, which contains typically depleted peridotites, and Van7-96, containing pyroxenite-veined peridotites. Also analyzed were one peridotite from dredge PS86-6, for interlab comparison to *Salters and Dick* [2002], and one peridotite from dredge Van7-86, a more altered peridotite dredge adjacent to dredge 85, for determination of the effects of alteration on Sr isotopic composition. From the Atlantis II Fracture Zone, we analyzed sample RC27-9-6-2, which contains a clinopyroxenite vein. Other samples from dredge RC27-9-6 were analyzed previously by *Salters and Dick* [2002].

[15] Dredge 85 is from a relatively amagmatic region of the Oblique Supersegment (Figure 1) and contains 65 kg peridotite, 11 kg dunite, and 2 kg diabase. The peridotites are "typical" in appearance (Figure 2a), consisting of Opx and Cpx porphyroclasts in an altered olivine matrix, no veins and 2%–6% modal Cpx. As shown in Figure 4, trace element concentrations are characteristic of depleted abyssal peridotites [e.g., *Johnson et al.*, 1990]. Two harzburgites (Van7-85-27 and Van7-85-30) and three lherzolites (Van7-85-42, Van7-85-47, and Van7-85-49), representative of the modal Cpx range of the dredge, were chosen for isotope analysis.

[16] Dredge 96 consists predominantly of lherzolites and harzburgites with pyroxenite veins (Figures 2b–2f). The dredge is from the inside corner high of the ridge with the Shaka Fracture Zone (Figure 1) and consists of 36 kg peridotite, 44 kg pyroxenite-veined peridotites, 3 kg pyroxenites, 39 kg polymict breccias and 8 kg diabase. Pyroxenite veins range in width from 1 to 10 cm and either crosscut larger peridotites samples (Figure 2c) or occur as individual samples with thin peridotite skins (Figure 2e). The veins themselves are crosscut by narrower veins (Figure 2e) predominantly composed of altered plagioclase and olivine. The absence of plagioclase in the coarser-grained regions of the pyroxenites and the presence of Opx, which does not appear with plagioclase on the low pressure liquidus of basalt [*Stolper*, 1980], indicate that plagioclase is related to a second, shallow level melt intrusion event. In addition, rims of Cpx grains have Eu anomalies whereas Cpx cores do not (J. M. Warren, unpublished ion probe data, 2009), further evidence for the later crystallization of plagioclase. Samples selected for analysis from this dredge include pyroxenites with little associated peridotite (Van7-96-09 and Van7-96-16), peridotites with pyroxenite veins (Van7-96-19 and Van 7-96-21), vein-free peridotites (Van7-96-25, Van7-96-28, Van7-96-35 and Van7-96-38) and basalt from a breccia (Van7-96-68).

[17] Sample RC27-9-6-2 from Atlantis II Fracture Zone was selected for detailed analysis due to the presence of an unusual clinopyroxenite vein (Figures 2g–2h) and also due to the preexisting data set for other peridotites from the same dredge. While the sample was investigated by *Snow et al.*

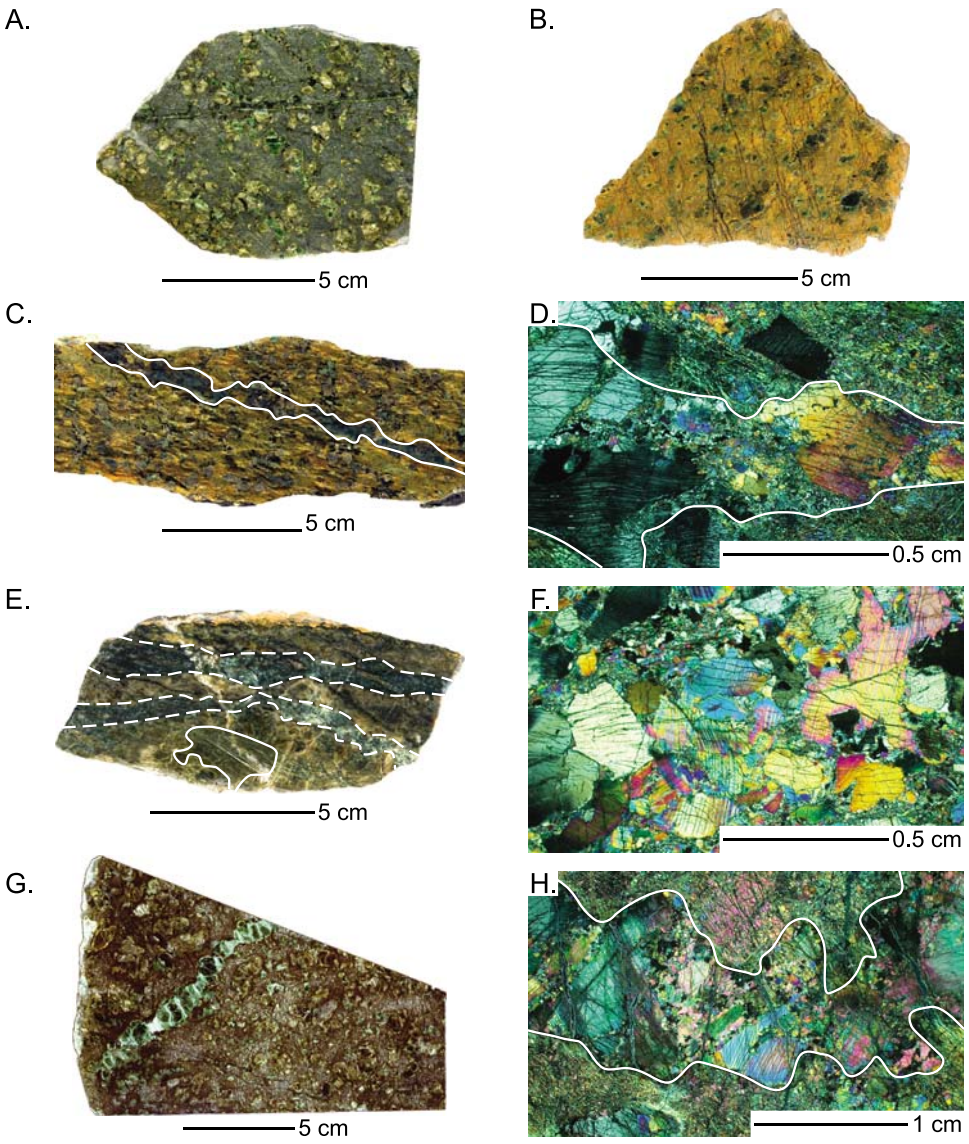

Figure 2. (a) Depleted lherzolite, Van7-85-49, with 5% Cpx. (b) Enriched peridotite, Van7-96-28, with 5% Cpx. Apart from the different alteration style, this peridotite has no visual characteristics that distinguish it from the dredge 85 peridotite. (c) Pyroxenite veined peridotite, Van7-96-21, with the vein outlined in white. (d) Cross-polarized photomicrograph of the same sample. (e) Pyroxenite, Van7-96-16, with a thin, altered, orange peridotite skin at the top. A particularly large Cpx grain is outlined in white. The pyroxenite is crosscut by two later stage veins of fine-grained Ol-Plag-Cpx, outlined with dashed lines. (f) Cross-polarized photomicrograph of a pyroxenite, Van7-96-09, consisting of coarse-grained Cpx and Opx with minor olivine. The fine-grained, cross-cutting assemblage of Ol-Plag-Cpx is from the later stage melt infiltration event. (g) RC27-9-6-2, the clinopyroxenite veined lherzolite. (h) Cross-polarized photomicrograph of the same sample, with the vein outlined in white. Photos of hand samples are courtesy of Tom Kleindinst.

[1994] and *Lee* [1997], we present here isotopic analyses for vein and matrix minerals measured separately. The sample is unusually Cpx rich (12%) and clinopyroxenite veins are rarely sampled among abyssal peridotites (one other occurrence has been reported by *Constantin et al.* [1995] in an East Pacific Rise peridotite). In contrast, websterites (mixtures of Opx and Cpx, with or without olivine) have been reported from most ridges [*Dick et al.*, 1984; *Kempton and Stephens*, 1997; *Dantas et al.*, 2007]. These typically have depleted trace element compositions, in contrast to both the RC27-9-6-2 clinopyroxenite and the dredge 96 pyroxenites.

3.2. Modal Analyses

[18] All samples were point counted for mineral modes (Table 2) under an optical microscope using large, 51 × 75 mm thin sections and a grid spacing of 1 mm. For the peridotites, a minimum of 1700 points were counted. The pyroxenites, due to their limited size, have fewer points and hence larger associated errors.

3.3. Chemical Analyses

[19] Mineral separates of Opx and Cpx were obtained by lightly crushing thin slices of the peridotite samples,

Table 2. Peridotite Modal Compositions

Sample	Lithology	Oliv	Opx	Cpx	Spin	Plag	Sum	Points
Van7-85-27	Harzburgite	68.6	27.5	3.1	0.9	0.0	100.0	2506
Van7-85-30	Harzburgite	67.4	29.2	2.1	1.2	0.2	100.0	2483
Van7-85-42	Lherzolite	67.1	25.6	6.2	1.0	0.0	100.0	2825
Van7-85-47	Lherzolite	68.7	24.7	5.1	1.5	0.0	100.0	2594
Van7-85-49	Lherzolite	71.6	22.2	5.3	0.9	0.1	100.0	2607
Van7-86-27	Lherzolite	55.8	34.0	9.6	0.6	0.0	100.0	2566
Van7-96-09V	Pyx Vein	9.3	25.8	48.5	1.9	14.6	100.0	756
Van7-96-16V	Pyx Vein	11.6	34.0	24.4	1.6	28.4	100.0	697
Van7-96-19M	Lherz w/Pyx Vein	64.8	17.9	13.3	0.8	3.1	100.0	1883
Van7-96-19V	Pyx Vein in Lherz	7.2	26.4	57.2	2.8	6.3	100.0	318
Van7-96-21M	Harz w/Pyx Vein	76.2	18.1	4.6	0.6	0.4	100.0	1894
Van7-96-21V	Pyx Vein in Harz	19.7	39.3	37.5	2.2	1.3	100.0	461
Van7-96-25	Lherzolite	66.2	25.6	6.8	1.4	0.0	100.0	2215
Van7-96-28	Lherzolite	76.7	17.2	5.4	0.7	0.0	100.0	2738
Van7-96-35	Lherzolite	70.4	16.7	10.5	2.3	0.1	100.0	1765
Van7-96-38	Lherzolite	64.2	24.1	9.9	1.6	0.2	100.0	2278
PS86-6-38	Lherzolite	56.7	29.0	12.6	1.7	0.0	100.0	3124
RC27-9-6-2M	Lherz w/Cpx Vein	67.5	19.5	11.9	0.9	0.2	100.0	2194
RC27-9-6-2V	Cpx Vein in Lherz	7.6	9.2	82.6	0.7	0.0	100.0	436

handpicking under a binocular microscope and then repicking to ensure purity of the concentrate. All grains were visually free of inclusions and uniform in color, except for a less pure separate of Van7-96-16, included for comparison to an optically pure separate of the same sample. Unleached concentrate weights were in the range 25–900 mg. Concentrates were leached ultrasonically in 6M HCl overnight and rinsed in water. Further light crushing in a SiN mortar and pestle exposed cleavage alteration surfaces. Concentrates were then leached ultrasonically for 5 min in 0.1M HF, rinsed with water, leached ultrasonically twice more with 6M HCL for 8 h each, rinsed with water and finally leached ultrasonically with 0.5M HNO_3 for 5 min. Following a final rinsing with water, samples were dried on a hot plate in a draft chamber with clean air. After leaching, 15–700 mg material remained per mineral separate. Prior to dissolution for high field strength elements (HFSE) and isotope analyses, concentrates were crushed to powder in a SiN mortar and pestle.

3.3.1. ICP-MS Analyses of Trace Elements

[20] Samples were analyzed by ICP-MS for 28 trace element concentrations (Table 3), of which the HFSE were prepared and measured independently of the other trace elements. In addition, blanks and the external rock standard JB-2 (tholeiitic basalt, Geological Survey of Japan) were prepared with the samples. For analyses of Li, Be, Rb, Sr, Y, Cs, Ba, rare earth elements (REEs), Pb, Th, and U, from 2 to 10 mg of weighed sample was spiked with ^{149}Sm and dissolved in two stages following the method of *Makishima and Nakamura* [1997]. In the first stage, samples were decomposed in 7M $HClO_4$ and 30M HF using a combination of ultrasonic bath and hotplate heating for several days, followed by stepwise drying. In the second stage, the samples were heated overnight after addition of 6M HCl, followed by stepwise drying. Finally, the samples were dissolved in 16M HNO_3 to a dilution factor of 1000 prior to analysis.

[21] Analyses of HFSE (Zr, Nb, Hf, and Ta) used weighed sample amounts of 3–12 mg and a mixed ^{91}Zr-^{179}Hf spike. Full recovery of HFSE following dissolution requires dissolution in HF. However, in Ca-rich materials, HF leads to the precipitation of fluoride compounds containing HFSE. To suppress the coprecipitation of HFSE, a solution of Al metal dissolved in HF and HCl was added prior to dissolution. The amount of Al solution added per sample was calculated to bring the Al/(Al + Ca) ratio of the pyroxene to 0.9, which has been shown to effectively limit HFSE coprecipitation in fluoride compounds [*Tanaka et al.*, 2003]. Following the Teflon bomb method of *Tanaka et al.* [2003], samples were dissolved in 30M HF at 245°C for 48 h. After dissolution, mannitol was added to sample solutions, which were then placed overnight in ultrasonic baths before being dried at 80°C in a clean air system. Prior to analysis, samples were dissolved in 30M HF to a dilution factor of 800, centrifuged and transferred to new containers to remove any remaining fluorides from the solutions.

[22] Trace elements were analyzed using an Agilent 7500cs Q pole–type ICP-MS, following the procedures of *Makishima and Nakamura* [1997, 2006] and *Makishima et al.* [1999]. Samples were introduced via fluid injection using a microconcentric nebulizer. Every two samples were bracketed by analysis of the JB-2 unspiked standard. Data reduction followed the isotope dilution internal standardization method of *Makishima and Nakamura* [2006], using ^{149}Sm as the internal standard. For HFSE, the internal standard ^{91}Zr was used for Zr and Nb and the internal standard ^{179}Hf was used for Hf and Ta. The 2σ reproducibility of the rock standard JB-2 is 1.4–6.6%, blanks were <20 pg and detection limits 10–100 ppb (Table 3). The elements Rb, Cs, and Ta were below detection limits for the samples in this study and are not reported here.

3.3.2. TIMS Analyses for Sm-Nd and Rb-Sr

[23] Analyses of Sm-Nd and Rb-Sr isotope ratios and concentrations by TIMS followed the techniques of *Nakamura et al.* [2003]. Sample amounts ranged between 9 and 240 mg (Table 4), with the amount used determined by the Nd and Sr concentrations of the sample. Sample powders were spiked with ^{84}Sr, ^{87}Rb, ^{150}Nd and ^{149}Sm prior to addition of 7M $HClO_4$, 30M HF, 16M HNO_3, and 6M HCl for dissolution. A combination of ultrasonic bath and heating on a hotplate was used to achieve dissolution. The dissolved minerals were stepwise dried using closed system evaporators to limit contamination; this evaporation system was used in all subsequent drying steps. A combination of $HClO_4$ addition and additional stepwise drying were used to completely decompose insoluble fluorides. The first separation

Table 3. Trace Element Concentrations in ppm for Cpx, Opx, and Basalt

Sample[a]	Phase	TE[b]	HFSE[b]	Ba[c]	Pb	Sr	La	Ce	Pr	Nd	Sm	Eu	Gd	Th	Tb	Dy	Y	Ho	Er	U	Tm	Yb	Lu	Li	Zr	Hf	Nb	Be
Error (2σ)[d]				3%	6%	2%	1%	2%	4%	3%	3%	2%	4%	5%	3%	4%	5%	3%	2%	6%	3%	3%	3%	3%	3%	2%	4%	
Van7-85-27	Cpx			0.043		0.98		0.029	0.029	0.297	0.39	0.189	0.83		0.182	1.39	7.8	0.32	0.86		0.130	0.88	0.126	0.78	n.m.	n.m.	n.m.	
Van7-85-30	Cpx	0.71			0.33	0.30		0.005	0.011	0.236	0.40	0.198	1.00		0.244	1.91	12.4	0.44	1.22		0.190	1.23	0.168	0.39	n.m.	n.m.	n.m.	0.862
Van7-85-42	Cpx	4.51	5.3			0.129		0.006	0.007	0.252	0.37	0.185	0.99		0.245	1.87	12.3	0.44	1.25		0.192	1.26	0.178	2.38	0.52	0.096	0.004	
Van7-85-42	Opx	4.08	5.5				0.002			0.007	0.016	0.011	0.066		0.023	0.220	1.87	0.065	0.218		0.044	0.34	0.060	0.57		0.010	0.003	
Van7-85-47	Cpx	3.84	7.4			0.139		0.004	0.007	0.259	0.35	0.188	1.01		0.230	1.84	12.2	0.43	1.21		0.185	1.19	0.175	2.64	0.215	0.086	0.004	
Van7-85-47	Opx	8.87	8.4							0.007	0.011	0.010	0.063		0.021	0.200	1.82	0.059	0.220		0.044	0.34	0.059	0.79	0.009	0.018	0.003	
Van7-85-49	Cpx	2.91	3.4		0.002	0.63		0.019	0.019	0.289	0.41	0.213	1.19		0.283	2.3	15.2	0.54	1.50		0.236	1.49	0.219	2.94	0.264	0.079	0.003	
Van7-85-49	Opx	2.97	4.5		0.101	0.025					0.016	0.010	0.066		0.021	0.209	1.86	0.060	0.211	0.0002	0.044	0.34	0.059	0.79		0.011		
Van7-86-27	Cpx			0.218		1.04	0.002	0.013	0.007	0.107	0.28	0.130	0.71		0.165	1.31	7.2	0.31	0.86		0.133	0.87	0.119	2.37	n.m.	n.m.	n.m.	
Van7-96-09V	Cpx					4.0	0.181	1.32	0.38	2.62	1.26	0.54	2.14		0.43	3.1	17.6	0.72	2.02	0.0005	0.30	2.01	0.277	1.96	n.m.	n.m.	n.m.	
Van7-96-09V	Opx	4.22		0.018	0.110	0.061	0.003	0.027	0.009	0.088	0.075	0.034	0.201		0.055	0.58	5.0	0.158	0.57	0.0002	0.112	0.87	0.153	0.73	n.m.	n.m.	n.m.	
Van7-96-16V	Cpx			0.101		2.25	0.048	0.64	0.27	2.21	1.31	0.52	2.12		0.44	3.1	17.6	0.71	2.00		0.30	2.06	0.283	0.61	n.m.	n.m.	n.m.	
Van7-96-16VII[e]	Cpx			0.288		1.49	0.023	0.207	0.058	0.37	0.135	0.171	0.179		0.033	0.24	1.38	0.059	0.183		0.032	0.238	0.042	0.082	n.m.	n.m.	n.m.	
Van7-96-19M	Cpx	2.84				5.8	0.258	2.23	0.62	4.1	1.92	0.69	2.9		0.57	3.9	24	0.84	2.27		0.34	2.06	0.288	1.10	n.m.	n.m.	n.m.	
Van7-96-19M	Opx	5.24	7.2	0.190		0.82	0.015	0.089	0.020	0.178	0.105	0.044	0.234		0.055	0.45	3.3	0.119	0.376		0.070	0.50	0.085	1.03	6.3	0.207	0.008	
Van7-96-19V	Cpx	1.94	3.1	1.12		7.9	0.417	2.69	0.64	4.3	1.81	0.67	2.8	0.0013	0.52	3.8	21.6	0.79	2.04	0.0005	0.31	1.87	0.262	2.11	35	1.14	0.014	
Van7-96-21M	Cpx	5.96			0.005	23.7	0.85	4.20	0.88	5.3	1.87	0.72	2.37		0.45	2.9	18.1	0.64	1.70		0.249	1.61	0.225	1.70	n.m.	n.m.	n.m.	
Van7-96-21M	Opx	3.42	6.0		0.002	0.72	0.019	0.102	0.024	0.169	0.087	0.038	0.162	0.0003	0.038	0.31	2.4	0.080	0.271	0.0001	0.050	0.39	0.071	0.94	4.3	0.156	0.001	
Van7-96-21V	Cpx	4.21			0.005	20.0	0.98	4.5	0.90	5.5	1.87	0.70	2.37	0.0057	0.44	2.8	17.8	0.63	1.70		0.247	1.63	0.218	1.52	n.m.	n.m.	n.m.	
Van7-96-25	Cpx	2.08				9.4	0.170	1.38	0.35	2.52	1.13	0.51	1.86		0.37	2.6	15.4	0.57	1.50		0.231	1.46	0.209	2.64	n.m.	n.m.	n.m.	
Van7-96-28	Cpx	2.93			0.016	75	1.03	3.29	0.60	3.4	1.19	0.47	1.57	0.018	0.285	1.83	11.4	0.39	1.04	0.0046	0.155	1.04	0.145	1.47	n.m.	n.m.	n.m.	
Van7-96-28	Opx	9.26	4.4		0.003	1.65	0.020	0.057	0.009	0.085	0.054	0.022	0.096	0.0008	0.020	0.183	1.41	0.045	0.152	0.0005	0.030	0.225	0.039	0.81	1.65	0.061	0.013	
Van7-96-35	Cpx	3.52				32.4	0.433	2.18	0.51	3.3	1.34	0.54	1.82	0.018	0.34	2.3	12.4	0.46	1.18	0.0064	0.165	1.00	0.141	1.88	n.m.	n.m.	n.m.	0.02
Van7-96-38	Cpx	4.48	11.7			10.3	0.064	0.88	0.33	2.49	1.34	0.59	2.18		0.45	3.2	20.7	0.72	1.92		0.29	1.87	0.262	4.4	14.3	0.64	0.003	0.02
Van7-96-38	Opx	6.29	6.1		0.004	0.2		0.018	0.007	0.067	0.054	0.026	0.128		0.033	0.31	2.6	0.082	0.279		0.054	0.408	0.071	1.64	2.01	0.115		
Van7-96-68	Basalt			105	1.07	249	11.8	28.4	3.77	16.6	4.32	1.60	4.9	1.42	0.83	5.2	32	1.10	2.92	0.42	0.44	3.01	0.43	6.1	n.m.	n.m.	n.m.	0.86
PS86-6-38	Cpx	2.52	3.1			5.9	0.025	0.51	0.255	2.30	1.30	0.57	2.17		0.44	3.2	19.8	0.70	1.88		0.282	1.75	0.257	2.75	7.9	0.456	0.002	
RC27-9-6-2M	Cpx	3.06	5.6			69	0.67	2.50	0.41	1.94	0.52	0.208	0.72	0.0051	0.138	0.94	5.5	0.20	0.55	0.0026	0.085	0.54	0.078	14.3	3.6	0.136	0.028	0.04
RC27-9-6-2M	Opx	6.06	5.0		0.012	2.51	0.029	0.096	0.014	0.090	0.026	0.016	0.060		0.014	0.135	1.08	0.036	0.112		0.023	0.175	0.029	6.2	0.87	0.026	0.014	
RC27-9-6-2V	Cpx	3.02	5.3			16.8	0.208	0.91	0.212	1.26	0.65	0.277	1.07	0.0023	0.216	1.55	9.0	0.33	0.87	0.0010	0.130	0.80	0.113	12.8	4.5	0.221	0.037	

[a]M indicates the peridotite matrix of a veined sample and V indicates a pyroxenite vein.
[b]Weight of material used for analysis, in mg.
[c]Empty values are below detection limit; *n.m.* indicates not measured.
[d]Calculated from repeat measurements of the standard basalt reference material JB2 (Geological Survey of Japan).
[e]Less pure Cpx separate: nonoptically pure grains contain small black inclusions and white alteration material.

Table 4. Nd and Sr Isotopic Compositions of Peridotite Cpx and Opx

Sample[a]	Phase	Wt (mg)	$^{87}Sr/^{86}Sr$[b]	Rb[c] (ppb)	Sr[c] (ppm)	$^{143}Nd/^{144}Nd$[b]	ε_{Nd}	Sm[c] (ppm)	Nd[c] (ppm)
Van7-85-27	Cpx	41.47	0.702855(25)	6.52	1.010	0.513297(25)	12.85	0.465	0.4199
Van7-85-30	Cpx	15.41	0.704301(27)	1.20	0.259	0.513133(100)	9.65	0.407	0.2490
Van7-85-42	Cpx	190.99		1.13		0.513335(27)	13.59	0.352	0.2065
Van7-85-47	Cpx	149.60	0.702286(22)	1.51	0.156	0.513322(27)	13.34	0.336	0.2128
Van7-85-47R[d]	Cpx	139.74	0.702176(25)	0.29	0.154	0.513330(24)	13.50	0.3849	0.2482
Van7-85-49	Cpx	43.30	0.702844(24)	0.50	0.497	0.513249(25)	11.92	0.339	0.2247
Van7-86-27	Cpx	105.32	0.704431(24)	24.03	1.254	0.513060(31)	8.23	0.2983	0.1687
Van7-96-09V	Cpx	19.65	0.703421(24)	0.65	5.888	0.513050(24)	8.04	1.401	2.8771
Van7-96-09V	Opx	204.86	0.703631(25)	0.28	0.079	0.513061(29)	8.25	0.0696	0.0899
Van7-96-16V	Cpx	29.44	0.703432(24)	15.58	2.214	0.512844(24)	4.01	1.581	2.8256
Van7-96-16V	CpxII[e]	37.25	0.703282(24)	27.2	1.622	0.512798(24)	3.12	0.259	0.5812
Van7-96-19M	Cpx	9.89	0.703052(14)	7.22	7.536	0.513018(26)	7.41	2.635	5.801
Van7-96-19M	Opx	79.30	0.703151(15)	13.72	0.823	0.512982(27)	6.71	0.1139	0.1854
Van7-96-19V	Cpx	9.49	0.703097(14)	31.1	10.584	0.512993(27)	6.92	2.723	6.349
Van7-96-21M	Cpx	241.45	0.703709(24)	0.33	23.887	0.513069(22)	8.41	1.978	5.4349
Van7-96-21M	Opx	100.80	0.703701(24)	0.09	0.502	0.513096(25)	8.94	0.086	0.1653
Van7-96-21V	Cpx	66.42	0.703715(25)	2.30	20.138	0.513107(23)	9.15	2.007	5.7292
Van7-96-25	Cpx	12.89	0.702480(13)	0.52	12.384	0.513184(27)	10.65	1.555	3.277
Van7-96-28	Cpx	191.22	0.703061(24)	0.25	82.843	0.512938(23)	5.85	1.224	3.4344
Van7-96-28	Opx	137.78	0.703046(24)	0.08	1.601	0.513053(34)	8.09	0.0459	0.0845
Van7-96-35	Cpx	10.15	0.703732(15)	1.10	43.607	0.512936(27)	5.81	1.831	4.427
Van7-96-38	Cpx	91.37	0.702096(24)	5.67	10.893	0.513205(22)	11.06	1.411	2.6592
Van7-96-38	Opx	224.64	0.702102(24)	2.32	0.263	0.513098(29)	8.97	0.0578	0.0715
Van7-96-68	Basalt	21.85	0.702735(24)	9890	261.0	0.513015(22)	7.35	4.709	18.127
PS86-6-38	Cpx	11.91	0.702593(13)		5.693	0.513032(27)	7.68	1.319	2.2341
PS86-6-38S[f]	Cpx		0.702598(13)			0.513044(10)			
RC27-9-6-2M	Cpx	19.53	0.704993(13)	4.29	74.815	0.512915(27)	5.40	0.634	2.317
RC27-9-6-2M	Opx	170.89	0.704987(14)	1.94	2.531	0.512937(43)	5.83	0.0375	0.1053
RC27-9-6-2V	Cpx	21.61	0.704447(14)	1.76	16.951	0.513099(27)	8.99	0.685	1.3526

[a]M indicates the peridotite matrix of a veined sample and V indicates a pyroxenite vein.
[b]Data are fractionation corrected to $^{146}Nd/^{144}Nd = 0.7219$ and $^{86}Sr/^{88}Sr = 0.1194$ and reported relative to La Jolla $^{143}Nd/^{144}Nd = 0.511858$ and NBS987 $^{87}Sr/^{86}Sr = 0.710271$. Number in parenthesis indicates the 2σ error in the last digits.
[c]2σ error is ±1 in the last digit.
[d]Repeat analysis.
[e]Less pure Cpx separate: nonoptically pure grains that contain small black inclusions and white alteration material.
[f]Analysis by *Salters and Dick* [2002], renormalized to above standard values and included for comparison.

step for Rb, Sr and REE used 1 mL columns with Bio-Rad AG-50WX10 cation exchange resin and HCl [*Yoshikawa and Nakamura*, 1993; *Nakamura et al.*, 2003]. Rb and Sr were separated using a second cation exchange column with 0.5 mL of Muromac AG-50WX8 cation exchange resin and HCl. Nd and Sm were separated in a second column with 0.3 mL of Muromac AG-50WX8 resin and using α-hydroxyisobutyric acid for elution.

[24] Sr and Nd isotopic compositions and Rb, Sr, Nd and Sm concentrations were determined on a Finnigan-MAT262 solid source thermal ionization mass spectrometer equipped with 5 Faraday cups. In addition, some Sr analyses were run on a Finnigan-Triton mass spectrometer with 9 Faraday cups. Analytical procedures followed *Nakamura et al.* [2003]. Sr was dissolved in dilute HNO_3 and loaded with a Ta_2O_5 activator on trapezoid shaped single W ionization filaments. Data are fractionation corrected to $^{86}Sr/^{88}Sr = 0.1194$ and reported relative to $^{87}Sr/^{86}Sr = 0.710250$ for the NBS 987 standard [*Faure and Mensing*, 2005]. Rb concentrations were measured using a Ta-Re double filament with Rb dissolved in dilute HNO_3 prior to loading on the Ta filament. The 2σ analytical reproducibility for 1 pg of Rb by this method is better than 1%, based on 10 replicate analyses [*Nakamura et al.*, 2003].

[25] Nd isotopic analysis used Re double filaments, with Nd dissolved in dilute HNO_3 prior to loading onto the Re ionization filament. Data were collected relative to the internal PML Nd standard, which has a value of $^{143}Nd/^{144}Nd = 0.511769 \pm 0.000011$ ($2\sigma_m$, n = 5) with respect to 0.511892 ± 0.000007 ($2\sigma_m$, n = 8) for the La Jolla Nd standard. Data are fractionation corrected to $^{146}Nd/^{144}Nd = 0.7219$ and reported relative to $^{143}Nd/^{144}Nd = 0.511858$ for the La Jolla standard [*Lugmair and Carlson*, 1978]. Determination of Sm concentrations followed the same Ta-Re double filament method used for Rb, with a 2σ analytical reproducibility of 1% for 1 pg Sm, based on 10 replicate analyses [*Nakamura et al.*, 2003].

[26] The average blank for Rb is 4 pg, for Sr is 20 pg, for Sm is 0.4 pg and for Nd is 3 pg. The Nd average excludes two blanks of 37 pg and 200 pg, which are associated with a group of 5 samples. Propagating these values into the composition of the relevant samples does not greatly alter their calculated isotopic composition or trace element concentrations. Overall, the blank effect on Nd and Sr isotopic compositions is <0.05% for the majority of samples. For the few samples with a high blank or for which a small sample volume was used, the blank effect is higher, but never more than 1.4%.

3.3.3. TIMS Analyses for Pb

[27] For Pb analyses, 50–600 mg of weighed mineral separates were dissolved in equal amounts of 8M HBr and 30M HF, with HBr used to suppress fluoride coprecipitation of Pb. Samples were heated and placed in ultrasonic baths for 3–7 days, and then centrifuged before transferring to new containers. The material remaining in the old containers was further treated with HBr, with an additional day of heating or placement in the ultrasonic bath to promote fluoride disso-

lution and Pb removal from fluorides. In none of the samples were fluorides completely dissolved. Samples were dried in closed system evaporators and diluted with HBr prior to column loading. Following the method of *Kuritani and Nakamura* [2002], a column with 0.1 mL of Bio-Rad AG-1X8 anion exchange resin was used to remove most elements apart from Pb, which was eluted in H_2O. A second column, with 0.01 mL Bio-Rad AG-1X8 resin, was used to remove trace contaminants from the Pb fraction, which was again eluted using H_2O.

[28] Following column separation, Pb concentrations were estimated from Pb count rates on the Agilent 7500cs ICP-MS. Of the 22 Cpx and Opx samples for which Pb was separated, only 3 Cpx samples yielded >1 ng Pb, which is sufficient for measurement of isotope ratios. The low Pb yields are probably due to the large amount of fluoride coprecipitation during dissolution, which was not adequately suppressed by HBr addition. Three basalt samples, one from dredge Van7-96 and two repeat analyses (Van7-92-03 and Kn162-61-71) from *Standish* [2006], were also prepared and these all yielded >5 ng Pb.

[29] Analytical procedures for the three Cpx samples followed the two double spikes method of *Kuritani and Nakamura* [2003]. A double spike enriched in ^{207}Pb and ^{204}Pb was added to a quarter of the sample and a double spike enriched in ^{205}Pb and ^{204}Pb was added to the remainder of the sample. For the basalts, analytical procedures followed the normal double spike method [e.g., *Hamelin et al.*, 1985; *Galer*, 1999], by adding a spike enriched in ^{207}Pb and ^{204}Pb to a quarter of the sample. The dried samples were dissolved in silicic acid and loaded on single Re filaments. All samples were analyzed on a Finnigan-MAT261 mass spectrometer equipped with 6 Faraday cups. Pb blanks were 15–30 pg and recovered sample Pb was 1–5 ng. Replicate analyses of the NBS 981 standard gave values of ^{206}Pb/^{204}Pb = 16.942 ± 0.002 ($2\sigma_m$), ^{207}Pb/^{204}Pb = 15.500 ± 0.002 ($2\sigma_m$) and ^{208}Pb/^{204}Pb = 36.727 ± 0.004 ($2\sigma_m$). Data are reported relative to the values of NBS 981 from *Todt et al.* [1996], consistent with the *Standish* [2006] Oblique Segment basalt data set.

4. Results

4.1. Data Quality

[30] To assess the effect of mineral separate purity, we analyzed two Cpx mineral separates from pyroxenite sample Van7-96-16. While one separate consisted of optically pure grains, the other consisted of Cpx which were not optically pure and contained inclusions of both black and white material. The REE compositions of both mineral separates are plotted in Figure 4b, with the impure separate shown as a dashed line. The pure Cpx separate is indistinguishable from the other pyroxenites. The impure separate has low REE concentrations with a positive Eu anomaly, indicative of plagioclase contamination of the Cpx. The Nd isotope ratios for these two separates are within error, while the pure separate has a higher Sr isotope ratio than the impure separate. Hence, the purity of the separate appears to affect trace element concentrations but not the Nd isotopic ratio.

[31] To test the precision of our analyses and for interlab comparison, we repeated the analysis of PS86-6-38 from *Salters and Dick* [2002]. As indicated in Table 4, our values for ^{143}Nd/^{144}Nd and ^{87}Sr/^{86}Sr agree within error with the Salters and Dick values. For Pb isotopes, we ran replicate analyses of two basalt samples from *Standish* [2006]. ^{206}Pb/^{204}Pb agree within error, but our samples have ^{207}Pb/^{204}Pb and ^{208}Pb/^{204}Pb offset to lower values (Figure 6), despite normalization of all data to the same standard values for NBS 981. To check internal reproducibility, we ran a duplicate analysis of Van7-85-47, starting from a split of the same powdered mineral separate. Table 4 shows that the duplicate analyses agree within error for ^{143}Nd/^{144}Nd, but not for ^{87}Sr/^{86}Sr (0.702286 vs 0.702176). The discrepancy between Sr isotope ratios may be the result of heterogeneous Sr distribution due to alteration phases not completely removed by leaching. We interpret the lower ^{87}Sr/^{86}Sr as the more representative value, as seawater alteration increases the Sr isotope ratio.

[32] Abyssal peridotites are generally severely altered by hydrothermal processes at the ridge and our samples are no exception. The majority of olivine is either serpentinized or altered to brownish orange clay minerals. Opx and Cpx are typically much fresher than olivine, but alteration occurs occasionally along rims and cleavage planes or as low-temperature amphibole alteration pseudomorphs. The alteration process results in isotopic exchange between minerals and fluid, and the precipitation of fluid-derived carbonates. Nd isotopic exchange is negligible due to low Nd concentrations in seawater, but Sr isotopic exchange and carbonate precipitation shift the ^{87}Sr/^{86}Sr of peridotite toward 0.709, the isotopic composition of seawater. In order to eliminate the seawater Sr signature, we followed a multiday, multistage leaching procedure using HCl, HF, and HNO_3, with an intermediate step of additional crushing, to remove alteration phases from the rims and cleavage planes of pyroxene grains. This procedure was effective in significantly reducing the seawater alteration signature based on the following three observations:

[33] 1. With a few exceptions, data plot on the same Nd-Sr isotope trend defined by basalts from the Oblique Segment [*Standish*, 2006], as illustrated in Figure 5.

[34] 2. Coexisting Cpx and Opx have similar ^{87}Sr/^{86}Sr ratios. As Opx is more susceptible to hydrothermal alteration due to its lower Sr concentrations, this result strongly supports our contention that alteration affects were minimized by our analytical technique.

[35] 3. Our results include a ^{87}Sr/^{86}Sr ratio of 0.702096 in Cpx from Van7-96-38, the most depleted value measured to date in abyssal peridotites and among the lowest measured in any basalt, thus attesting to the effectiveness of our leaching procedure.

[36] Despite extensive leaching, the two most visibly altered samples have ^{87}Sr/^{86}Sr > 0.704 (Van7-85-30 and Van7-86-27) and do not plot on the basalt Nd-Sr isotope trend (Figure 5). We conclude that pristine ^{87}Sr/^{86}Sr values were not recovered for these samples. The only sample in which a high ratio does not appear to be due to visible alteration is RC27-9-6-2, which is relatively unaltered for an abyssal peridotite (Figures 2g–2h). This sample is unusual in various ways, including the greater isotopic and trace element enrichment in the peridotite matrix than in the clinopyroxenite vein. However, until ^{87}Sr/^{86}Sr can be measured *in situ*, the origin of ^{87}Sr/^{86}Sr enrichment in this sample cannot be conclusively identified.

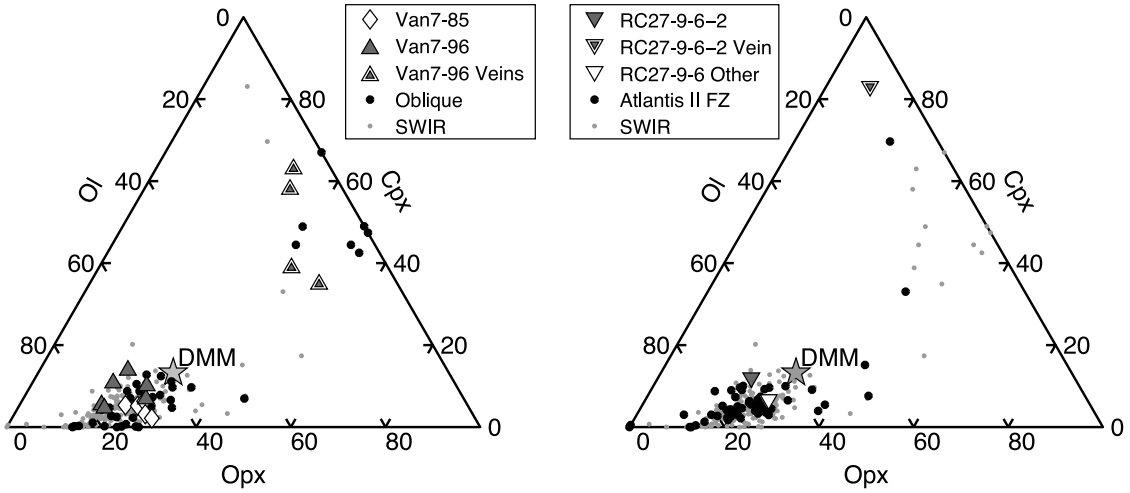

Figure 3. Modal composition of abyssal peridotites in this study compared to regionally associated abyssal peridotites. Data for other SWIR peridotites are from *Dick et al.* [1984], *Dick* [1989], *Johnson et al.* [1990], *Johnson and Dick* [1992], *Snow* [1993], *Kumagai et al.* [2003], *Morishita et al.* [2007], and *Dantas et al.* [2007]. The modal composition of DMM is from *Workman and Hart* [2005].

4.2. Modes and Petrography

[37] The unveined peridotites in this study (Figures 2a and 2b) are typical abyssal peridotites [*Dick*, 1989], ranging in modal Cpx content from 2% to 13%, as shown in the ternary diagrams in Figure 3. Mineral major element compositions, discussed in Appendix A, are also typical of abyssal peridotites. The variations of spinel Cr # (Cr/(Cr + Al) = 10–52), Mg # (Mg/(Mg + Fe) = 52–78) and TiO_2 (up to 0.5 wt%) suggest variable degrees of melting and, among veined peridotites, melt refertilization (Figure A1). The most unusual feature among Cpx major element compositions are the low Mg # (88.6–91.6) and Cr # (3–15) of Cpx in the dredge 96 pyroxenites (Figure A2). In contrast, Cpx in the clinopyroxenite vein in RC27-9-6-2 has relatively high Cr # (16–19, Figure A2).

[38] Dredge 96 pyroxenites consist of 25–39% Opx and 24–57% Cpx, with minor amounts of olivine, hence they are properly classified as websterites and Ol-websterites. The boundaries of narrower veins are difficult to distinguish in thin section, as veins are sometimes the width of a single pyroxene porphyroclast (Figure 2d). Veins of finer grained Ol-Plag-Cpx crosscut the coarser grained pyroxenites (Figure 2e) and plagioclase forms rims around spinels. As discussed earlier, we interpret the Ol-Plag-Cpx assemblage to be a late stage gabbroic melt which crystallized at shallow depths, whereas the original pyroxenites formed at depths greater than the plagioclase stability field.

[39] The clinopyroxenite vein in RC27-9-6-2 is composed of 82% large, bright green, Cr-rich Cpx (Figure 2e). Plagioclase is present in trace amounts (0.01–0.2%) in the vein and peridotite matrix. The Na content of plagioclase is higher in the peridotite matrix (An_{56}; Data Set S1 of the auxiliary material) than the vein (An_{74}).[1] Plagioclase is most likely the result of later melt impregnation related to a late stage, 0.5 mm wide, magmatic vein in the peridotite matrix that is unconnected to the clinopyroxenite vein. The clinopyroxenite vein boundaries are sharply defined by a transition from large Cpx porphyroclasts, with associated small olivine, Cpx and Opx grains, to the coarse grained olivine matrix (Figures 2g–2h). The modal composition of the matrix peridotite is slightly enriched in Cpx, suggesting addition of Cpx to the peridotite in addition to crystallization of the clinopyroxenite vein.

4.3. Trace Elements

[40] Peridotite Cpx in this study cover the range of trace element compositions previously observed in abyssal peridotite Cpx [e.g., *Johnson et al.*, 1990]. Trace element data for Cpx and Opx are presented in Table 3, and REE patterns, normalized to primitive upper mantle (PUM) [*McDonough and Sun*, 1995], are plotted in Figure 4. For comparison, the abyssal peridotite Cpx data sets from *Johnson et al.* [1990] and *Johnson and Dick* [1992] are also shown, excluding samples near hot spots. SWIR Oblique Segment samples from dredge 85 and dredge 86 have typical, depleted REE patterns for abyssal peridotites, with Cpx falling in the middle of the range of Cpx compositions from *Johnson et al.* [1990]. In contrast, the dredge 96 samples have higher overall REE concentrations and less depleted patterns. The sample from dredge PS86-6 is also relatively undepleted, with a similar composition to the most light REE (LREE) depleted of the dredge 96 samples.

[41] Both the peridotites and pyroxenites from dredge 96 have enriched compositions, with almost flat patterns, except for variable LREE depletion. LREE vary by over an order of magnitude among samples, with both peridotites and pyroxenites spanning the same range of concentrations. The most notable feature of the dredge 96 samples is that the pyroxenites do not have a distinct trace element composition from the peridotites. The basalt from dredge 96 is LREE enriched and has only slightly higher heavy REE (HREE) concentrations than the peridotite Cpx. The basalt REE pattern is close to the calculated composition of melts in equilibrium with peridotites and pyroxenites from dredge 96.

[1] Auxiliary materials are available at ftp://ftp.agu.org/apend/jb/2008JB006186.

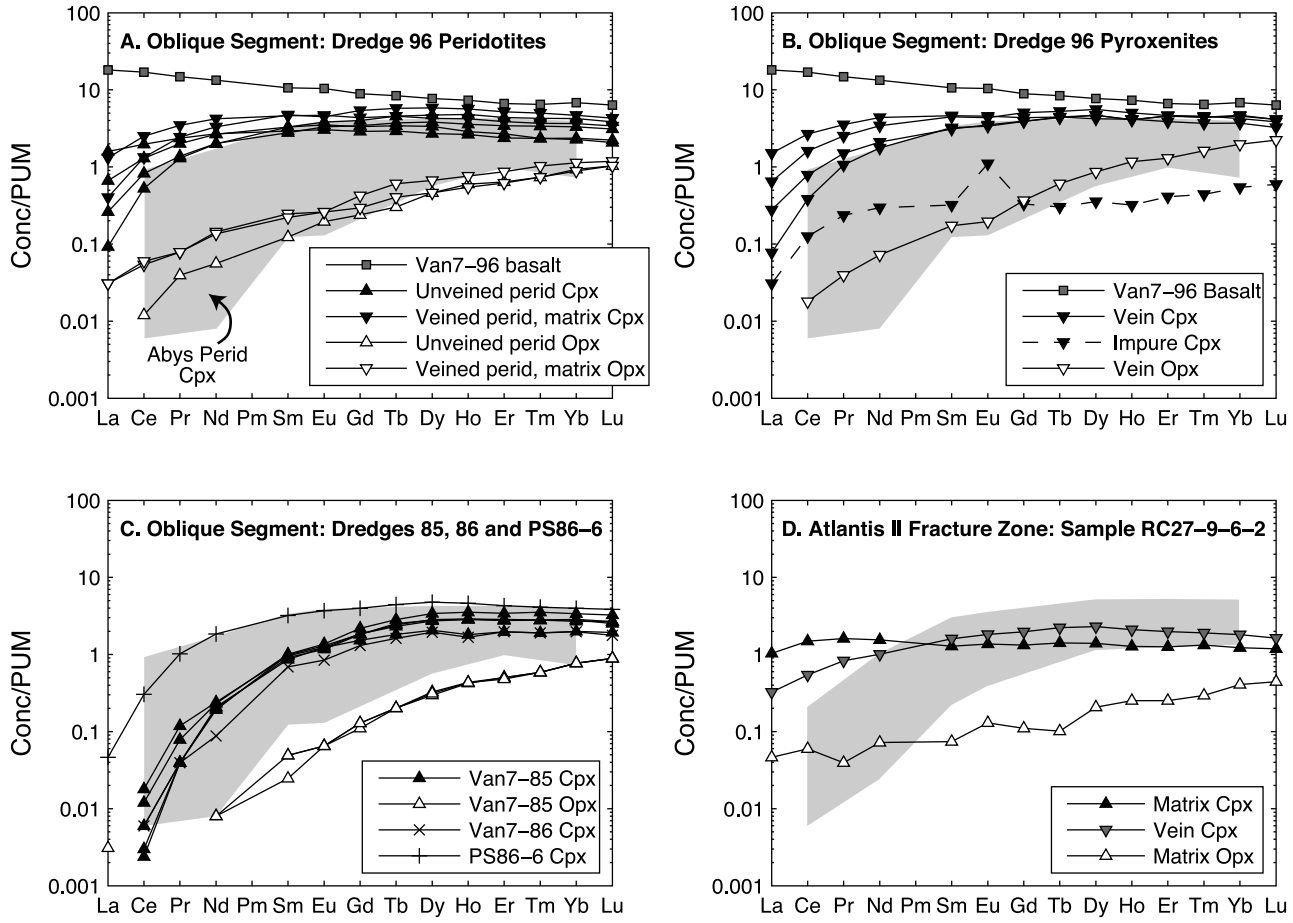

Figure 4. ICPMS rare earth element data for Cpx and Opx, normalized to PUM [*McDonough and Sun*, 1995]. (a–c) The grey shaded field is the range for abyssal peridotite Cpx from *Johnson et al.* [1990]. Note that data in Figure 4a are for unveined peridotites and for minerals from the matrix of veined peridotites, whereas the data in Figure 4b are for the veins themselves. (d) The grey shaded field is the range for peridotite Cpx from the Atlantis II Fracture Zone [*Johnson and Dick*, 1992].

[42] Sample RC27-9-6-2 from the Atlantis II Fracture Zone has a distinctive, nearly flat REE pattern. In comparison to residual abyssal peridotite Cpx from the fracture zone [*Johnson and Dick*, 1992], this sample has a relative depletion in HREE and enrichment in LREE. In addition, the REE pattern of the matrix peridotite Cpx crosses that of the vein Cpx. The matrix Cpx REE pattern is almost identical to PUM in composition. Vein Cpx is less enriched in LREE, but more enriched in HREE compared to matrix Cpx.

4.4. Isotopes

[43] Results of Nd, Sr and Pb isotope analyses are presented in Tables 4 and 5, revealing variations both within and between dredges and down to the subsample scale. In Figure 5, we plot the variation in $^{143}Nd/^{144}Nd$ against the variation in $^{87}Sr/^{86}Sr$ for both localities. Pb isotope data are shown for the three Cpx separates successfully analyzed in Figure 6. In addition, we plot published peridotite Cpx compositions from the same localities [*Snow et al.*, 1994;

Table 5. Pb Isotopic Compositions of Peridotite Cpx and Basalt Glasses

Sample	Phase	$^{206}Pb/^{204}Pb$[a]	2σ	$^{207}Pb/^{204}Pb$[a]	2σ	$^{208}Pb/^{204}Pb$[a]	2σ
Van7-96-21M	Cpx	19.032	0.015	15.537	0.012	38.423	0.025
Van7-96-28	Cpx	19.598	0.016	15.570	0.012	39.096	0.026
RC27-9-6-2M	Cpx	17.221	0.002	15.446	0.002	37.201	0.005
Van7-96-68	Basalt	18.789	0.015	15.493	0.012	38.426	0.025
Van7-92-03	Basalt	19.068	0.002	15.582	0.002	38.866	0.006
Van7-92-03S[b]	Basalt	19.065	0.002	15.601	0.001	38.893	0.004
Kn162-61-71	Basalt	19.270	0.002	15.617	0.002	39.297	0.006
Kn162-61-71S[b]	Basalt	19.288	0.001	15.642	0.001	39.368	0.002

[a]All data are normalized to the NBS981 values from *Todt et al.* [1996]: $^{206}Pb/^{204}Pb = 16.936$, $^{207}Pb/^{204}Pb = 15.489$ and $^{208}Pb/^{204}Pb = 36.701$.
[b]Values from *Standish* [2006], for interlaboratory comparison.

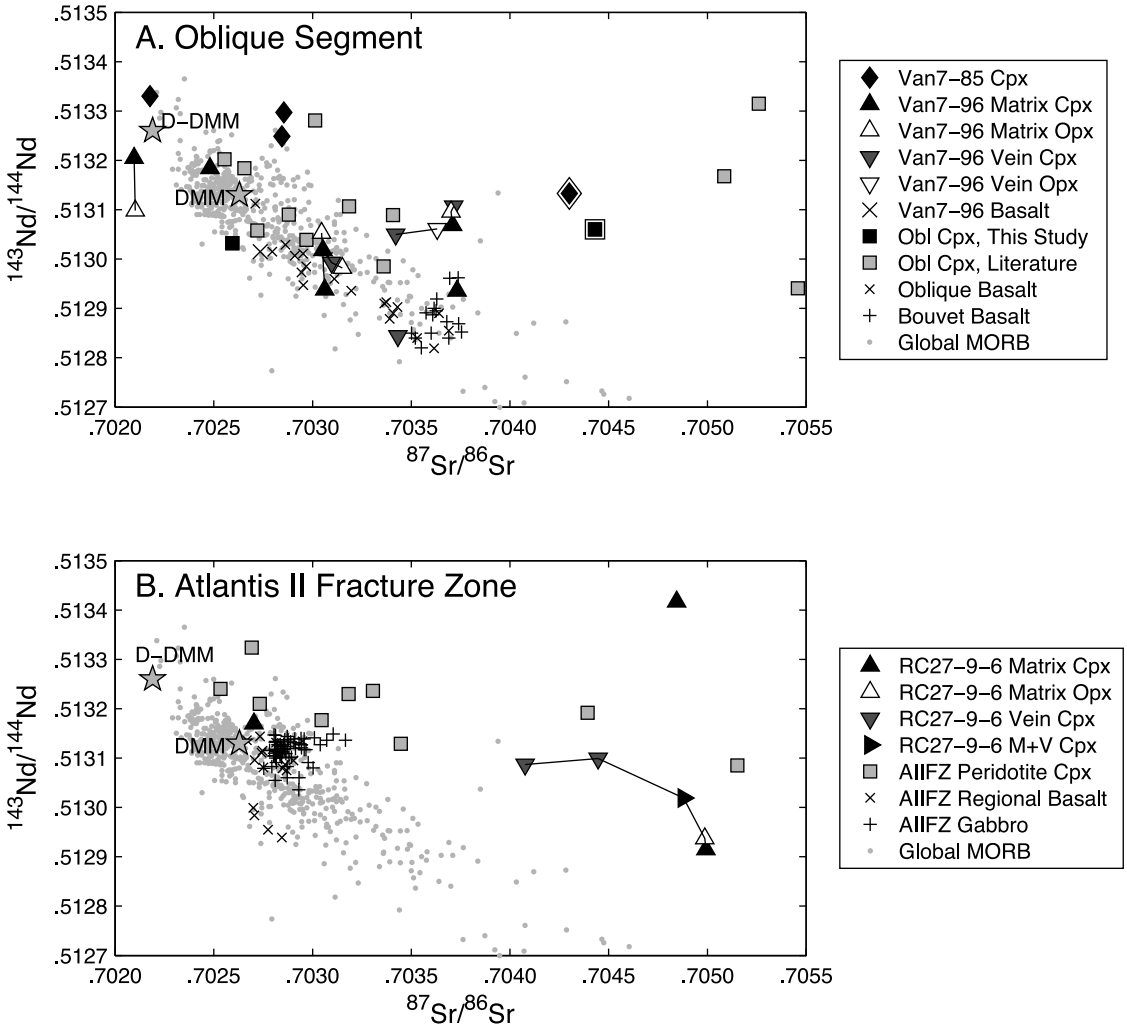

Figure 5. Nd and Sr isotopic variations in peridotites from this study and the literature, in comparison to associated basalts and gabbros and to global MORB. All data are corrected to $^{87}Sr/^{86}Sr = 0.71025$ for NBS987 and $^{143}Nd/^{144}Nd = 0.511858$ for La Jolla. The two outlined Oblique Segment samples are the most altered peridotites from this study. Note that data for dredge RC27-9-6, including sample RC27-9-6-2, is from this study, *Snow et al.* [1994], *Lee* [1997], and *Salters and Dick* [2002]. In addition, the Cpx referred to as RC27-9-6 M + V is a combined analysis of matrix and vein Cpx from RC27-9-6-2 [*Snow et al.*, 1994]. Additional data sources are DMM from *Su and Langmuir* [2003], D-DMM from *Workman and Hart* [2005], MORB from a PetDB compilation by M. Collier (personal communication, 2007). (a) Oblique Segment peridotites from *Snow et al.* [1994] and *Salters and Dick* [2002]; Shaka Fracture Zone peridotites from *Snow* [1993]; Bouvet regional peridotites from *Snow et al.* [1994]; Oblique Segment basalts from *le Roex et al.* [1983, 1992], *Mahoney et al.* [1992], *Janney et al.* [2005], and *Standish* [2006]; Shaka Fracture Zone basalts from *le Roex et al.* [1983]; Bouvet basalts from *O'Nions and Pankhurst* [1974], *O'Nions et al.* [1977], *Sun* [1980], *Kurz et al.* [1998], *Prestvik et al.* [1999], *Janney et al.* [2005], and *Barry et al.* [2006]. (b) Atlantis II Fracture Zone peridotites from *Snow et al.* [1994] and *Salters and Dick* [2002]; gabbros, all from Hole 735B on Atlantis Bank, from *Kempton et al.* [1991], *Hart et al.* [1999], and *Holm* [2002]; fracture zone and transform volcano basalts from *Mahoney et al.* [1989] and *Snow* [1993]; basalts from adjacent ridge segments from *Hamelin and Allègre* [1985], *Snow* [1993], and *Meyzen et al.* [2005].

Salters and Dick, 2002] and related basalts and gabbros from a compilation of published data (see Figure 5 caption for references).

4.4.1. Oblique Segment

[44] On the Oblique Segment, dredge 85 samples are isotopically depleted, except for alteration-related enrichment of Sr in some samples. One dredge 85 sample is more depleted in both Nd and Sr than the estimated isotopic composition of DMM, which is derived from the average composition of MORBs [*Su and Langmuir*, 2003]. This sample is also more depleted than depleted-DMM (D-DMM), defined as the isotopic composition that is 2σ depleted from average MORB [*Su and Langmuir*, 2003; *Workman and Hart*, 2005]. Similarly, in dredge 96, Van7-96-38 is more

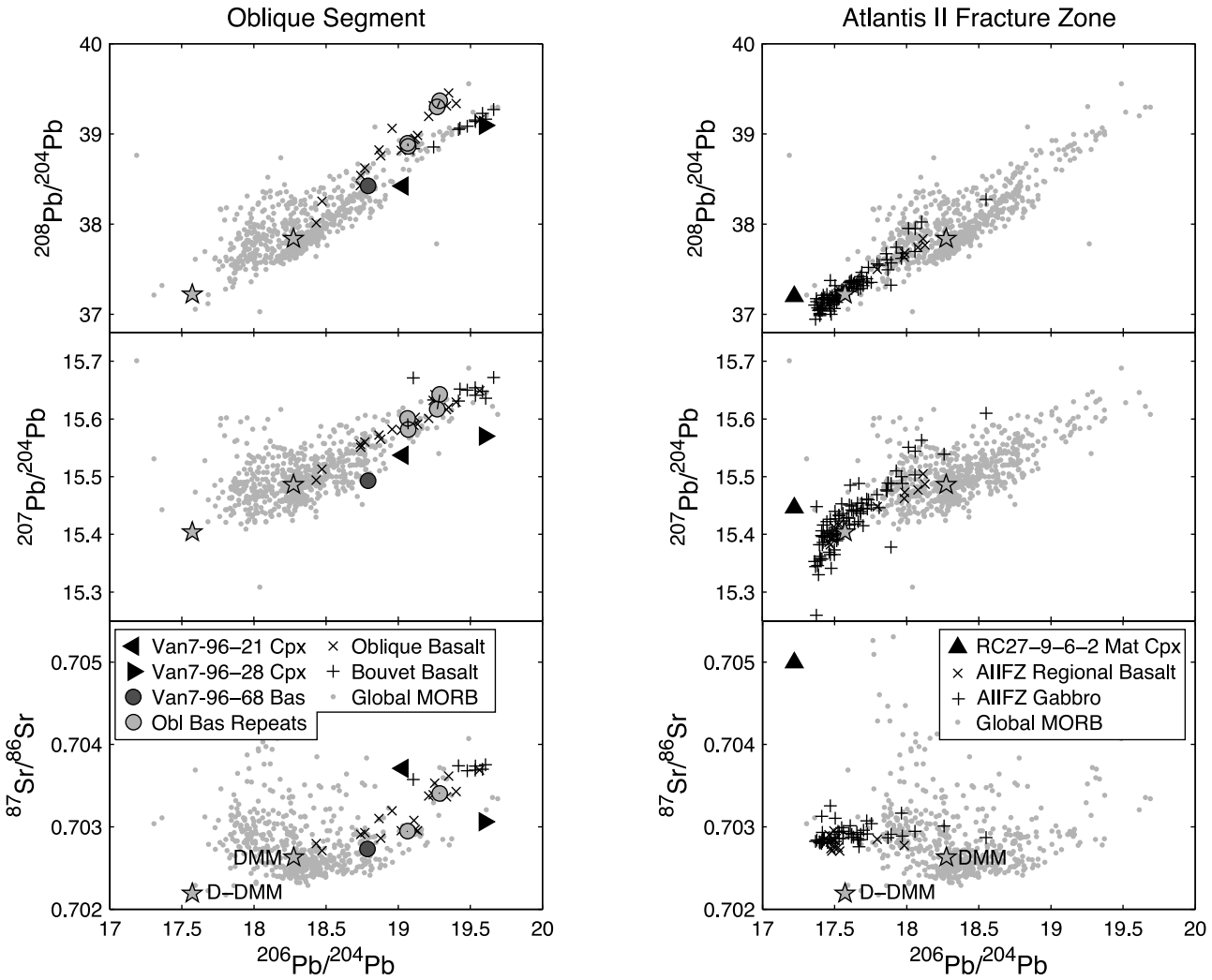

Figure 6. Variation of $^{206}Pb/^{204}Pb$ with $^{208}Pb/^{204}Pb$, $^{207}Pb/^{204}Pb$, and $^{87}Sr/^{86}Sr$ in peridotite Cpx and basalt glasses from the two study areas. Also shown are related basalts and gabbros, the estimated compositions of DMM and D-DMM, and global MORB (see Figure 5 for references). Data for the two repeat analysis basalts from this study and *Standish* [2006] are shown with a connecting tie line (visible as a dot when samples closely overlap). These basalts plot along the Oblique Segment trend, whereas the dredge 96 peridotites and basalt plot off the trend. Similarly, the Atlantis II Fracture Zone peridotite plots away from the trend of associated basalts and gabbros.

depleted than DMM for both Nd and Sr, and has among the lowest $^{87}Sr/^{86}Sr$ value ever measured in MORBs or abyssal peridotites.

[45] The isotopic composition of dredge 96 ranges from the extremely depleted composition of Van7-96-38 (unveined peridotite) to the enriched compositions of Van7-96-16 (pyroxenite) and Van7-96-35 (unveined peridotite). The pyroxenites and peridotites do not form two distinct isotopic groups, though the unveined peridotites extend to more depleted compositions than the pyroxenites. The basalt from dredge 96 plots toward the depleted end of the peridotite trend, close to DMM.

[46] In Figure 5a, we also plot the composition of Bouvet Island basalts, located to the west of the Oblique Segment near the Bouvet Triple Junction (Figure 1). Bouvet Island is near the present-day location of Bouvet Hotspot, which is presently located beneath Speiss Ridge, adjacent to the Bouvet Triple Junction [*Ligi et al.*, 1997]. The Bouvet Hotspot track can be traced back to southern Africa at ~80 Ma and is estimated to have passed along the Shaka Fracture Zone, which defines the western end of the Oblique Segment, beneath the African plate at ~15–25 Ma [*Hartnady and le Roex*, 1985].

[47] Basalts and peridotites from the Shaka Fracture Zone [*le Roex et al.*, 1983; *Snow*, 1993] have similar Nd isotopic compositions to Bouvet basalts (Figure 5a). The most enriched dredge 96 samples fall within the range of Bouvet basalt compositions. As a whole, dredge 96 peridotites, Oblique basalts, and other Oblique peridotites form a trend between Bouvet samples and DMM, with some peridotite $^{87}Sr/^{86}Sr$ exceptions due to seawater alteration. In contrast, peridotites from the ridge near Bouvet Island [*Snow et al.*, 1994] have depleted compositions similar to DMM.

[48] The Pb isotopic variation of the two dredge 96 peridotites, one veined and the other unveined, show significant variation in $^{206}Pb/^{204}Pb$ and $^{208}Pb/^{204}Pb$, but less variation in

$^{207}Pb/^{204}Pb$ (Figure 6). Van7-96-28 (unveined peridotite) is similar in composition to Bouvet basalts. Van7-96-21 (veined peridotite) and the dredge 96 basalt have less radiogenic compositions, with the basalt close in composition to DMM. All three samples are offset in $^{207}Pb/^{204}Pb$ from the trend of the Oblique basalts from *Standish* [2006], whereas our replicate analyses of two basalts from the *Standish* [2006] data set plot on the trends (Table 5 and Figure 6).

4.4.2. Atlantis II Fracture Zone

[49] The peridotite matrix of RC27-9-6-2 is enriched in $^{143}Nd/^{144}Nd$, while the clinopyroxenite vein is, surprisingly, less isotopically enriched. Sr isotopes are enriched, also with greater enrichment in the peridotite than in the vein. While seawater alteration cannot be ruled out as the cause of $^{87}Sr/^{86}Sr$ enrichment, an isotopic range from 0.704 to 0.705 on a scale of ~10 cm is unlikely for seawater alteration. The isotopic composition of RC27-9-6-2 contrasts with other Atlantis II Fracture Zone peridotites [*Snow et al.*, 1994; *Salters and Dick*, 2002], which extend from $^{143}Nd/^{144}Nd$ compositions similar to DMM toward compositions more depleted than D-DMM.

[50] In Figure 5b we plot three types of MORB data from the Atlantis II Fracture Zone region for comparison to the peridotites: samples from (1) the Atlantis II Fracture Zone, (2) a transform volcano at the northern ridge-transform intersection, and (3) the ridge segments on either side of the fracture zone. While generally depleted in composition, all three types of basalt have at least one sample with $^{143}Nd/^{144}Nd$ similar to RC27-9-6-2. The gabbros from Hole 735B on Atlantis Bank are all depleted in composition, encompassing the range of depleted MORBs from the area. In terms of Pb isotopes, basalts and gabbros from the fracture zone are depleted, ranging between DMM and D-DMM in composition. Cpx from the peridotite matrix of RC27-9-6-2 is more depleted in $^{206}Pb/^{204}Pb$ than the basalts and gabbros but similar in terms of $^{207}Pb/^{204}Pb$ and $^{208}Pb/^{204}Pb$.

5. Discussion

5.1. Radiogenic Ingrowth

[51] The characterization of residual peridotites by their isotopic compositions requires assessment of the role of radiogenic ingrowth following melt extraction. In particular, at slow and ultraslow spreading rates, peridotites spend a considerable amount of time between passing through their closure temperature and their collection on rift valley or transform fault walls. As residual peridotites have higher Sm/Nd ratios than the initial mantle, ingrowth of ^{143}Nd may affect peridotite isotopic compositions. In contrast, ^{87}Sr ingrowth following melt extraction is negligible because Rb concentrations in peridotite Cpx are extremely low.

[52] To calculate the magnitude of ^{143}Nd ingrowth, we define the ingrowth time, t_I, as a combination of the seafloor spreading time, t_S, and the upwelling time, t_U. Seafloor spreading time is determined by dividing the distance of a sample to the ridge axis, d, by the effective half-spreading rate, v_H. The upwelling time is the time between the peridotite passing through its closure temperature and exposure on the seafloor. We select the 1200°C isotherm as a nominal closure temperature for REE diffusion in pyroxenes based on the diffusion data of *Van Orman et al.* [2001] and *Cherniak and Liang* [2007], as well as the discussion given by *Van Orman et al.* [2002].

[53] To determine t_U, we use the results of a numerical model for the thermal structure of the ridge axis [*Montési and Behn*, 2007] to determine the depth, L^*_{1200}, to the 1200°C isotherm:

$$L^*_{1200} = 5\frac{\kappa}{v_H} \tag{1}$$

where κ is the thermal conductivity (10^{-6} m^2 s^{-1}). The solution for corner flow beneath the ridge axis [*Batchelor*, 1967; *McKenzie*, 1969] provides the relationship between upwelling velocity, v_U, and spreading rate:

$$v_U = \frac{2}{\pi} v_H \tag{2}$$

leading to an expression for t_U:

$$t_U = \frac{5\pi}{2}\frac{\kappa}{v_H^2} \tag{3}$$

Thus, the time available for ingrowth is

$$t_I = t_U + t_S = \frac{5\pi}{2}\frac{\kappa}{v_H^2} + \frac{d}{v_H} \tag{4}$$

The results of these calculations are given in Table 6. For dredge 85 and 96 samples, t_U is ~7 My; t_S is 0.5 My for dredge 85 and 4 My for dredge 96. On the Oblique Segment, at locations where the ridge has a high angle of obliquity to the spreading direction, t_U approaches 18 My. For ridges with half spreading rates >10 mm/yr and no obliquity, $t_U \leq 1$ My.

[54] In Figure 7a, we plot $^{143}Nd/^{144}Nd$ corrected for t_I (the "age"-corrected value) versus the measured $^{143}Nd/^{144}Nd$ value. Samples plot on or to the right of the 1:1 line, with a maximum deviation of 0.01% among our samples. The field between DMM and D-DMM is shaded to demonstrate that the age correction does not shift depleted peridotites back to DMM values. In addition, in Figure 7a, we plot age-corrected values calculated for the global abyssal peridotite Cpx data set [*Snow*, 1993; *Snow et al.*, 1994; *Salters and Dick*, 2002; *Cipriani et al.*, 2004]. The maximum change globally in $^{143}Nd/^{144}Nd$ composition is 0.04%, even among samples that are ~20 Ma. The small amount of ingrowth in the global data set indicates that ingrowth can be ignored when interpreting peridotite isotopic data.

[55] The effect of ^{143}Nd ingrowth as a function of time and the Sm/Nd ratio can also be understood using ϵ_{Nd} notation, as the absolute change in $^{143}Nd/^{144}Nd$ is small owing to the long half-life of ^{147}Sm. The difference between the measured, M, and corrected, C, values of ϵ_{Nd} is

$$\Delta\epsilon_{Nd} = \epsilon^M_{Nd} - \epsilon^C_{Nd} = \frac{\left(\frac{^{143}Nd}{^{144}Nd}\right)_M - \left(\frac{^{143}Nd}{^{144}Nd}\right)_C}{\left(\frac{^{143}Nd}{^{144}Nd}\right)_{CHUR}} \times 10^4 \tag{5}$$

where *CHUR* is the chondritic uniform reservoir, which has a present-day $^{143}Nd/^{144}Nd$ value of 0.512638. The amount of

Table 6. Age-Corrected Isotopic Compositions for Peridotite Clinopyroxenes and Orthopyroxenes

Sample[a]	Phase	L^*_{1200}[b] (km)	t_U[c] (Ma)	d[d] (km)	t_S[e] (Ma)	t_I[f] (Ma)	$^{87}Sr/^{86}Sr$ Ingrowth	$^{87}Sr/^{86}Sr$ Age Corrected	$^{87}Rb/^{86}Sr$ Age Corrected	$^{143}Nd/^{144}Nd$ Ingrowth	$^{143}Nd/^{144}Nd$ Age Corrected	$^{147}Sm/^{144}Nd$ Age Corrected
Van7-85-27	Cpx	26	6.9	3	0.5	7.4	0.000002	0.702853	0.0187	0.000032	0.513265	0.670
Van7-85-30	Cpx	26	6.9	3	0.5	7.4	0.000001	0.704300	0.0134	0.000048	0.513085	0.988
Van7-85-42	Cpx	26	6.9	3	0.5	7.4				0.000050	0.513285	1.031
Van7-85-47	Cpx	26	6.9	3	0.5	7.4	0.000001	0.702175	0.0054	0.000045	0.513285	0.938
Van7-85-49	Cpx	26	6.9	3	0.5	7.4	0.000000	0.702844	0.0029	0.000044	0.513205	0.912
Van7-86-27	Cpx	26	6.9	10	1.7	8.6	0.000007	0.704424	0.0554	0.000060	0.513000	1.070
Van7-96-09	Cpx	26	6.5	22	3.6	10.0	0.000000	0.703421	0.0003	0.000019	0.513031	0.295
Van7-96-09	Opx	26	6.5	22	3.6	10.0	0.000001	0.703630	0.0105	0.000031	0.513030	0.468
Van7-96-16	Cpx	26	6.5	22	3.6	10.0	0.000003	0.703429	0.0203	0.000022	0.512822	0.339
Van7-96-19M	Cpx	26	6.5	22	3.6	10.0	0.000000	0.703052	0.0028	0.000018	0.513000	0.275
Van7-96-19M	Opx	26	6.5	22	3.6	10.0	0.000007	0.703144	0.0482	0.000024	0.512958	0.372
Van7-96-19V	Cpx	26	6.5	22	3.6	10.0	0.000001	0.703096	0.0085	0.000017	0.512976	0.259
Van7-96-21M	Cpx	26	6.5	22	3.6	10.0	0.000000	0.703709	0.0000	0.000015	0.513055	0.220
Van7-96-21M	Opx	26	6.5	22	3.6	10.0	0.000000	0.703701	0.0005	0.000021	0.513075	0.315
Van7-96-21V	Cpx	26	6.5	22	3.6	10.0	0.000000	0.703715	0.0003	0.000014	0.513093	0.212
Van7-96-25	Cpx	26	6.5	22	3.6	10.0	0.000000	0.702480	0.0001	0.000019	0.513165	0.287
Van7-96-28	Cpx	26	6.5	22	3.6	10.0	0.000000	0.703061	0.0000	0.000014	0.512924	0.216
Van7-96-28	Opx	26	6.5	22	3.6	10.0	0.000000	0.703046	0.0002	0.000022	0.513031	0.329
Van7-96-35	Cpx	26	6.5	22	3.6	10.0	0.000000	0.703732	0.0001	0.000016	0.512920	0.250
Van7-96-38	Cpx	26	6.5	22	3.6	10.0	0.000000	0.702096	0.0015	0.000021	0.513184	0.321
Van7-96-38	Opx	26	6.5	22	3.6	10.0	0.000004	0.702098	0.0254	0.000032	0.513066	0.489
PS86-6-38	Cpx	36	12.7	16	3.6	16.4				0.000038	0.512994	0.357
RC27-9-6-2M	Cpx	19	3.4	6	0.6	4.1	0.000000	0.704993	0.0002	0.000004	0.512911	0.166
RC27-9-6-2M	Opx	19	3.4	6	0.6	4.1	0.000000	0.704987	0.0022	0.000006	0.512931	0.215
RC27-9-6-2V	Cpx	19	3.4	6	0.6	4.1	0.000000	0.704447	0.0003	0.000008	0.513091	0.307

[a]M indicates the peridotite matrix of a veined sample and V indicates a pyroxenite vein.
[b]Depth to the 1200°C isotherm (see text).
[c]Upwelling time.
[d]Distance from ridge axis.
[e]Seafloor spreading time.
[f]Ingrowth time.

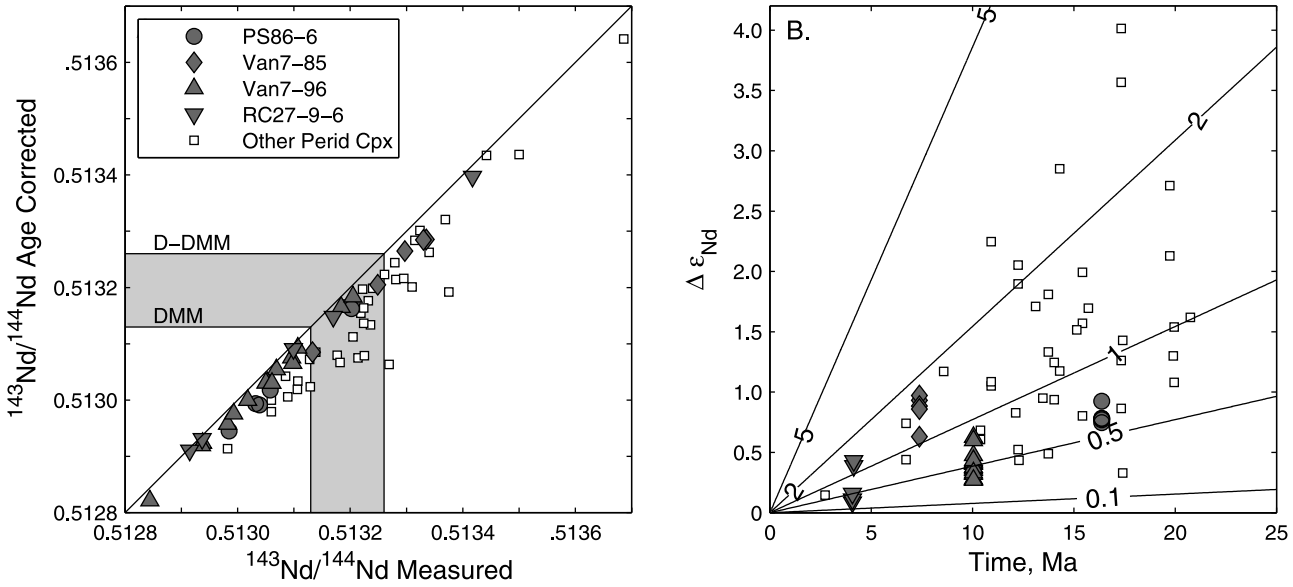

Figure 7. (a) Age-corrected $^{143}Nd/^{144}Nd$ compared to measured $^{143}Nd/^{144}Nd$. Age correction accounts for the time since the peridotites left the 1200°C isotherm. The solid line is a 1:1 correlation line. Samples either plot on the line or toward higher measured values, due to ingrowth. Additional data for abyssal peridotite Cpx are from *Snow* [1993], *Snow et al.* [1994], *Salters and Dick* [2002], and *Cipriani et al.* [2004]. (b) The difference in ϵ_{Nd} between measured and corrected $^{143}Nd/^{144}Nd$ values as a function of time since the sample left the 1200°C isotherm. Contours are for constant Sm/Nd ratios.

Table 7. Reconstructed Peridotite Whole Rock Isotopic Compositions From Mineral Modes and Measured Cpx and Opx Compositions[a]

Sample[b]	Rb (ppb)	$^{87}Rb/^{86}Sr$	Cpx[c] (%)	Sr (ppm)	$^{87}Sr/^{86}Sr$	Cpx (%)	Sm (ppm)	$^{147}Sm/^{144}Nd$ AC[d]	Cpx (%)	Nd (ppm)	$^{143}Nd/^{144}Nd$ AC[d]	Cpx (%)
Van7-96-09V	0.45	0.00223	81	3.369	0.703423	99	0.817	0.299	97	1.662	0.513031	98
Van7-96-19M	3.53	0.03544	28	1.189	0.703065	87	0.384	0.280	95	0.832	0.512998	96
Van7-96-21M	0.03	0.00028	49	1.206	0.703709	92	0.108	0.234	86	0.284	0.513057	89
Van7-96-28	0.03	0.00008	49	4.785	0.703060	94	0.075	0.228	89	0.201	0.512932	93
Van7-96-38	1.12	0.01345	50	1.142	0.702096	94	0.154	0.336	91	0.281	0.513177	94
RC27-9-6-2M	0.89	0.00103	58	9.445	0.704993	95	0.083	0.170	91	0.298	0.512912	93

[a]Modes have been normalized to remove late stage plagioclase.
[b]M indicates the peridotite matrix of a veined sample and V indicates a pyroxenite vein.
[c]Contribution of Cpx to whole rock concentration and isotopic composition.
[d]Age-corrected isotopic composition (see text).

the age correction for variable Sm/Nd ratios can be calculated independently of the measured $^{143}Nd/^{144}Nd$ in a sample:

$$\Delta\epsilon_{Nd} = \frac{\lambda t_I c \frac{Sm}{Nd}}{\left(\frac{^{143}Nd}{^{144}Nd}\right)_{CHUR}} \times 10^4 \quad (6)$$

where c is the conversion factor of 0.6049 between Sm/Nd and $^{147}Sm/^{144}Nd$. The results of calculations using equations (5) and (6) are shown in Figure 7b. For samples in our study, the ingrowth time is generally $\leq$10 Ma, Sm/Nd is <2 and $\Delta\epsilon_{Nd}$ is <1.

[56] The isotopic variations observed in this study are clearly not created in the time since melting beneath the ridge and are thus related to either long-term mantle heterogeneities or recent reaction with a melt with distinct isotopic composition. Figure 7 also includes samples from the global data set, demonstrating that those with longer ingrowth times are either far from the ridge axis or have a very low effective spreading rate. Samples with the highest amounts of ingrowth ($\Delta\epsilon_{Nd} \approx 3-4$) have both high Sm/Nd ratios and long ingrowth times. However, even for these samples, the amount of ingrowth is significantly less than the overall $^{143}Nd/^{144}Nd$ isotopic variation among abyssal peridotites, which have a global range of $\Delta\epsilon_{Nd} = 16$.

5.2. Reconstructed Whole Rock Compositions

[57] The TIMS measurements of Sr, Rb, Nd and Sm represent the first time that these elements have been measured in both Cpx and Opx in abyssal peridotites. We use the six samples with paired measurements of Cpx and Opx and the modal compositions of these samples to construct peridotite whole rock compositions. The result of this calculation is given in Table 7. We have not included concentrations of Sr, Rb, Nd and Sm in olivine and spinel in the calculation as these are negligible in abyssal peridotites, due to the greater partitioning of these elements into Cpx by 2 or more orders of magnitude [e.g., *Kelemen et al.*, 2003]. Our calculations indicate that the concentration of Sr, Nd and Sm in Opx can also be considered negligible, as Cpx contains >85% of these elements.

[58] The calculated bulk rock compositions demonstrate that Cpx controls the isotopic and trace element composition of peridotites and thus Cpx can be used as a proxy for the bulk rock. Three of the reconstructed peridotites come from veined samples and overall the six bulk rock compositions span the range from depleted to enriched mantle. We find that Cpx dominates the trace element budget and isotopic composition of the peridotite independently of the presence or absence of veins and depletion or enrichment of the peridotite. This observation is also valid for more depleted peridotites, such as those from dredge 85, for which the calculation must be done using ICPMS data as TIMS data is not available for Opx from this dredge.

[59] The control on peridotite trace element and isotopic composition by Cpx is due to the high concentrations of trace elements in Cpx, despite the low modal proportion of Cpx in peridotites. Even in samples with higher modal Opx (i.e., harzburgites), the contribution of Cpx to the bulk rock Sr, Nd and Sm budget remains >85%, due to depletion of these elements in both Cpx and Opx. The effect of errors in the mineral mode estimates is relatively unimportant. Assuming a modal error of 5% for Cpx, the calculated Nd isotopic composition of the whole rock is shifted by <0.1 ϵ_{Nd} and the change in the contribution of Cpx to the whole rock isotopic composition changes by only a couple percent.

[60] The amount of Rb contained in Cpx versus Opx varies between 49% and 81% (Table 7). Overall, we find that Rb concentrations in both Cpx and Opx in our samples are higher than expected if abyssal peridotites have undergone only melt depletion at the ridge axis. As Rb is extremely incompatible in both Cpx and Opx, it should not be present in measurable quantities in either mineral. Thus, we suggest that the variability of Rb concentrations reflects late stage melt percolation through peridotite, which results in very small degrees of refertilization. This would have a greater effect on the most incompatible elements, as these have negligible concentrations after melting. This type of weak refertilization has been observed and modeled for Vema Fracture Zone peridotites by *Brunelli et al.* [2006].

[61] In Figure 8, we plot age-corrected whole rock $^{143}Nd/^{144}Nd$ and $^{147}Sm/^{144}Nd$ for the SWIR samples. For samples in which Opx was not measured, we calculate bulk composition using Cpx composition, mineral modes and mineral/melt partition coefficients, following the formulation given by *Workman and Hart* [2005]. We find that the difference between Cpx isotopic composition and the recalculated composition is greater than the difference observed for the 6 samples with recalculated compositions based on measured Cpx and Opx compositions. We conclude that the *Workman and Hart* [2005] formulation overestimates the contribution of other phases, specifically Opx, to the isotopic and trace element composition of the bulk peridotite. Their formulation uses Cpx/melt and Opx/melt partitioning data instead of Cpx/Opx partitioning data. We suggest that the high-temperature mineral/melt partition coefficients underestimate the Cpx/Opx partitioning of trace elements that continues to lower temperature in the mantle. In Appendix B, we

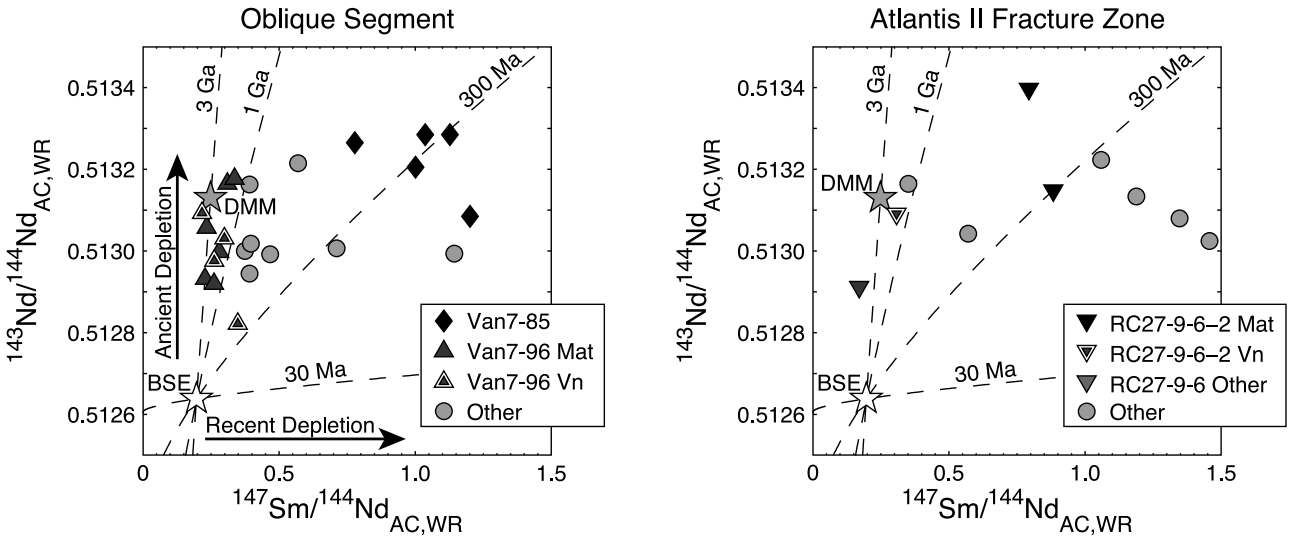

Figure 8. Variation of $^{143}Nd/^{144}Nd$ as a function of $^{147}Sm/^{144}Nd$ for the Oblique Segment and the Atlantis II Fracture Zone. Data are reconstructed whole rock (WR) compositions with the age correction applied, as discussed in the text. For the six samples that have measured Cpx and Opx compositions, the whole rock reconstruction is based on this and mineral modes. For the remaining samples, the reconstruction is based on Cpx composition, mineral modes, and mineral/melt partition coefficients, following the formulation given by *Workman and Hart* [2005, equation (1)]. Model isochrons are calculated using a continuous depletion model [*Workman and Hart*, 2005] with an initial composition constrained by BSE. Data for other SWIR Cpx are from this study, *Snow et al.* [1994], and *Salters and Dick* [2002].

present Cpx/Opx partition coefficients calculated from the bulk mineral ICP-MS analyses in this study. Overall, as our data suggests that Cpx is a good proxy for peridotite bulk composition, we use Cpx data in our analysis below, instead of the reconstructed whole rock compositions.

[62] On the isotope plot in Figure 8, we also plot model isochrons for depletion from bulk silicate Earth starting at 3 Ga, 1 Ga, 300 Ma and 30 Ma, following the continuous depletion model of *Workman and Hart* [2005]. The continuous depletion model, discussed in more detail below, predicts the isotopic evolution of the mantle based on the composition of bulk silicate Earth and DMM, assuming that the only process affecting the mantle is removal of material to form continental crust. The scatter of peridotite data away from the 3 Ga isochron immediately demonstrates that the mantle system is affected by other processes. While some peridotites, e.g., from dredge 96, appear to have a limited range, they actually cover the range 1–3 Ga, as older isochrons plot closer together. In addition, one point from dredge 96 plots close to 300 Ma.

[63] The scatter in Figure 8 demonstrates that the peridotites are not simple mixtures between enriched and depleted sources, as this should produce an inverse linear mixing line on a plot of $^{143}Nd/^{144}Nd$ versus $^{147}Sm/^{144}Nd$. The nonisochronous relationship between spatially related peridotites and the lack of a mixing relationship indicates the complicated nature of the oceanic upper mantle, which we address in detail below.

5.3. Origin of the Pyroxenite Veins

[64] The coexisting pyroxenites and peridotites in dredge 96 were selected for analysis to determine whether the pyroxenites are direct samples of recycled oceanic lithosphere, following the marble cake model for the mantle proposed by *Allégre and Turcotte* [1986]. The presence of recycled material in the mantle has been invoked to explain isotopic variations in OIBs [e.g., *White and Hofmann*, 1982; *Zindler and Hart*, 1986] and MORBs [e.g., *Allégre et al.*, 1984; *Kellogg et al.*, 2002]. In addition, the presence of pyroxenites in the upper mantle has been proposed as a mechanism to explain geochemical signatures in MORB of melting in the presence of garnet, as the thickness of oceanic crust is too thin for what should be produced if peridotite melting commenced at the depth of garnet stability [*Hirschmann and Stolper*, 1996]. However, despite the general consensus that isotopic heterogeneities in basalts are explained by recycled oceanic lithosphere and sediments [e.g., *Hofmann*, 1997], no consensus exists as to the form that recycled crust takes in the mantle following millions of years of convection. In addition, no consensus exists as to the degree of variability of upper mantle composition and the degree to which it is veined.

[65] The occurrence of pyroxenites in peridotite massifs led *Allégre and Turcotte* [1986] to suggest the marble cake mantle hypothesis, in which recycled crust has been stretched and boudinaged to length scales below meaningful thermodynamic integrity and absorbed into the peridotitic lithology. While numerous studies have documented mineralogical, chemical and isotopic variations among pyroxenites from ophiolites and orogenic lherzolites [e.g., *Frey and Prinz*, 1978; *Polvé and Allègre*, 1980; *Zindler et al.*, 1983; *Hamelin and Allègre*, 1988; *Piccardo et al.*, 1988; *McDonough and Frey*, 1989; *Mukasa et al.*, 1991; *Shervais and Mukasa*, 1991; *Pearson et al.*, 1993; *Python and Ceuleneer*, 2003], these pyroxenites have all been identified as representing recent magmatic addition to the host peridotite, rather than direct samples of ancient recycled crust older than the host. Only

studies which include $\delta^{18}O$ analyses have made a compelling case for recycled ancient crust in the mantle as the original source of present-day pyroxenites or eclogites in massifs and xenoliths [*Pearson et al.*, 1993; *Jacob et al.*, 1994; *Barth et al.*, 2001].

[66] In abyssal peridotites from ridges, recycled oceanic lithosphere in the form of pyroxenite veins has not been observed, despite models for mid-ocean ridge melting that invoke them [e.g., *Phipps Morgan and Morgan*, 1999; *Salters and Dick*, 2002]. The existing literature on abyssal pyroxenites is limited to descriptions of less than ten samples combined from the East Pacific Rise [*Constantin et al.*, 1995], MAR [*Serri et al.*, 1988; *Juteau et al.*, 1990; *Kempton and Stephens*, 1997] and SWIR [*Dantas et al.*, 2007]. All these occurrences describe pyroxenites with depleted compositions similar to adjacent peridotites, suggesting that these abyssal pyroxenites are not direct samples of recycled oceanic crust. Instead, they are likely the result of variable amounts of melt crystallization in the mantle at various depths. In the OIB setting, two suites of pyroxenites have been studied in detail: garnet pyroxenite xenoliths from Hawaii [*Bizimis et al.*, 2005] and garnet clinopyroxenite xenoliths from the Ontong Java Plateau [*Ishikawa et al.*, 2007]. Both are suggested to be of cumulate origin, though their isotopic compositions indicate the presence of recycled lithosphere within their source regions.

[67] Various aspects of the pyroxenites from dredge 96 suggest that they are not direct pieces of recycled oceanic crust. Texturally, if the pyroxenites were part of the convecting mantle, they should have acquired a lattice preferred orientation and the veins should be aligned with the peridotite foliation. However, pyroxenes are not aligned and in Figure 2 the pyroxenites are observed to crosscut the peridotites. If the pyroxenites were direct remnants of recycled ancient oceanic crust, then they should have less radiogenic Nd isotopic compositions and more enriched trace element compositions relative to the host peridotites. However, in Figures 4 and 5, the pyroxenites and peridotites from dredge 96 have overlapping compositions. Isotopically, as shown in Figure 5, both peridotites and pyroxenites extend from depleted, DMM-type compositions to enriched compositions that overlap the field of Bouvet basalts. Additionally, three pairs of Cpx from pyroxenites and host peridotites (Table 4) have isotopic compositions that are identical, or the pyroxenite is more depleted than the peridotite, unlike what is expected for recycled ancient oceanic crust.

[68] We suggest that though the pyroxenites in this study are not direct samples of recycled oceanic crust, their isotopic enrichment could have been derived from a recycled crustal component within the Bouvet plume. As shown in Figure 1, Bouvet Hotspot passed along the Shaka Fracture Zone, which bounds the western end of the Oblique Segment, at 15–25 Ma [*Hartnady and le Roex*, 1985]. Dredge 96 is located on the ridge axis adjacent to the Shaka Fracture Zone. Assuming the present-day spreading rate when Bouvet passed along the fracture zone at 15–25 Ma, the dredge 96 peridotites moved from 84 km depth to 45 km depth during this time and crossed the peridotite solidus around 20 Ma (based on a dry peridotite solidus at ~60 km [*Langmuir et al.*, 1992]). We suggest that melts generated by the plume migrated through this upwelling, partially melting mantle and locally reacted to produce the pyroxenites. This resulted in a wide array of reaction products on the subkilometer scale, ranging from depleted unreacted peridotite (Van7-96-38) to extensively reacted peridotite (Van7-96-35) and pyroxenite (Van7-96-16). The observation that the pyroxenites share chemical and isotopic compositions with associated peridotites suggests that near-equilibrium conditions prevailed at temperatures close to but slightly above the peridotite solidus.

[69] Recent infiltration of the upper mantle by Bouvet melt is supported by the Pb isotopic compositions of peridotite Cpx and sulfides from dredge 96. Cpx have similar radiogenic compositions to Bouvet basalts (Table 5 and Figure 6). Peridotite Cpx also have similar Pb isotopic compositions to primary sulfide (monosulfide solid solution) grains in peridotite Van7-96-28, as determined by *in situ* analyses with the Misasa multicollector IMS 1270 (two-grain average: $^{207}Pb/^{206}Pb = 0.7907$ and $^{208}Pb/^{206}Pb = 1.9984$, compared to 0.7947 and 1.9955 for Cpx, Table 5). The apparent isotopic equilibrium between Cpx and sulfide in the peridotite must be recent, as uranium is absent in sulfide, μ ($^{238}U/^{204}Pb$) = 0, whereas $\mu = 18$ in Cpx (Table 3). Hence, we suggest that the radiogenic Pb signatures of both Cpx and sulfide were formed by the migration of a Bouvet-derived melt through the mantle. The peridotite, Van7-96-28, for which the sulfide measurements were made is unveined. It is also the most enriched sample from the dredge in terms of Nd and Sr isotopic compositions and REE abundances (Figure 4). Hence, the characteristics of this peridotite support a recent derivation for the mantle enrichment.

[70] The results of our Nd isotopic analyses of coexisting Cpx and Opx pairs are also consistent with recent melt-rock reaction. Two of the four Cpx-Opx pairs analyzed from dredge 96 peridotites, Van7-96-28 and Van7-96-38, display significant $^{143}Nd/^{144}Nd$ disequilibrium (Figure 9). If a pyroxene pair was in isotopic equilibrium above the Nd closure temperature, then the pyroxenes are expected to form a two-point isochron with a ~10 My ingrowth age, based on the estimated time since dredge 96 passed through the Nd closure temperature. This assessment is correct if simple partial melting and melt extraction occurred under isotopic equilibrium. It is also correct if a melt that originated from an isotopically distinct source migrated through the peridotite and reacted with the pyroxenes, as long as isotopic equilibrium was attained during melt-rock reaction. The existence of isotopic disequilibrium itself can then be taken as evidence for interaction between an isotopically distinct peridotite and melt that failed to reach isotopic exchange equilibrium.

[71] Van7-96-28, the most enriched lherzolite from dredge 96, forms a 165 Ma Cpx-Opx isochron, whereas Van7-96-38 is the most depleted lherzolite from the dredge and displays a negative age. As discussed above, melt from the Bouvet plume probably impacted the upwelling mantle at various depths and hence variable amounts of time were available for diffusive equilibration. For example, if melt-rock reaction did not occur until a depth of 60 km, then only ~6 My was available for equilibration before the peridotite passed through the REE closure temperature, estimated to be at 30 km depth from the *Montési and Behn* [2007] thermal model. Using diffusion data for Nd in Cpx [*Van Orman et al.*, 2001] and Nd in Opx [*Cherniak and Liang*, 2007], we calculate that 6 My is insufficient for typical peridotite pyroxene grain sizes (~2 mm for Cpx and ~10 mm for

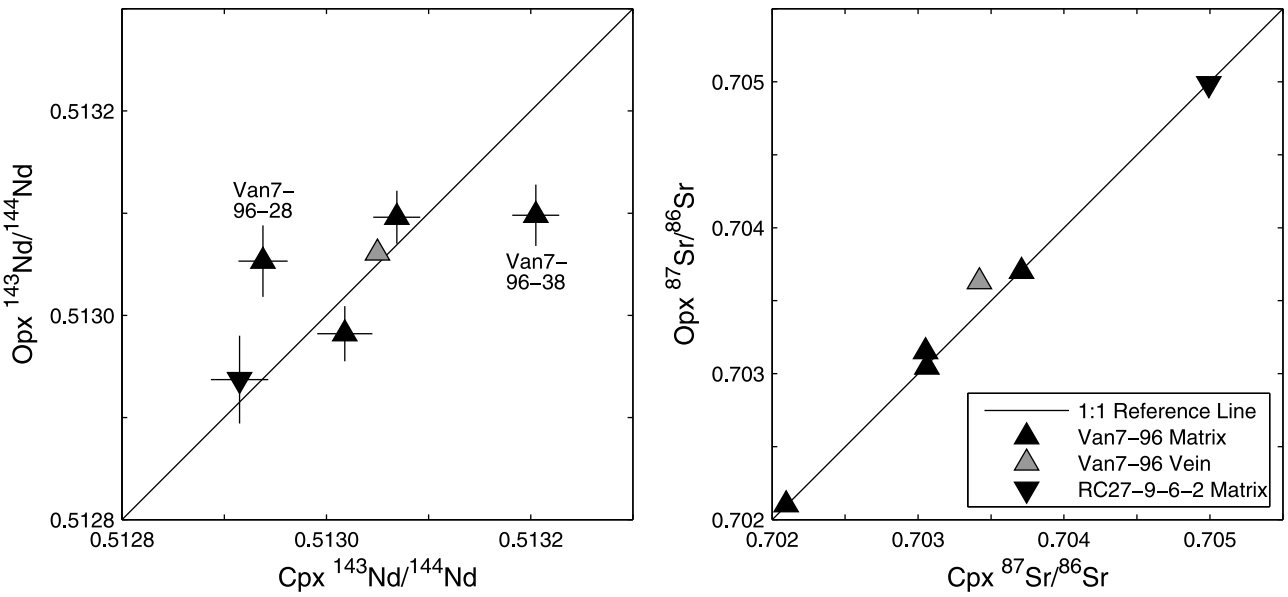

Figure 9. Comparison of Nd and Sr isotopic compositions for coexisting Cpx-Opx pairs. Error bars for Sr are smaller than the symbol size. Samples Van7-96-28 and -38 are significantly out of equilibrium for $^{143}Nd/^{144}Nd$.

Opx) to reach isotopic exchange equilibrium with the melt. In contrast to the Nd isotopic data, $^{87}Sr/^{86}Sr$ among the Cpx-Opx pairs is close to or at isotopic equilibrium (Figure 9). Diffusion data for Sr in Cpx [*Sneeringer et al.*, 1984] indicates that Sr diffusion is faster than Nd diffusion in Cpx. Estimates by *Cherniak and Liang* [2007] suggest that Sr diffusion is also relatively fast in Opx. In general, the faster diffusion of Sr than of Nd can explain the concomitant Sr isotopic equilibrium but Nd isotopic disequilibrium in peridotite Cpx-Opx pairs.

[72] Diffusion data further suggest that at temperatures >1300°C, Nd diffusion in Opx is faster than in Cpx [*Cherniak and Liang*, 2007] and that Opx could approach isotopic exchange equilibrium with melt faster than Cpx. This implies that in peridotites with Cpx-Opx Nd isotopic disequilibrium, Cpx is closest to the original prereaction composition of the peridotite. As Van7-96-38 Cpx has the most depleted Nd isotopic composition in dredge 96, this Cpx could represent the closest approach to the original depleted end-member for this dredge location. On the other hand, sample Van7-96-28 is chemically and isotopically among the most enriched peridotite for this location, suggesting that reaction with an enriched melt occurred relatively recently as full isotopic equilibrium was not reached.

5.4. Relationship Between Peridotites and Basalts

[73] Previous studies of radiogenic isotopes in abyssal peridotites have attempted to reconcile the isotopic compositions of peridotites with associated basalts, to determine if they complement basalt compositions or whether they indicate the existence of an additional mantle component. For example, *Snow et al.* [1994] and *Kempton and Stephens* [1997] found that abyssal peridotites locally have similar isotopic compositions to MORBs and are from the same depleted source. *Salters and Dick* [2002] looked in detail at the Oblique Segment and the Atlantis II Fracture Zone and concluded that peridotites are isotopically more depleted in comparison to associated basalts. They advocated for the existence of an enriched pyroxenite component in the mantle that is removed by melting and sampled by basalts, but not preserved in the peridotites. *Cipriani et al.* [2004] analyzed basalts and peridotites from the Vema Lithospheric Section on the MAR and found that the age-corrected averages for the two lithologies are not statistically different. In addition, they observed significant isotopic variability among peridotites from individual localities along the Vema Fracture Zone.

[74] To provide improved constraints on the role of mantle lithology in generating MORB isotopic compositions, we looked in detail at the mixed pyroxenite-peridotite samples from dredge 96. In addition, to determine whether the subdredge scale variability in peridotite isotopic compositions observed by *Cipriani et al.* [2004] is a common occurrence, we analyzed multiple peridotites per dredge. Finally, by combining our data set with the existing data sets for peridotite Cpx isotopic compositions, we can assess the degree to which residual peridotites produce the isotopic range observed among MORB.

[75] The peridotites and pyroxenites from dredge 96 represent the first detailed isotopic analysis of veined peridotites in the oceanic setting. We found large isotopic variations among peridotites and pyroxenites (Figure 5), which were sampled over a distance of <1 km. The samples cover 46% of the Nd isotopic range for Indian Ocean MORB and encompasses the Nd and Sr isotopic range of Oblique Segment basalts [*Standish*, 2006]. However, as discussed in the previous section, the pyroxenites do not have a distinct isotopic composition from the peridotites and we interpret the pyroxenites and peridotites to have been strongly influenced by Bouvet Hotspot.

[76] Other peridotites from the Oblique Segment suggest a Bouvet influence beyond the vicinity of the Shaka Fracture Zone. The variation in Nd and Sr isotopic compositions of peridotites along the Oblique Segment is shown in Figure 10.

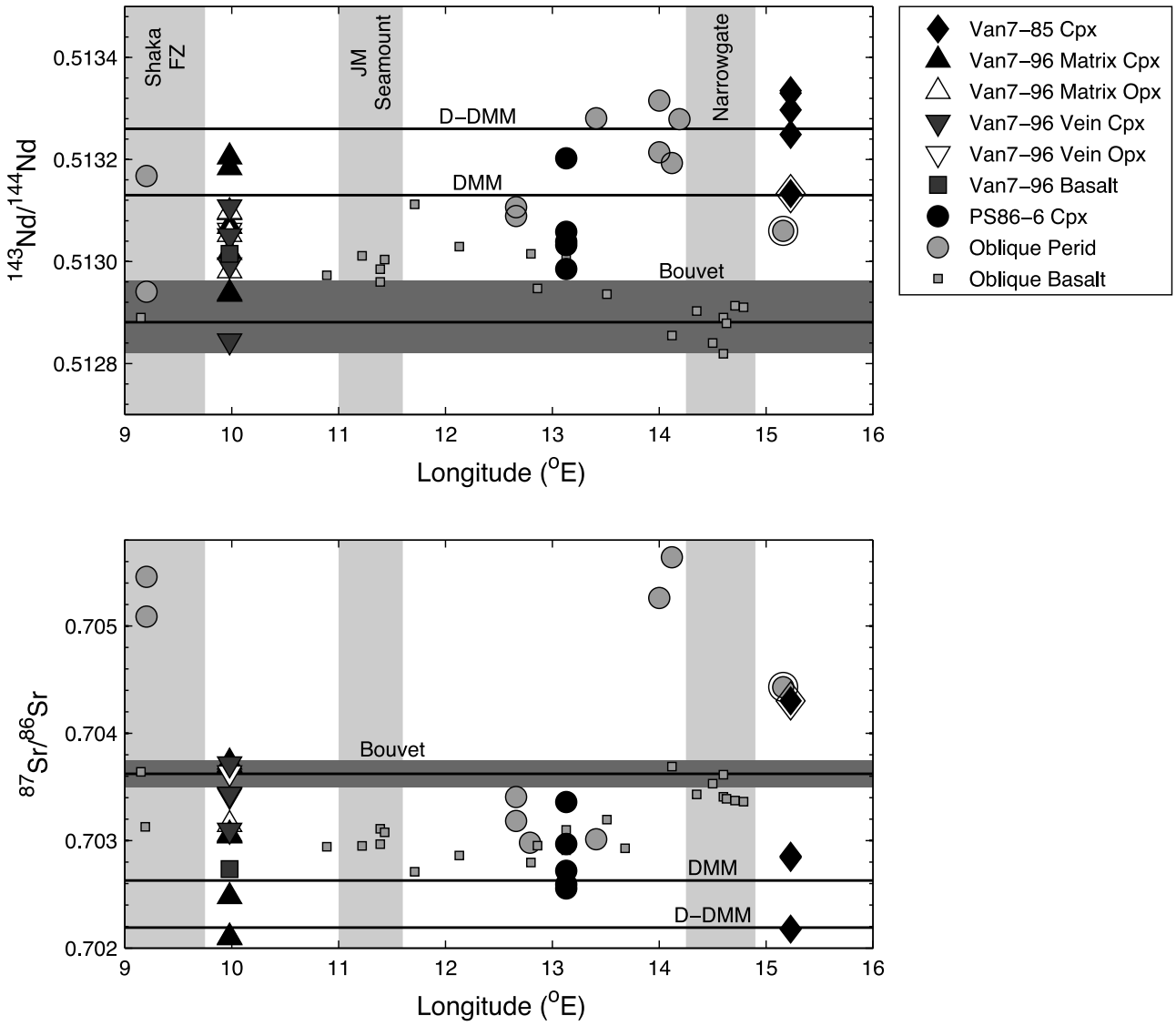

Figure 10. Variation of Nd and Sr isotopes along the SWIR Oblique Segment. Joseph Mayes Seamount and Narrowgate are regions where spreading is approximately orthogonal, volcanic activity occurs and significant basaltic crust is present. These features are largely absent along the rest of the Oblique Segment. The two outlined samples around 15.2°E are the most altered samples in this study. Data for other peridotite Cpx and basalts are from references in Figure 5; the Shaka Fracture Zone peridotites are whole rock analyses of fresh mylonitized peridotites.

Peridotite Cpx from dredge PS86-6 (near 13°E) range from $^{143}Nd/^{144}Nd$ of 0.513202 (more depleted than DMM) to 0.512985 (similar to Bouvet basalts), as reported by *Salters and Dick* [2002]. This dredge contains no veins, though the relatively enriched Cpx trace element concentrations (Figure 4) and high modal Cpx contents (Table 2) suggest that these peridotites have undergone some form of metasomatism. In contrast, dredge 85 peridotite Cpx (near 13°E) are depleted in terms of isotopes, Cpx modes and trace element concentrations.

[77] Previous studies of SWIR basalts have identified Bouvet as the source of isotopic heterogeneities for regions to both the east and west of the Shaka Fracture Zone. For example, the influence of the hot spot is observed in basalts from the Shaka (located at 9°E) westward along the ridge to the present-day location of the plume near Speiss Ridge at 0° [*le Roex et al.*, 1983; *Kurz et al.*, 1998]. In basalts from the Oblique Segment and the adjacent Orthogonal segment, which extends to 25°E, Bouvet has been identified as the source of isotopic, trace and major element variations [*le Roex et al.*, 1992; *Standish*, 2006; *Standish et al.*, 2008]. The Nd and Sr isotopic composition of Oblique Segment basalts form a trend between DMM and Bouvet, as shown in Figure 5. However, basalt isotopic compositions do not vary systematically with distance from the Bouvet Hotspot track. As shown in Figure 10, basalts from the Narrowgate region (far to the east of the hot spot track, at 14.5°E), have the greatest overlap with the Bouvet isotopic range [*Standish*, 2006]. In contrast, a sample just to the east of Joseph Mayes Seamount (11.7°E) has Sr and Nd isotopic compositions similar to DMM.

[78] In the model proposed by *le Roex et al.* [1992], *Salters and Dick* [2002] and *Standish et al.* [2008], the isotopic signatures in basalts along the SWIR Oblique Segment are due to pervasive infiltration of the mantle by melts from the Bouvet plume, which resulted in crystallization of pyroxenites at depth in the asthenosphere. During upwelling beneath the ridge axis, the pyroxenite component preferentially melted, as pyroxenite has a lower melting point than peridotite [*Hirschmann and Stolper*, 1996].

[79] Alternatively, the variability in basalt and peridotite compositions is derived from preexisting heterogeneities in the mantle. In this interpretation, Bouvet only influenced the immediate mantle around the plume (e.g., it affected dredge 96, which sits adjacent to the hot spot track, but not peridotites further to the east on the Oblique Segment). Isotopically, the Bouvet signature is not extremely enriched and thus not entirely distinctive as a plume signature. While the mantle is typically treated as a single composition, represented by DMM, the global variability of MORB compositions [*Lehnert et al.*, 2000; *Su and Langmuir*, 2003] indicates that the mantle is compositionally variable. The forms that heterogeneities take in the upper mantle are not well defined: they could be veins or they could be variably enriched and depleted peridotite, or a combination of both. The isotopically enriched component in the mantle can be relatively minor, but as isotopic enrichment is associated with trace element enrichment, it would dominate the composition of a mixed melt. In addition, production of basalts with a range of compositions is controlled both by source composition and the degree to which melt interacts with the mantle and other melts during extraction.

[80] Analysis of the Atlantis II Fracture Zone peridotites provides additional constraints on the variability in source mantle composition. The Atlantis II Fracture Zone is not associated with any hot spot track, but some basalts are isotopically enriched. This enrichment is matched by Nd isotopic enrichment in peridotite RC27-9-6-2. This peridotite is veined, but the clinopyroxenite vein is a cumulate feature with more depleted isotopic and trace element compositions than the host peridotite. Figure 11 compares the isotopic enrichments along and across the fracture zone. The basalt isotopic enrichment does not occur specifically on one side of the fracture zone or at only one location along the fracture zone. A transform volcano, located adjacent to the sampling location of peridotite RC27-9-6-2 (Figure 1), ranges in composition from DMM ($^{143}Nd/^{144}Nd = 0.51313$) to an enriched composition ($^{143}Nd/^{144}Nd = 0.51298$). RC27-9-6-2 ranges from an enriched composition in the peridotite matrix ($^{143}Nd/^{144}Nd = 0.512915$) to a near-DMM composition in the clinopyroxenite vein ($^{143}Nd/^{144}Nd = 0.513099$). Hence, in one peridotite sample we observe the entire isotopic range of basalts from the transform volcano. The randomly distributed isotopic enrichment of the Atlantis II Fracture Zone suggests that isotopic heterogeneities in the mantle are ubiquitous and exist on a subkilometer scale.

[81] The range of isotopic compositions observed in basalts from both the Oblique Segment and the Atlantis II Fracture Zone are also observed in spatially associated peridotites. Figure 12 demonstrates this observation with histograms of $^{143}Nd/^{144}Nd$ for basalts and peridotites from the Oblique Segment, the Atlantis II Fracture Zone, and the global ridge system. The overlap between basalts and peridotites is valid even if the veined peridotites from dredge 96 are excluded. While Oblique Segment dredges 85 and 86 have depleted isotopic compositions, dredge PS86-6 peridotites extend to both depleted and enriched isotopic compositions.

[82] In Figure 12c, we compare the global data sets for peridotites and basalts. The MORB data set consists of 1075 samples from all ridges. In contrast, the abyssal peridotite data set consists of isotopic data on Cpx mineral separates for 70 peridotites from three main areas: the Vema Fracture Zone on the MAR, the Atlantis II Fracture Zone on the SWIR and the SWIR Oblique Segment. While this data set is not truly global, all three areas have similar compositional ranges despite their different locations and different proximities to hot spots. The similarity of the distribution of the 70 peridotite analyses to the MORB data set suggests that these peridotites are representative of the isotopic range of the oceanic upper mantle.

[83] *Salters and Dick* [2002] emphasized that abyssal peridotites have statistically more depleted Nd isotopic compositions than MORB and advocated for a bimodal mantle composed of peridotite and pyroxenites. However, from the additional data presented in this study, we find that peridotites have a similar isotopic range to that of MORB (Figure 12) and we do not find unambiguous evidence for a pervasive pyroxenite component everywhere in the oceanic upper mantle. Given the continuous gradation in residual peridotites and basalts from depleted to enriched isotopic compositions, a bimodal mantle composition is not required by our data. It is more likely that the mantle has been metasomatized to various degrees, creating heterogeneous mantle with variable scales of enrichment, both in space and amplitude. For the western SWIR in proximity to the Bouvet Hotspot track, the nature of the metasomatic enrichment is likely directly related to Bouvet and similar to what we report for dredge 96, consisting of a more fertile and isotopically enriched mantle region rich in veins.

[84] Conversely, the finding of abyssal peridotites more depleted than any MORB (Figure 12c) argues for mantle that extends to more depleted compositions than previously estimated. For peridotites to ingrow depleted isotopic compositions (e.g., dredge 85), they must have been chemically depleted prior to entering the mid-ocean ridge melting regime. Hence, the contribution of isotopically depleted peridotites to the trace element concentrations in basalts is small compared to the contribution from more enriched peridotites. For this reason, peridotites should always extend to more depleted isotopic compositions than basalts, but this observation does not imply that basalts have formed from a different source than that represented by abyssal peridotites.

[85] A straightforward calculation demonstrates the effect of mixing melts from variably depleted mantle. Starting with the composition of bulk silicate Earth (BSE), assume that one region of mantle undergoes 0.01% modal fractional melting at 2 Ga, whereas another region undergoes 5% melting at 2 Ga. The composition of these materials today will be $\epsilon_{Nd} = +0.5$ with a Nd concentration of 1.2 ppm for the 0.01% melted mantle, versus $\epsilon_{Nd} = +95$ and 0.3 ppm Nd for the 5% melted mantle. Now, assuming these portions of mantle have mixed together, allow them to undergo 3% fractional melting at the ridge axis today. If equal volumes of melt from the two sources are mixed to form basalt, the resulting mixture will

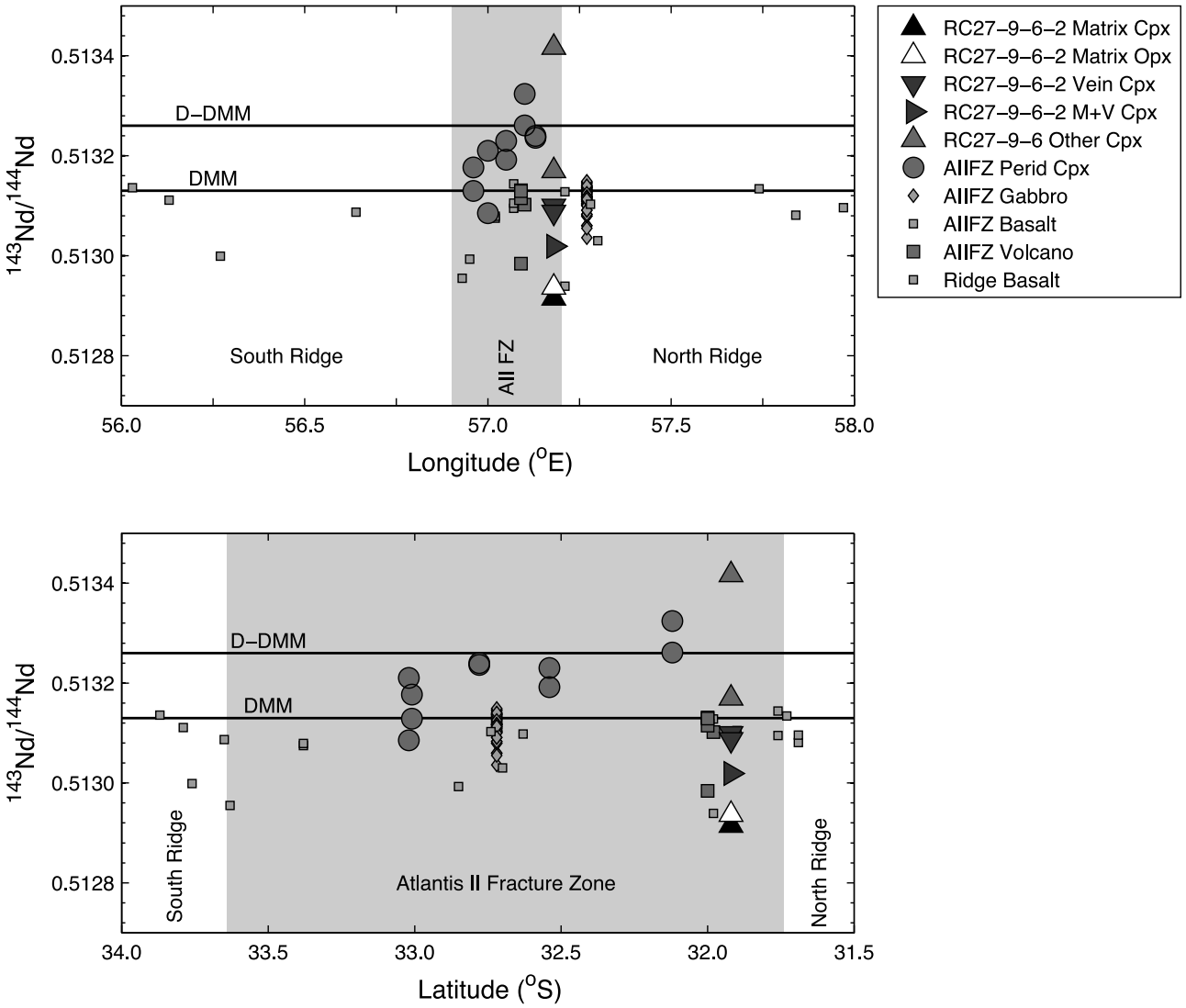

Figure 11. Variation of Nd across and along the Atlantis II Fracture Zone. No systematic variation is observed in either direction. Data for other peridotite Cpx (including additional data for dredge RC27-9-6), gabbros, and basalts are from references in Figure 5 and additional $^{143}Nd/^{144}Nd$ basalt data from *Coogan et al.* [2004].

have ϵ_{Nd} = +9.6 and 14 ppm Nd. This is the isotopic composition of DMM with a Nd concentration typical of MORB. While this calculation is clearly nonunique, it demonstrates how a melt from a mantle source that has previously undergone significant depletion can be hidden in MORB.

[86] Finally, we find noteworthy the observation that almost the entire spectrum of isotopic variation can be observed in individual dredges (e.g., Van7-96 and PS86-6 from the Oblique Segment and RC27-9-6 from the Atlantis II Fracture Zone), demonstrating that large amplitude mantle heterogeneity in a single ultramafic lithology can occur on length scales of <1 km. This indicates that the observation of large variations in a dredge from the MAR by *Cipriani et al.* [2004] is a general characteristic of some (but not all) abyssal peridotite dredges. We suggest that melting, melt-rock reaction, and melt crystallization (recent and old) are responsible for creating mineralogical, chemical and isotopic heterogeneities and for refertilizing originally depleted asthenospheric peridotites. In the following sections, we explore the general implications of this for the composition of the oceanic upper mantle.

5.5. Preexisting Mantle Heterogeneity Versus Recent Ridge-Derived Heterogeneity

[87] Based on the preceding discussion, we observe that abyssal peridotites are more complex than would be expected for the products of simple melt extraction from a uniform upper mantle at present-day ridges. Instead, we suggest that the isotopic and compositional variations in peridotites reflect a combination of recent ridge processes and preexisting heterogeneities. Previous studies of peridotites have also suggested that the mantle at some ridge localities has undergone earlier depletion and enrichment events [e.g., *Seyler et al.*, 2003; *Cipriani et al.*, 2004; *Liu et al.*, 2008]. In order to access the extent to which oceanic upper mantle compositions reflect long-term heterogeneity versus recent melting systematics, we have compiled all available trace element,

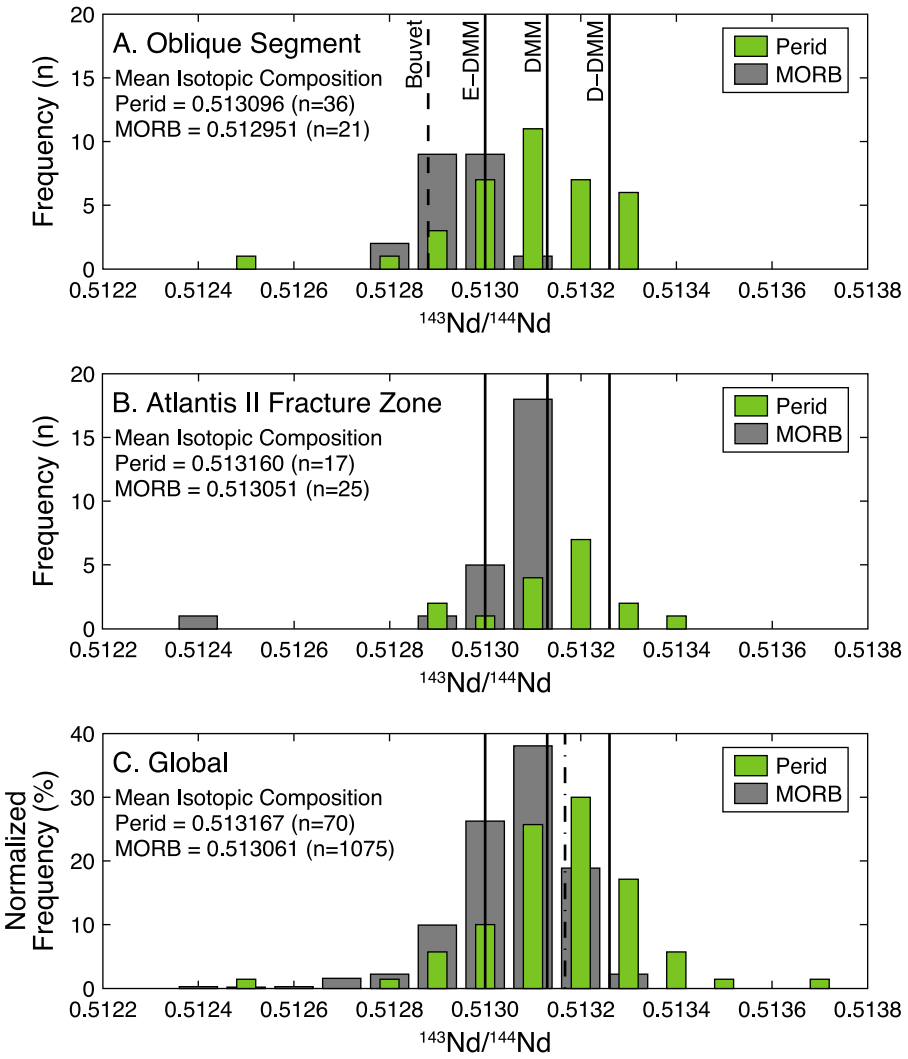

Figure 12. Histograms of peridotite and basalt Nd isotopic ratios for (a) the Oblique Segment, (b) the Atlantis II Fracture Zone, and (c) global abyssal peridotite and MORB. DMM and the 2σ variation in DMM (D-DMM and E-DMM) are shown by solid lines and global average peridotite composition by the dashed-dotted line. Note that Oblique Segment basalts and peridotites are shifted to lower average $^{143}Nd/^{144}Nd$ due to the influence of Bouvet Hotspot (dashed line). Data are from this study and references in Figure 5. Peridotite data in Figure 12c also includes data from *Kempton and Stephens* [1997] and *Cipriani et al.* [2004]; global MORB is a compilation from PetDB (http://www.petdb.org) [*Lehnert et al.*, 2000].

modal and major element data for peridotites with measured Cpx isotopic compositions. If peridotites were not significantly modified by recent ridge processes, then their isotopic compositions should correlate with parameters of depletion such as modal Cpx, Ce/Yb and spinel Cr # (i.e., isotopic depletion or enrichment should be accompanied by long-term compositional depletion or enrichment). In Figure 13, plots of $^{143}Nd/^{144}Nd$ against these depletion parameters demonstrate that no correlation exists. Long-term heterogeneity is required to explain isotopic variability, but peridotite compositions have essentially all been affected by recent melting.

[88] The lack of a correlation between isotopes and peridotite compositions indicate the complexity of the effects of melting and melt-rock reaction. For example, simple isotopic exchange could occur when melt and pyroxenes are in chemical equilibrium and dissolution or precipitation of Cpx is inhibited. In such a case, the isotopic composition of the peridotite would be modified without modal and chemical changes. Alternatively, exchange dissolution or exchange precipitation can occur, whereby isotopic and chemical enrichments are accompanied by modal decrease (exchange dissolution) or increase (exchange precipitation) in Cpx. Finally, during melting, the isotopic composition of the peridotite does not vary, while the chemical composition does. Figure 13 illustrates these possible scenarios for the covariation of the isotopic and chemical compositions of peridotites and compares them to the abyssal peridotite Cpx data set.

[89] Dredge 96 peridotites indicate that past plume-ridge interactions resulted in significant modification of the depleted upper mantle through veining and metasomatism. On the plot of $^{143}Nd/^{144}Nd$ against modal Cpx (Figure 13a), dredge 96 samples are scattered, whereas on a plot of

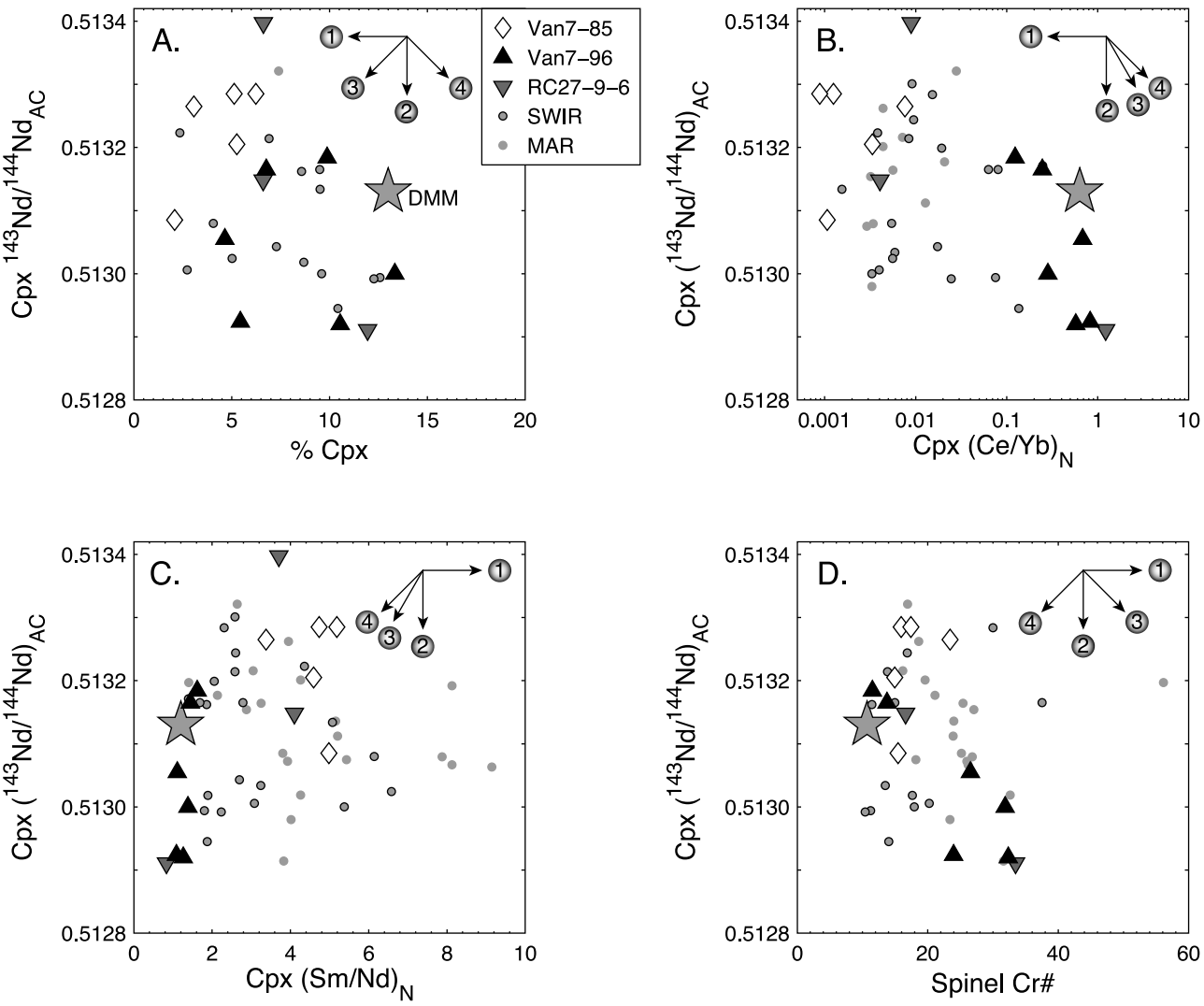

Figure 13. The variation of abyssal peridotite Cpx ^{143}Nd/^{144}Nd as a function of modal Cpx, Ce/Yb, Sm/Nd, and spinel Cr #. ^{143}Nd/^{144}Nd values are age corrected to the 1200°C isotherm, as discussed in the text; Cr # is calculated as Cr/(Cr + Al) × 100; the N subscript for REE ratios indicates normalization to PUM [*McDonough and Sun*, 1995]. During melting, modal Cpx and Ce/Yb decrease with increasing degree of melting, whereas spinel Cr # and Sm/Nd increase with increasing degree of melting. Arrows in the top corners of the plots indicate the direction of change for different processes: (1) melting, (2) isotope exchange with an enriched source, (3) exchange dissolution, and (4) exchange precipitation. Data for other SWIR Cpx are from this study and references in Figure 5; data for MAR Cpx are from *Cipriani et al.* [2004] and *Brunelli et al.* [2006]; values for DMM are from *Su and Langmuir* [2003] and *Workman and Hart* [2005].

^{143}Nd/^{144}Nd against Ce/Yb they have a negative correlation (Figure 13b). We suggest that this indicates both exchange dissolution and precipitation with an enriched (Bouvet derived) melt. In particular, sample Van7-96-38, with the most depleted Nd isotopic composition, is a likely starting material for the melt-rock reaction process, consistent with the previous discussion based on Cpx-Opx isotopic disequilibrium.

[90] Compared to dredge 96 samples, dredge 85 samples possess more depleted Nd isotopic compositions and are more depleted in modal Cpx (Figure 13a) and Ce/Yb ratios (Figure 13b). This suggests that there exists a link between long-term chemical depletion and present-day mineralogy and mineral chemistry. However, the overall scatter in Figure 13 illustrates the difficulty in separating the effects of melt extraction, including melt-rock reaction, from the preexisting compositional heterogeneity present in abyssal peridotites.

[91] Samples from the Atlantis II Fracture Zone show a large range of Nd isotopic compositions. The most isotopically enriched sample is also enriched in modal Cpx (Figure 13a) as well as Ce/Yb (Figure 13b). This sample (RC27-9-6-2) lies off the general Cpx depletion trend for abyssal peridotites. This suggests that it underwent modification through melt-rock reaction and precipitation, instead of simply being a more fertile peridotite composition. As noted earlier, there is ample evidence for reaction between peridotite and enriched melt at this site. Two depleted samples from the same dredge indicate heterogeneity in the premelting depleted mantle Nd isotopic composition (e.g., Figure 11). However, despite large differences in the Nd

isotopic composition of these samples, the degrees of depletion in terms of Cpx mode and Ce/Yb are similar.

[92] Overall, the variation of spinel Cr # in peridotites is the only compositional parameter that suggests any correlation with Cpx Nd isotopic composition (Figure 13d). In addition to our SWIR data, we plot the data from the MAR Vema Lithospheric Section [*Cipriani et al.*, 2004; *Brunelli et al.*, 2006]. *Cipriani et al.* [2004] noted that $^{143}Nd/^{144}Nd$ has a negative correlation with spinel Cr # for the Vema peridotites, but no corresponding correlation with Cpx trace element concentrations. In Figure 13d, an overall (weak) negative correlation exists between these two parameters for all peridotites. As suggested by *Cipriani et al.* [2004], we interpret the increase in Cr # with decreasing $^{143}Nd/^{144}Nd$ to indicate interaction between depleted peridotite and a migrating enriched melt.

[93] As recent interaction with enriched melt significantly modifies the original depleted Nd isotopic signature of abyssal peridotites, we suggest that similar processes in the geologic past could have generated enriched signatures in the upper mantle and that these peridotites were later entrained in the upwelling mantle beneath an ocean ridge. Based on the histograms in Figure 12, we favor a model for the upper mantle which is heterogeneous at a variety of length scales, due to repeated enrichment and depletion events. In addition, we find significant the observation that depleted peridotites from a single dredge (dredge 85) have no evidence for reaction with enriched melt, but display significant Nd isotopic heterogeneity. We conclude that various extents of chemical depletion on length scales of <1 km have existed for a sufficiently long period of time to produce isotopic heterogeneity.

[94] The above discussion indicates that peridotite compositions reflect both recent ridge melting processes and preexisting heterogeneities. The distinction between long-term depletion and recent depletion due to melt extraction cannot be made easily on the basis of mineralogy, trace elements or major elements. Only isotopes provide a clear indication of preexisting heterogeneities in the mantle. Below, to understand the long-term evolution of mantle composition, we compare the abyssal peridotite data set to standard isotope evolution models for the mantle.

5.6. Long-Term Evolution of Mantle Composition

[95] Results from the present study, combined with the data of *Salters and Dick* [2002] and *Cipriani et al.* [2004], suggest that the asthenospheric mantle (DMM) is more isotopically heterogeneous and extends to more depleted isotopic compositions than previously considered [e.g., *Su and Langmuir*, 2003; *Workman and Hart*, 2005]. The histograms in Figure 12 demonstrate the isotopic range of peridotites, which is comparable to MORBs and extends significantly beyond the estimates of D-DMM and E-DMM of *Workman and Hart* [2005].

[96] The most depleted SWIR peridotites are more depleted than D-DMM, with $^{87}Sr/^{86}Sr$ as low as 0.702096 and $^{143}Nd/^{144}Nd$ up to 0.513417, requiring long-term depletion of Rb relative to Sr and Nd relative to Sm. Such long-term LREE depletion suggests that there exists, in the asthenospheric mantle, more strongly LREE-depleted regions than suggested by MORBs. As discussed above, these concentration variations are not apparent in surveys of MORB compositions. Aggregated melts form by mixing of melt fractions derived from variously depleted source peridotites, resulting in a Nd mass balance that is dominated by the least depleted end-member. Hence, MORBs are skewed toward more isotopically enriched compositions than peridotites (Figure 12).

[97] The presence of ultradepleted mantle as observed here requires a reassessment of current models for mantle depletion. To demonstrate the degree to which current isotope models to not replicate the abyssal peridotite data set, we explore the continuous depletion model used by *Workman and Hart* [2005] to model DMM. This model is representative of standard isotope evolution models for the Earth [e.g., *Allégre*, 1968; *DePaolo and Wasserburg*, 1976; *Hofmann*, 1997] that assume depletion occurs either at a specific time (two-stage evolution model), repeatedly (multistage evolution model) or continuously from the initial depletion time (continuous depletion model). Our purpose in using a model of this type is not to replicate the abyssal peridotite data set by adjusting model parameters. Instead, our goal is to demonstrate the degree to which current models are unable to explain the complexity observed in abyssal peridotite isotope compositions and to explore the implications of this in terms of mantle processes.

[98] The continuous depletion model predicts the present-day parent-daughter ratios of DMM based on (1) the isotopic ratios of DMM and BSE and (2) continuous depletion of the parent-daughter ratio of BSE from the initial depletion time, t. In this model, continuous removal of crust from the chondritic mantle begins at t, in contrast to a two-stage model where all depletion occurs at t. Workman and Hart estimate t to be 3 Ga, as a best estimate for the start of significant continental crustal growth [*Taylor and McLennan*, 1995]. The evolution of the isotopic composition of DMM is calculated from the composition of BSE and the transport coefficient, k:

$$\left(\frac{^{143}Nd}{^{144}Nd}\right)^{0}_{DMM} = \left(\frac{^{143}Nd}{^{144}Nd}\right)^{t}_{BSE} + \frac{\lambda\left(\frac{^{147}Sm}{^{144}Nd}\right)^{t}_{BSE}\left[1 - e^{-(\lambda+k)t}\right]}{\lambda + k} \quad (7)$$

The superscript 0 indicates present-day values, whereas the superscript t indicates values at time t. The transport coefficient is equivalent to an additional decay constant in the decay equation and is calculated from the parent-daughter ratios of BSE and DMM:

$$\frac{\left(\frac{^{147}Sm}{^{144}Nd}\right)^{0}_{DMM}}{\left(\frac{^{147}Sm}{^{144}Nd}\right)^{t}_{BSE}} = e^{-(\lambda+k)t} \quad (8)$$

[99] From equation (7), we can determine k for a given t and $^{143}Nd/^{144}Nd$ composition of the mantle. For example, taking the $^{143}Nd/^{144}Nd$ composition of DMM = 0.51313 [*Workman and Hart*, 2005] and t = 3 Ga, we calculate $k = -7.8 \times 10^{-11}$. The present-day composition of $^{147}Sm/^{144}Nd$ is then calculated from equation (8); for DMM, *Workman and Hart* [2005] found that $^{147}Sm/^{144}Nd = 0.249$.

[100] In Figure 14a we plot isotopic growth curves for different t to demonstrate the effect of initial depletion time on $^{147}Sm/^{144}Nd$. Also in Figure 14a, we plot abyssal peridotite data, using age-corrected Cpx $^{143}Nd/^{144}Nd$ and $^{147}Sm/^{144}Nd$

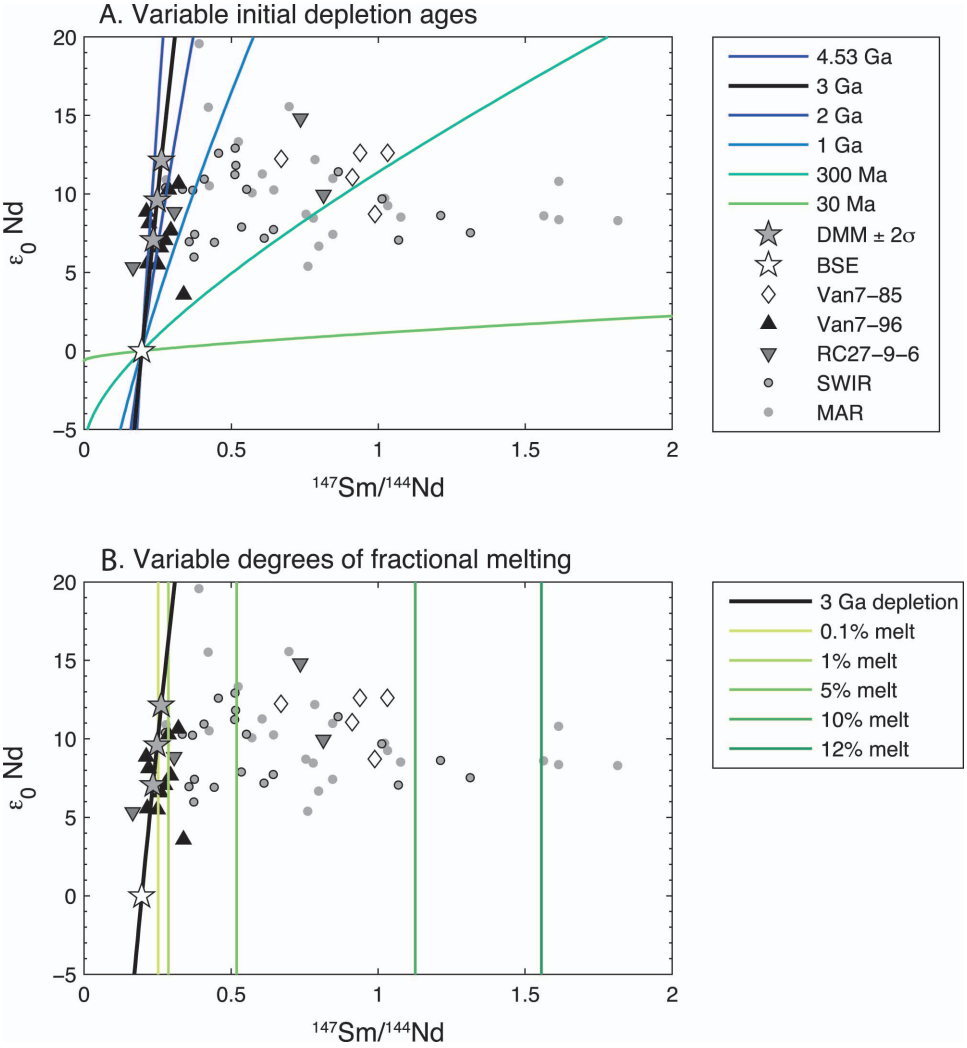

Figure 14. (a) The continuous depletion model for the variation of ϵ_0 Nd as a function of $^{147}Sm/^{144}Nd$, for different initial depletion times. The preferred model of *Workman and Hart* [2005] is for depletion to begin at 3 Ga (thick black line) and their estimates of DMM, D-DMM, and E-DMM lie on this line. Abyssal peridotite Cpx data, from this study and the literature (see Figure 13 for references), extend over a larger range of Sm/Nd compositions than predicted by the continuous depletion model for realistic initial depletion times (e.g., $\geq$3 Ga). (b) The predicted variation of $^{147}Sm/^{144}Nd$ during modal fractional melting of DMM that has evolved following the 3 Ga continuous depletion model. The spread in Cpx $^{147}Sm/^{144}Nd$ can be explained by variable degrees of melting from an initial DMM composition, but the large variations in $^{147}Sm/^{144}Nd$, especially within individual dredges (e.g., dredge 85), cannot be explained by variable degrees of melting.

ratios and assuming that these are representative of the whole rock. Initial depletion ages of $\geq$3 Ga are reasonable based on our knowledge of early Earth evolution [e.g., *Taylor and McLennan*, 1995]. In addition, the difference between 3 Ga or an earlier initial depletion age is small. Hence, compared to reasonable estimates for initial depletion ages, the abyssal peridotite data are observed to trend toward higher Sm/Nd ratios than predicted by the continuous depletion model.

[101] One way to understand the comparison of the abyssal peridotite data set to the continuous depletion model is to look at the role of k (the transport coefficient) in the model. As k is a combined transport coefficient for Sm and Nd [*Hart and Brooks*, 1970], the variability of k must be examined in terms of the geochemical behavior of Sm and Nd during mantle depletion. Following *Hart and Brooks* [1970], mantle depletion with respect to Nd can be written as

$$Nd^0_{DMM} = Nd^t_{BSE} e^{-\alpha t} \quad (9)$$

where Nd^0_{DMM} is the number of Nd atoms in DMM today, Nd^t_{BSE} is BSE at time t and α is the transport coefficient for Nd. Using Nd^t_{BSE} of 1.25 ppm (PUM) [*McDonough and Sun*, 1995], Nd^0_{DMM} of 0.581 ppm [*Workman and Hart*, 2005] and t of 3 Ga, we calculate $\alpha = 2.55 \times 10^{-10}$. The transport coef-

ficient for Sm, γ, is calculated from the relationship [*Hart and Brooks*, 1970]

$$k = \gamma - \alpha \quad (10)$$

Using the value derived above for k for DMM, -7.8×10^{-11}, we calculate $\gamma = 1.77 \times 10^{-10}$.

[102] The higher transport rate for Nd compared to Sm agrees with the greater incompatibility of Nd with respect to Sm during melting. The Sm/Nd ratio of bulk partition coefficients (Nd = 0.031; Sm = 0.045) [*Workman and Hart*, 2005] is 1.45, but the inverse ratio of 0.69 (the ratio of compatibilities in melt) is the relevant parameter to compare to the α/γ ratio, which is also 0.69. Hence, the transport coefficients reflect the mantle-crust transport of Nd and Sm via melting and melt extraction. This analysis demonstrates that the parameter k should always reflect the relative compatibility of the parent and daughter elements. Therefore, k can only be varied in the continuous depletion model such that the α/γ ratio is similar to the Sm/Nd melt/rock partitioning ratio. While a young t and large negative k would best fit the abyssal peridotite data (Figure 14a), this would require very rapid, recent depletion of the mantle with huge volumes of crust extracted. Thus, our knowledge of the differentiation history of the mantle and the geochemical behavior of Sm and Nd are best fit when t is $\geq$3 Ga and k is $\sim -7.8 \times 10^{-11}$.

[103] One potential explanation for the divergence of the peridotite data from the 3 Ga model for DMM evolution is the effect of recent partial melting on peridotite Cpx Sm/Nd ratios. In Figure 14b, we contour the plot of $^{147}Sm/^{144}Nd$ against $^{143}Nd/^{144}Nd$ for different degrees of modal fractional melting from an initial DMM Sm/Nd ratio of 0.411 [*Workman and Hart*, 2005]. For consistency with *Workman and Hart* [2005], we use modal melting instead of nonmodal melting. This simple melting model can be taken as an explanation for the variation in Sm/Nd among and within peridotite dredges, especially if more sophisticated melt focusing [e.g., *Cannat et al.*, 2008] and residual porosity [e.g., *Brunelli et al.*, 2006] models are used. However, variations in degree of melting and melt entrapment cannot explain the large isotopic range of the peridotites and, in particular, the variation within individual dredges (e.g., ε_0 Nd in dredge 85 varies from +8.7 to +12.6). Hence, the Sm/Nd ratios of peridotites must partly reflect melt extraction event(s) that significantly predate recent melting at the ridge.

[104] In Figure 15a, we attempt to explain the divergence of observed peridotite compositions from the continuous depletion model by adding removal of material at different times to the model and calculating the present-day ratio of this material. In this scenario, the $^{143}Nd/^{144}Nd$ ratio evolves to compositions that lie between present-day BSE and DMM, thus explaining enriched mantle components (i.e., recycled slabs) but not the more depleted components in the mantle. As demonstrated in Figure 15a, our model is limited in that it cannot produce compositions outside of the BSE-DMM range. Abyssal peridotites extend to higher Sm/Nd ratios, but to evolve to these extremely depleted isotopic compositions, the model would need to explicitly calculate changes in Sm/Nd ratios during melting.

[105] To further explore the implications of the abyssal peridotite isotope data set for mantle composition, we have calculated the $^{147}Sm/^{144}Nd$ ratios predicted by the continuous depletion model based on measured $^{143}Nd/^{144}Nd$ ratios. The implication of this calculation is that the difference between the calculated Sm/Nd ratio and the measured ratio is due to recent melting. To demonstrate this calculation, in Figure 15b we plot the ϵ_0 Nd compositions of the peridotites against their measured $^{147}Sm/^{144}Nd$ ratios and compare this to the 3 Ga continuous depletion model. We then use the 3 Ga model in Figure 15c to calculate the $^{147}Sm/^{144}Nd$ ratio necessary to produce the observed $^{143}Nd/^{144}Nd$ ratios of the samples. Finally, in Figure 15d, we plot modeled versus measured $^{147}Sm/^{144}Nd$ ratios and contour for degree of recent melting necessary to produce the measured ratios from the predicted ratios. As in the previous calculation for degree of melting, this calculation can explain the large measured Sm/Nd concentration range among peridotites. However, it still does not satisfactorily explain the spread in isotopic composition (represented by the modeled $^{147}Sm/^{144}Nd$ in Figure 15d) of the peridotites, especially within dredges. The peridotite isotopic range still requires ancient episodes of melt extraction and recycling of enriched material.

[106] Our results indicate that evolution of the asthenosphere is more complicated than implied by depletion models constrained by BSE and DMM alone. The continuous depletion model results in calculated Sm/Nd ratios that are too low to reconcile with measured values. Traditionally, this has been interpreted as indicating that melt extraction at the ridge axis produced the mismatch. However, the isotopic heterogeneity among peridotites suggests that heterogeneity with respect to Sm/Nd was preexisting and down to length scales <1 km for a considerable length of time. For example, the depleted peridotites from dredge 85 can be explained by an ancient, low-degree, melt extraction event (e.g., around 0.5–1 Ga) that produced isotopic heterogeneity, followed by recent melting and melt-rock reaction to produce present-day Sm/Nd ratios. We have suggested above that peridotites are mixtures of multiple depletion events and variable recent melt extraction. Abyssal peridotites indicate that models need to explicitly include ancient melting events if they are going to reproduce the observed variations in mantle composition.

6. Conclusions

[107] This study uses detailed isotope and trace element analyses of peridotites from individual dredges to constrain the spatial scale and amplitude of heterogeneities in the mantle. Isotopic heterogeneity was observed both among samples from the same dredge and within samples themselves. On the basis of our data, we reach several conclusions:

[108] 1. The amount of radiogenic ingrowth following melt extraction is negligible compared to the observed range of peridotite isotopic compositions. In general, peridotites spend $\sim$1–20 My from the time that they pass through their closure temperature to the time that they are collected at variable distances from the ridge axis. Radiogenic ingrowth during this time results in <0.01% change among our samples, despite slow upwelling rates along the SWIR. Thus, the observed isotopic range of abyssal peridotites and the extremely depleted compositions among some peridotites reflect the composition of the asthenospheric mantle.

[109] 2. From our isotopic analyses of Cpx and Opx, combined with modal analyses, we have reconstructed peri-

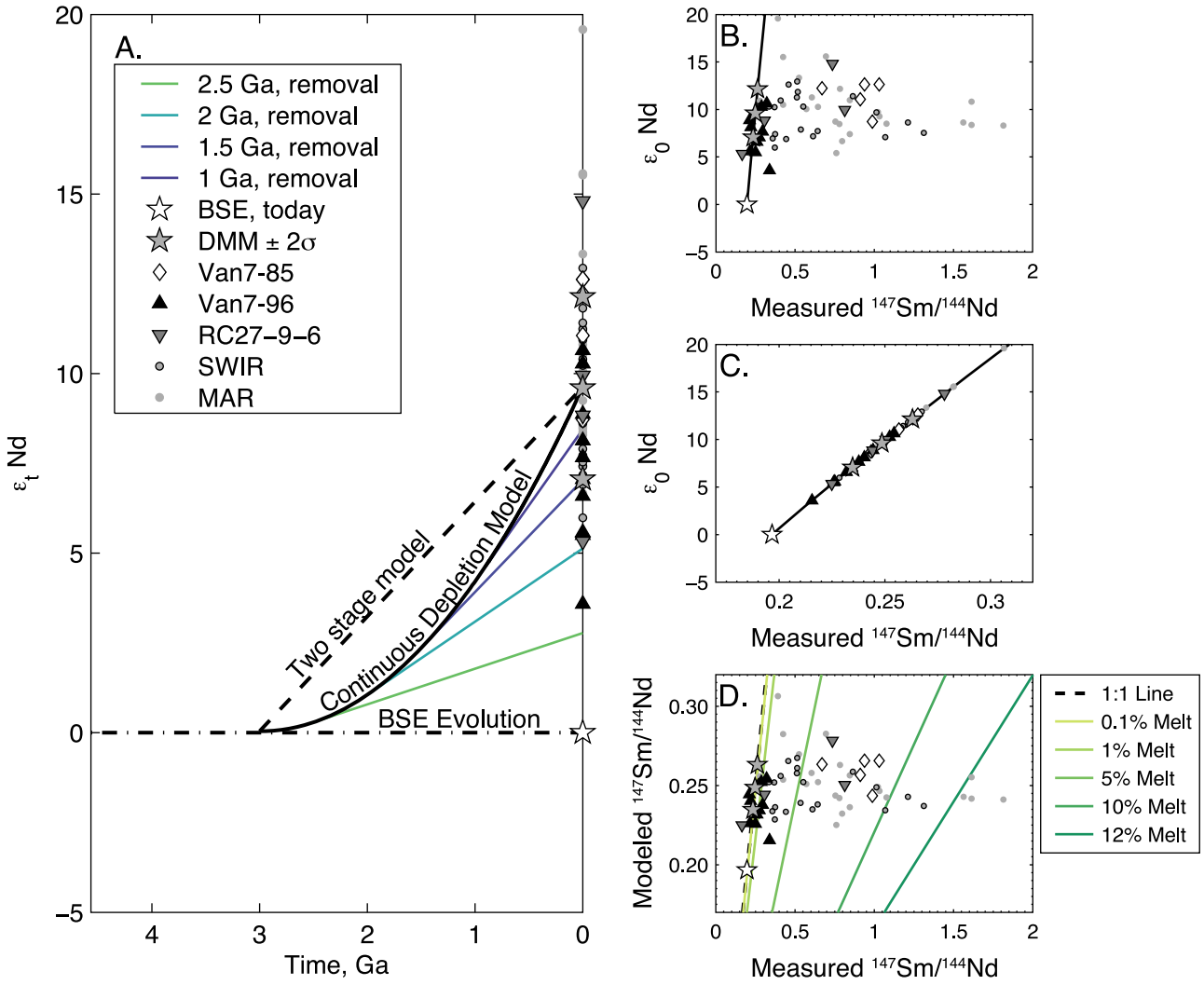

Figure 15. (a) Models of mantle Nd isotopic evolution through time. The thick solid line is a continuous depletion model with gradual depletion beginning at 3 Ga; the thick dashed line is a two-stage model with instantaneous depletion at 3 Ga. These models follow slightly different trajectories but are constrained to produce the same present-day $^{143}Nd/^{144}Nd$ DMM ratio. Lines coming off the continuous depletion model are for removal of material from the mantle at different times since 3 Ga, producing a range of present-day compositions between DMM and BSE. (b) Variation of ϵ_0 Nd for abyssal peridotite Cpx against measured $^{147}Sm/^{144}Nd$ ratios. The solid line is the evolution of ϵ_0 Nd for the continuous depletion model with depletion starting at 3 Ga. (c) Modeled $^{147}Sm/^{144}Nd$ ratios based on present-day peridotite Cpx $^{143}Nd/^{144}Nd$ ratios, the composition of BSE and the 3 Ga continuous depletion model (solid line). (d) Comparison of modeled and measured $^{147}Sm/^{144}Nd$ ratios, contoured for the degree fractional melting necessary to deplete the predicted Sm/Nd ratios to the measured ratios.

dotite whole rock compositions. In general, >85% of the trace element budget of peridotites is contained within Cpx. Hence, Cpx is a good proxy for peridotite bulk composition.

[110] 3. Peridotites do not display isochronous relationships among samples from the same dredge or for those grouped by location. This indicates that peridotite compositions have been modified by melting and melt-rock reaction at the present-day ridge axis. However, the large range in isotopic composition among peridotites from individual dredges indicates that the mantle must have been heterogeneous before melting began.

[111] 4. Pyroxenite veins from two localities on the SWIR are both interpreted as having formed by recent crystallization of melt in a conductively cooling mantle. Veins do not have the predicted compositions of recycled oceanic crust. For example, at the Atlantis II Fracture Zone, the clinopyroxenite vein in sample RC27-9-6-2 is more depleted than the host peridotite. In dredge 96 on the Oblique Segment, the major, trace and isotopic compositions of the pyroxenite veins overlap those of coexisting peridotites. We suggest that the variability among peridotites and basalts from this area is due to veining of the upper mantle by Bouvet Hotspot, though we cannot rule out an independent origin related to preexisting mantle heterogeneity. In either case, the isotopic composition of some dredge 96 samples require a recycled oceanic crust component, but the pyroxenites are not direct samples of recycled crust.

[112] 5. By combining our data set with existing data for abyssal peridotites, we find that peridotites cover the same isotopic range as MORBs, but also extend to more depleted compositions. No missing component is required to reconcile MORB isotopic compositions with peridotite compositions. A few of our samples are relatively enriched, with $^{143}Nd/^{144}Nd$ as low as 0.512884. In particular, peridotite RC27-9-6-2 provides evidence for enriched mantle unrelated to any hot spot. Peridotites, however, extend to more depleted compositions than basalts, with $^{87}Sr/^{86}Sr$ as low as 0.702096 and $^{143}Nd/^{144}Nd$ as high as 0.513335 among our samples. This depleted end-member in peridotites is not observed in basalts, as the mass balance of aggregated melts formed by melt fractions from variably depleted sources is dominated by the least depleted component.

[113] 6. The composition of abyssal peridotites reflects both ancient depletion and enrichment events, and variable recent melting, melt-rock reaction and melt crystallization. In particular, the $^{143}Nd/^{144}Nd$ compositions of peridotites requires long-term depletion, but the lack of a correlation with parameters of melt depletion indicate recent modification of peridotites at the ridge axis. The timing (or timings) of previous depletions is difficult to determine due to the lack of any isochronous relationships among abyssal peridotite minerals or recalculated whole rocks. The observed length scale of heterogeneities extends to relatively small scales, down to <1 km and even <0.1 m in some cases. We conclude that the asthenospheric mantle is isotopically heterogeneous and probably also heterogeneous in terms of major and trace elements and modal composition, in agreement with previous work on abyssal peridotites [*Brandon et al.*, 2000; *Seyler et al.*, 2003, 2004; *Cipriani et al.*, 2004; *Harvey et al.*, 2006; *Liu et al.*, 2008]. Hence, we caution against the prevailing assumption that the entire range of chemical variations observed among abyssal peridotites was generated by melt extraction beneath the current set of ocean ridges.

[114] 7. The isotopic and trace element compositions of peridotites cannot be reconciled with isotope evolution models that are based only on the composition of DMM and BSE, such as two-stage or continuous depletion models. In addition to recent melt extraction, the combination of high $^{143}Nd/^{144}Nd$ and high Sm/Nd requires previous melt extraction episodes that are not accounted for by these types of models. The complexities in peridotite compositions introduced by recent melting processes must also have created heterogeneous lithosphere in the past, which was eventually subducted back into the mantle. We propose that the upper mantle consists of variably depleted and enriched peridotites and that this requires more complex mantle evolution models to account for the observed variations in the isotopic, trace, major and modal compositions of peridotites.

Appendix A: Major Elements

[115] In Data Set S1 of the auxiliary material, mineral major element compositions are presented as both grain and sample averages for Cpx, Opx, olivine, spinel and plagioclase. Data for sample RC27-9-6-2 includes data from *Lee* [1997]. Major element compositions of all primary silicate phases were determined by electron microprobe, using a JEOL JXA-733 at the Massachusetts Institute of Technology. For olivine, spinel and plagioclase, a focused 1 μm beam was used and multiple points collected per grain. For pyroxenes, to average out the effects of exsolution, a 10 μm defocused beam was used and data were collected by line traverses on grain cores and rims.

[116] Figure A1 shows the variation of spinel Cr # with spinel Mg # and TiO_2 in spinel. During melting, spinel Cr # increases while Mg # decreases [*Dick and Bullen*, 1984]. TiO_2 concentrations greater than DMM ($\sim$0.2 wt%) are indicative of melt refertilization in peridotite. Dredge 85 peridotites have low TiO_2, reflecting melting and melt extraction only. In contrast, spinels in dredge 96 and RC27-9-6-2 suggest variable degrees of melting and fractional crystallization of melt in the peridotite. In addition, dredge 96 pyroxenite spinels often have plagioclase rims due to a later melt infiltration event, and are thus not necessarily representative of processes that occurred during pyroxenite formation.

[117] The variation of Mg # with Cr # and with Na_2O for individual Cpx grains is shown in Figure A2. Dredge 85 Cpx fall in the range typical for abyssal peridotites. Cpx in dredge 96 peridotites and pyroxenites extend to unusually low Cr # and Mg #. In addition, dredge 96 peridotite Cpx have high Na_2O, while pyroxenite Cpx have Na_2O concentrations similar to depleted abyssal peridotites. RC27-9-6-2 has high Cr_2O_3, as evidenced by the bright green color of Cpx in this sample (whereas dredge 96 Cpx have low Cr_2O_3 and are grey in color; Figure 2). Variations in Cpx compositions in RC27-9-6-2 do not correspond to lithology (clinopyroxenite vein versus peridotite matrix) or to distance from the clinopyroxenite vein.

Appendix B: Partition Coefficients

[118] In Table B1, we present the first set of Cpx-Opx partition coefficients measured for abyssal peridotites from bulk mineral analyses. In addition, we calculate an average set of Cpx-Opx partition coefficients, excluding outliers and veins. The dominant valence state of each element in pyroxene and their ionic radii [*Shannon*, 1976] in Cpx and Opx are also listed in Table B1. The ionic radii provide a measure of the relative compatibility of each element in Cpx and Opx and we use these radii to order the elements in the spider diagrams in Figure B1. In Cpx, trace elements vary between sixfold and eightfold coordination, depending on whether they occupy the M1 or M2 site, whereas elements in Opx are in sixfold coordination in both the M1 and M2 sites. Thus elements have the same ionic radii in Cpx and Opx if they occupy the M1 site in Cpx: for example, the relatively small cations Zr and Ti. Ordering elements in this way is more relevant to intermineral behavior than the commonly used element ordering from *Hofmann* [1988], which is based on the partitioning of elements into melt.

[119] The range of partition coefficients from *Witt-Eickschen and O'Neill* [2005] and from *Hellebrand et al.* [2005] are shown on the spider diagrams in Figure B1. The Witt-Eickschen and O'Neill data set consists of LA-ICP-MS analyses of mineral separates from peridotite xenoliths that equilibrated over a temperature range of 900–1250°C. Their results constrain the systematic change in partition coefficients as a combined function of temperature and composition, the main variables controlling partitioning. These two effects cannot be separated for pyroxenes with an immiscibility gap. Our results overlap the high-temperature end of the

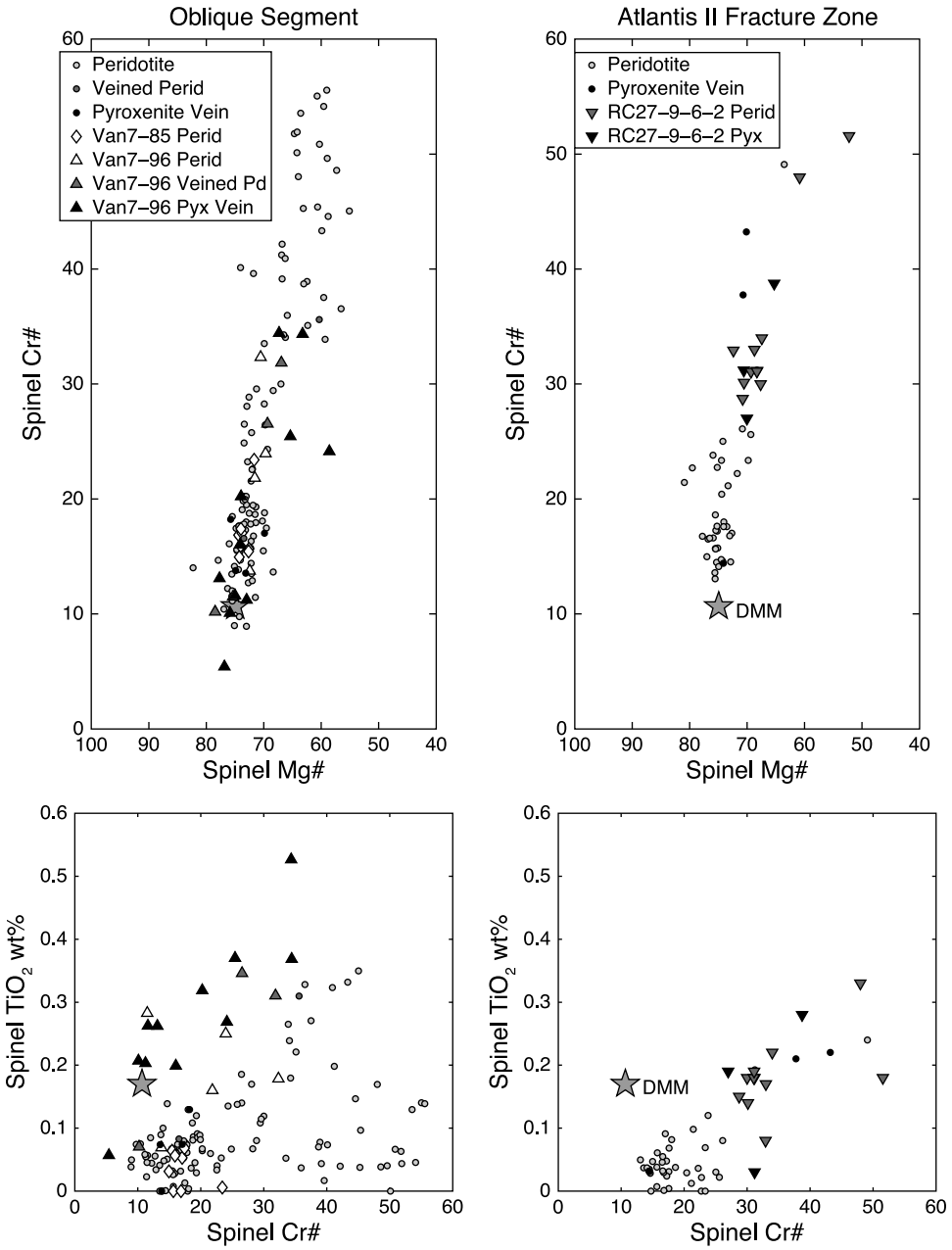

Figure A1. Variations in spinel Cr #, Mg #, and TiO_2 in peridotites and pyroxenites from this study. Cr # is calculated as Cr/(Cr + Al) × 100 and Mg as Mg/(Mg + Fe) × 100. Also shown are data for spatially associated peridotites and pyroxenites from unpublished data and a literature compilation for these areas. The composition of spinel in DMM is from *Workman and Hart* [2005].

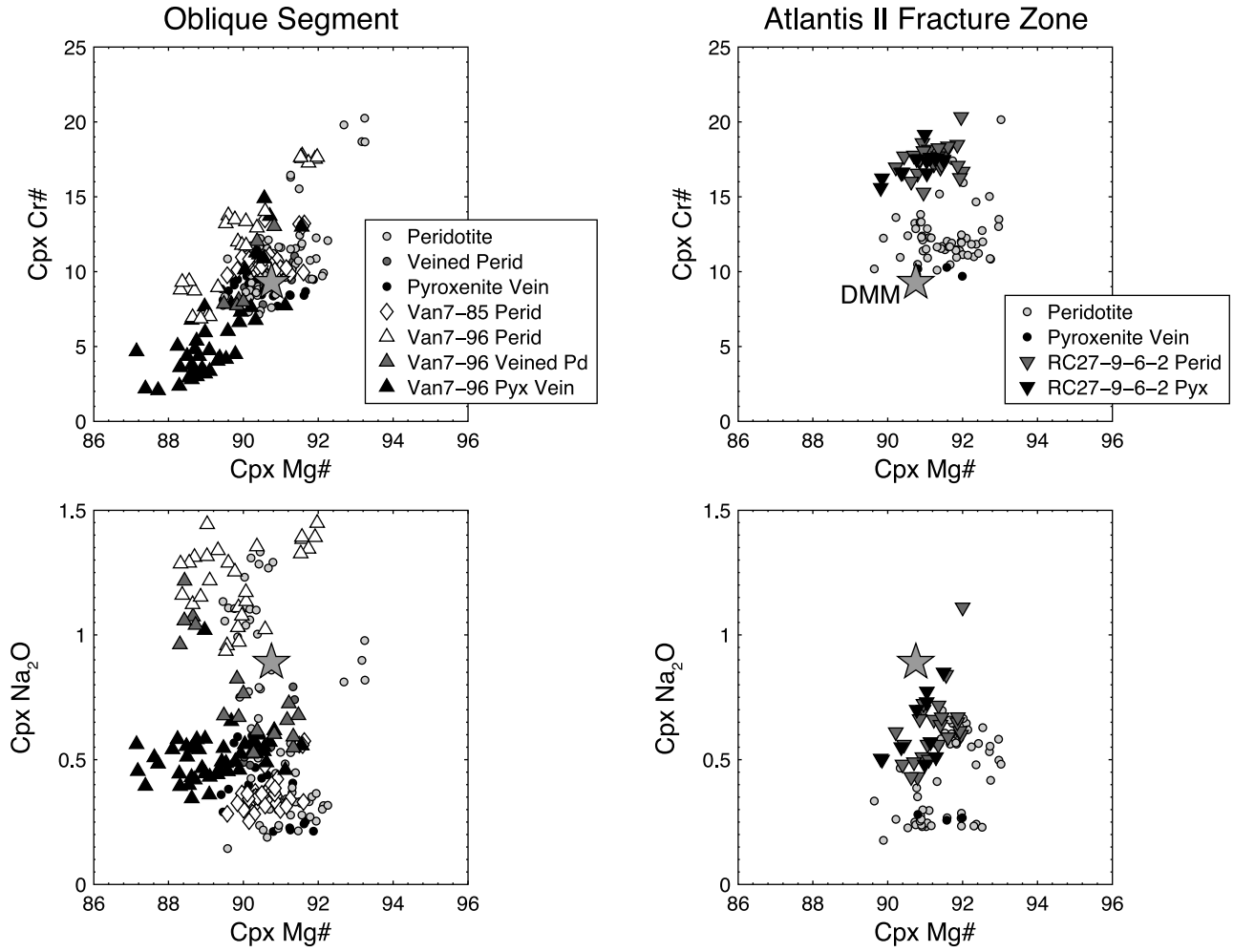

Figure A2. Variation of Mg # with Cr # and Na_2O in Cpx for peridotites and pyroxenites from this study and spatially associated samples (from a literature compilation and unpublished data). The composition of Cpx in DMM is from *Workman and Hart* [2005].

Witt-Eickschen and O'Neill data set. Our results also overlap the 1300–1400°C partition coefficients for the more compatible trace elements as modeled from lattice strain theory by *Lee et al.* [2007]. We have calculated temperatures for the abyssal peridotites using the *Brey and Köhler* [1990] geothermometers used by Witt-Eickschen and O'Neill and found a general range of 1050–1250°C. However, some samples have >200°C difference in temperature calculated using the Ca in Opx thermometer versus the Cpx/Opx thermometer. In addition, the difference between temperatures calculated for pyroxene cores and rims varies by a similar amount.

[120] As the Brey and Köhler thermometers depend on the CaO distribution in pyroxene, we compared pyroxene CaO to calculated partition coefficients for various trace elements. Whereas the Witt-Eickschen and O'Neill data set forms a linear array, the abyssal peridotites have a large range of pyroxene CaO values with limited variation in trace element partition coefficient. Overall, we found no systematic variation in the calculated temperatures or the measured pyroxene CaO contents of abyssal peridotites as a function of partition coefficients. We conclude that the xenoliths in the Witt-Eickschen and O'Neill data set are better at preserving mantle temperatures due to the fast transport of xenoliths to the surface, whereas the slow ascent of abyssal peridotites results in incomplete reequilibration of pyroxene compositions. However, we suggest that our measured partition coefficients require only a small amount of extrapolation to be applicable to temperatures relevant to mantle melting processes (~1350°C). Despite this extrapolation, our partition coefficients have the advantage over the Witt-Eickschen and O'Neill coefficients of being determined for pyroxene compositions relevant to the oceanic upper mantle.

[121] The second background data set plotted in Figure B1 is from *Hellebrand et al.* [2005] and consists of in situ ion microprobe analyses of abyssal peridotite pyroxenes. The Hellebrand et al. partition coefficients extend over a range of up to 2 orders of magnitude, with a larger range among the more incompatible elements. Most pyroxenes in abyssal peridotites exsolve a second pyroxene phase during their ascent to the seafloor, which redistributes the high-temperature trace element budget within the mineral. To account for exsolution lamellae, *Hellebrand et al.* [2005] applied correction factors to their partition coefficients, with larger corrections applied to the more incompatible elements. Application of their correction factors shifts their partition coefficients to higher temperature values, but does not reduce the overall

Table B1. Cpx/Opx Partition Coefficients

	Van7-85-42	Van7-85-47	Van7-85-49	Van7-96-09V	Van7-96-19M	Van7-96-21M	Van7-96-28	Van7-96-38	RC27-9-6-2M	Average[a]	Valence	Cpx IR[b] (Å)	Opx IR[b] (Å)
Pb			0.02			2.7	6.3			4.5	2	1.29	1.19
Sr			26	66	7.1	33	45	45	27	37	2	1.26	1.18
La				68	17	46	53		23	49	3	1.16	1.03
Ce				48	25	41	58	48	26	49	3	1.14	1.01
Pr				44	31	37	67	44	30	45	3	1.13	0.99
Nd	38	37		30	23	31	39	37	22	34	3	1.11	0.98
Sm	23	32	25	17	18	21	22	25	20	24	3	1.08	0.96
Eu	17	18	22	16	16	19	22	22	13	19	3	1.07	0.95
Gd	15	16	18	11	13	15	16	17	12	16	3	1.05	0.94
Th							23			23	4	1.05	0.94
Tb	11	11	14	7.7	10	12	14	14	9.5	12	3	1.04	0.92
Dy	8.5	9.2	11	5.4	8.7	9.3	10	10	7.0	9.6	3	1.03	0.91
Y	6.6	6.7	8.16	3.5	7.4	7.7	8.1	8.1	5.1	7.5	3	1.02	0.90
Ho	6.9	7.3	9.05	4.5	7.1	8.0	8.6	8.8	5.6	8.0	3	1.02	0.90
Er	5.7	5.5	7.12	3.6	6.0	6.3	6.8	6.9	4.9	6.3	3	1.00	0.89
U				2.2			10			10	4	1.00	0.89
Tm	4.4	4.2	5.41	2.7	4.9	5.0	5.1	5.5	3.7	4.9	3	0.99	0.88
Yb	3.7	3.5	4.43	2.3	4.1	4.1	4.6	4.6	3.1	4.2	3	0.99	0.87
Lu	3.0	3.0	3.69	1.8	3.4	3.2	3.7	3.7	2.7	3.4	3	0.98	0.86
Li	4.2	3.3	3.74	2.7	1.1	1.8	1.8	2.7	2.3	2.7	1	0.92	0.76
Zr		23						7.1	4.2	7.1	4	0.72	0.72
Hf	9.9	4.9	7.07					5.6	5.2	6.9	4	0.71	0.71
Nb	1.4	1.2							2.0	1.3	5	0.64	0.64

[a]Average does not include outliers or samples Van7-96-09V and RC27-9-6-2M.
[b]Ionic radii from *Shannon* [1976].

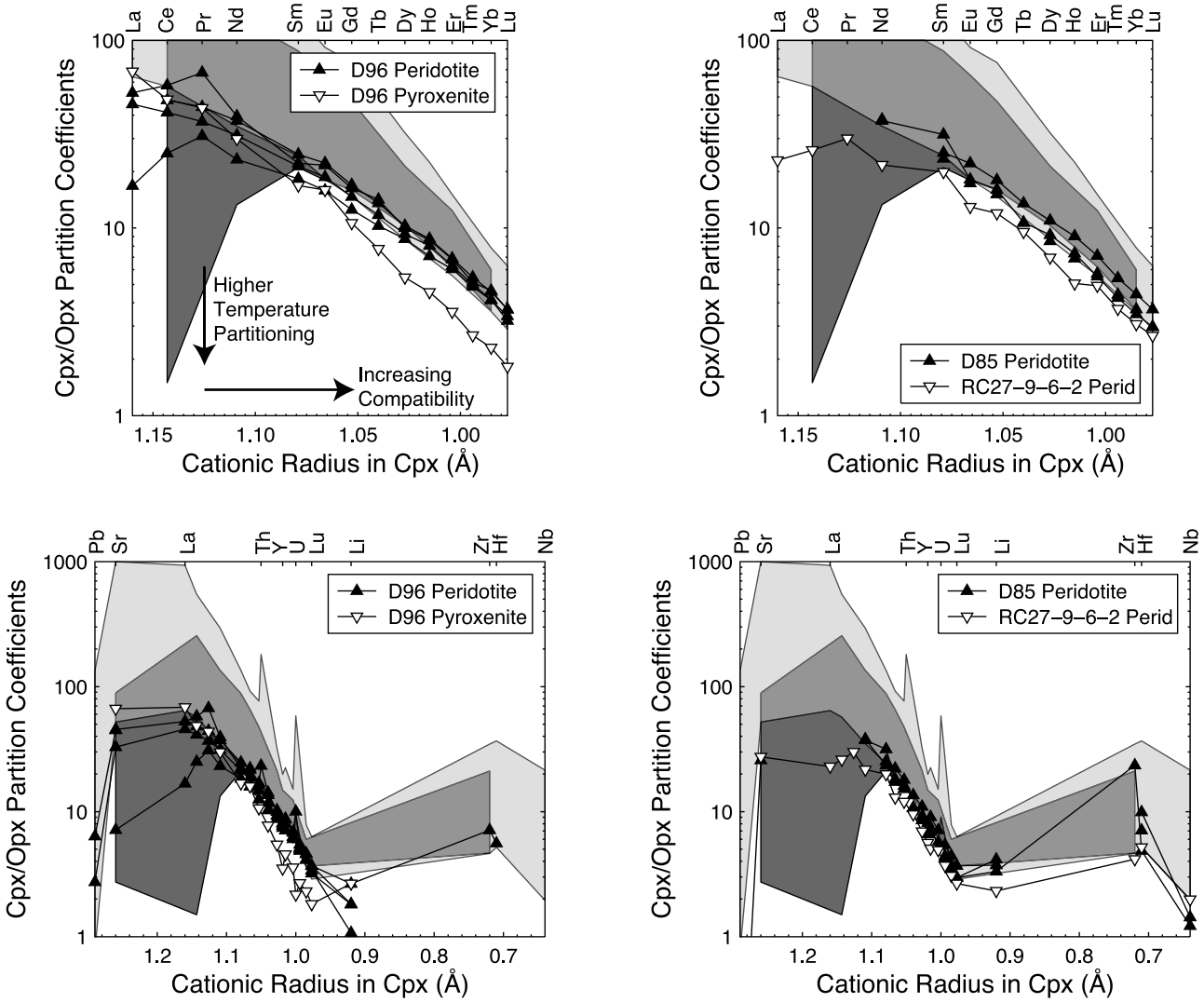

Figure B1. Cpx/Opx partition coefficients in abyssal peridotites, plus one pyroxenite, plotted as a function of cationic radius in Cpx. For the elements Pb to Li, this corresponds to eightfold coordination in the M2 sites whereas for the elements Zr-Nb, this corresponds to sixfold coordination in the M1 site. (top) REE variations are plotted; (bottom) the full set of trace elements are plotted. The light grey field is the partition coefficient range from *Witt-Eickschen and O'Neill* [2005] for xenoliths equilibrated over a range of temperatures from 900°C (high values) to 1250°C (low values). The dark grey field is the partition coefficient range for *Hellebrand et al.* [2005] from in situ analyses of abyssal peridotite pyroxenes.

range for a given element. We suggest that the large range is due to the difficulty of low concentration analyses on the 3f ion microprobe.

[122] In general, the partition coefficients that we measured vary smoothly as a function of ionic radius. The breaks in slope on the spidergram correspond to large changes in radius, changes in cation valence state, or changes in site occupancy (e.g., between Li and Zr, cations switch from M2 to M1 site occupancy). Only Pb, the most incompatible element, exhibits a large range of partition coefficients and appears to be relatively compatible in Opx. This may be due to measurement uncertainty or to sulfide microinclusions that control the Pb system. However, we note that *Witt-Eickschen and O'Neill* [2005] also observed similarly low Pb partition coefficients and they suggested that Pb might be more evenly distributed between Cpx and Opx than other elements.

[123] **Acknowledgments.** The authors thank Stan Hart, Glenn Gaetani, Peter Kelemen, Fred Frey, and Greg Hirth for reading earlier versions of this manuscript. Discussions with Laurent Montési, Jeff Standish, Matt Jackson, Mary Horan, and Vincent Salters provided helpful insights. Editorial handling by Patrick Taylor and Michael Bizimis and comments by two anonymous reviewers strengthened the manuscript. Yoshiko Nakano, Masako Uyama, and the members of PML are thanked for their hospitality during multiple visits to Misasa. Neel Chatterjee provided assistance with electron microprobe analyses. Martin Collier provided the MORB compilation for the global histogram plot. Maps were generated using GMT (http://gmt.soest.hawaii.edu/). This research was supported by WHOI Academic Programs funding to J.M.W; EAR0115433 and EAR0106578 to N.S; OCE9907630, OCE0526905, and OPP0425785 to H.J.B.D; and COE-21 funding to E.N.

References

Abelson, M., and A. Agnon (1997), Mechanics of oblique spreading and ridge segmentation, *Earth Planet. Sci. Lett.*, *148*, 405–421, doi:10.1016/S0012-821X(97)00054-X.

Allégre, C. J. (1968), Comportement des systèmes U-Th-Pb dans le manteau supérieur et modèle d'évolution de ce dernier au cours des temps géologiques, *Earth Planet. Sci. Lett.*, *5*, 261–269, doi:10.1016/S0012-821X(68)80050-0.

Allégre, C. J., and D. L. Turcotte (1986), Implications of a two-component marble-cake mantle, *Nature*, *323*, 123–127, doi:10.1038/323123a0.

Allégre, C. J., B. Hamelin, and B. Dupré (1984), Statistical analysis of isotopic ratios in MORB: The mantle blob cluster model and the convective regime of the mantle, *Earth Planet. Sci. Lett.*, *71*, 71–84, doi:10.1016/0012-821X(84)90053-0.

Barry, T. L., J. A. Pearce, P. T. Leat, I. L. Millar, and A. P. le Roex (2006), Hf isotope evidence for selective mobility of high-field-strength elements in a subduction setting: South Sandwich Islands, *Earth Planet. Sci. Lett.*, *252*, 223–244, doi:10.1016/j.epsl.2006.09.034.

Barth, M. G., R. L. Rudnick, I. Horn, W. F. McDonough, M. J. Spicuzza, J. W. Valley, and S. E. Haggerty (2001), Geochemistry of xenolithic eclogites from West Africa, part I: A link between low MgO eclogites and Archean crust formation, *Geochim. Cosmochim. Acta*, *65*(9), 1499–1527, doi:10.1016/S0016-7037(00)00626-8.

Batchelor, G. K. (1967), *An Introduction to Fluid Dynamics*, Cambridge Univ. Press, Cambridge, U. K.

Bizimis, M., G. Sen, V. J. M. Salters, and S. Keshav (2005), Hf-Nd-Sr isotope systematics of garnet pyroxenites from Salt Lake Crater, Oahu, Hawaii: Evidence for a depleted component in Hawaiian volcanism, *Geochim. Cosmochim. Acta*, *69*(10), 2629–2646, doi:10.1016/j.gca.2005.01.005.

Bown, J. W., and R. S. White (1994), Variation with spreading rate of oceanic crustal thickness and geochemistry, *Earth Planet. Sci. Lett.*, *121*, 435–449, doi:10.1016/0012-821X(94)90082-5.

Brandon, A. D., J. E. Snow, R. J. Walker, J. W. Morgan, and T. D. Mock (2000), ^{190}Pt-^{186}Os and ^{187}Re-^{187}Os systematics of abyssal peridotites, *Earth Planet. Sci. Lett.*, *177*, 319–335, doi:10.1016/S0012-821X(00)00044-3.

Brey, G. P., and T. Köhler (1990), Geothermobarometry in four-phase lherzolites ii. new thermobarometers, and practical assessment of existing thermobarometers, *J. Petrol.*, *31*(6), 1353–1378.

Brunelli, D., M. Seyler, A. Cipriani, L. Ottolini, and E. Bonatti (2006), Discontinuous melt extraction and weak refertilization of mantle peridotites at the Vema Lithospheric Section (Mid-Atlantic Ridge), *J. Petrol.*, *47*(4), 745–771, doi:10.1093/petrology/egi092.

Burton, K. W., P. Schiano, J.-L. Birck, and C. J. Allègre (1999), Osmium isotope disequilibrium between mantle minerals in a spinel-lherzolite, *Earth Planet. Sci. Lett.*, *172*, 311–322, doi:10.1016/S0012-821X(99)00207-1.

Cannat, M., D. Sauter, A. Bezos, C. Meyzen, E. Humler, and M. Le Rigoleur (2008), Spreading rate, spreading obliquity, and melt supply at the ultraslow spreading Southwest Indian Ridge, *Geochem. Geophys. Geosyst.*, *9*, Q04002, doi:10.1029/2007GC001676.

Cherniak, D. J., and Y. Liang (2007), Rare Earth element diffusion in natural enstatite, *Geochim. Cosmochim. Acta*, *71*, 1324–1340, doi:10.1016/j.gca.2006.12.001.

Cipriani, A., H. K. Brueckner, E. Bonatti, and D. Brunelli (2004), Oceanic crust generated by elusive parents: Sr and Nd isotopes in basalt-peridotite pairs from the Mid-Atlantic Ridge, *Geology*, *32*(8), 657–660, doi:10.1130/G20560.1.

Constantin, M., R. Hékinian, D. Ackermand, and P. Stoffers (1995), Mafic and ultramafic intrusions into upper mantle peridotites from fast spreading centers of the Easter Microplate (South East Pacific), in *Mantle and Lower Crust Exposed in Oceanic Ridges and in Ophiolites*, edited by R. L. M. Vissers and A. Nicolas, pp. 71–120, Kluwer Acad., Dordrecht, Netherlands.

Coogan, L. A., G. M. Thompson, C. J. MacLeod, H. J. B. Dick, S. J. Edwards, A. Hosford Scheirer, and T. L. Barry (2004), A combined basalt and peridotite perspective on 14 million years of melt generation at the Atlantis Bank segment of the Southwest Indian Ridge: Evidence for temporal changes in mantle dynamics, *Chem. Geol.*, *207*, 13–30, doi:10.1016/j.chemgeo.2004.01.016.

Dantas, C., G. Ceuleneer, M. Gregoire, M. Python, R. Freydier, J. Warren, and H. J. B. Dick (2007), Pyroxenites from the Southwest Indian Ridge, 9–16°E: Cumulates from incremental melt fractions produced at the top of a cold melting regime, *J. Petrol.*, *48*(4), 647–660, doi:10.1093/petrology/egl076.

DePaolo, D. J., and G. J. Wasserburg (1976), Inferences about magma sources and mantle structure from variations of ^{143}Nd/^{144}Nd, *Geophys. Res. Lett.*, *3*(12), 743–746, doi:10.1029/GL003i012p00743.

Dick, H. J. B. (1989), Abyssal peridotites, very slow spreading ridges and ocean ridge magmatism, in *Magmatism in the Ocean Basins*, edited by A. D. Saunders and M. J. Norry, *Geol. Soc. Spec. Publ.*, *42*, 71–105, doi:10.1144/GSL.SP.1989.042.01.06.

Dick, H. J. B., and T. Bullen (1984), Chromian spinel as a petrogenetic indicator in abyssal and alpine-type peridotites and spatially associated lavas, *Contrib. Mineral. Petrol.*, *86*, 54–76, doi:10.1007/BF00373711.

Dick, H. J. B., R. L. Fisher, and W. B. Bryan (1984), Mineralogic variability of the uppermost mantle along mid-ocean ridges, *Earth Planet. Sci. Lett.*, *69*, 88–106, doi:10.1016/0012-821X(84)90076-1.

Dick, H. J. B., et al. (1991), Tectonic evolution of the Atlantis II Fracture Zone, *Proc. Ocean Drill. Program, Sci. Results*, *118*, 359–398.

Dick, H. J. B., J. Lin, and H. Schouten (2003), An ultraslow-spreading class of ocean ridge, *Nature*, *426*, 405–412, doi:10.1038/nature02128.

Dosso, L., H. Bougault, C. Langmuir, C. Bollinger, O. Bonnier, and J. Etoubleau (1999), The age and distribution of mantle heterogeneity along the Mid-Atlantic Ridge (31–41°N), *Earth Planet. Sci. Lett.*, *170*, 269–286, doi:10.1016/S0012-821X(99)00109-0.

Faure, G., and T. M. Mensing (2005), *Isotopes: Principles and Applications*, 3rd ed., John Wiley, Hoboken, N. J.

Frey, F. A., and M. Prinz (1978), Ultramafic inclusions from San Carlos, Arizona: Petrologic and geochemical data bearing on their petrogenesis, *Earth Planet. Sci. Lett.*, *38*, 129–176, doi:10.1016/0012-821X(78)90130-9.

Galer, S. J. G. (1999), Optimal double and triple spiking for high precision lead isotopic measurement, *Chem. Geol.*, *157*, 255–274, doi:10.1016/S0009-2541(98)00203-4.

Hamelin, B., and C. J. Allègre (1985), Large-scale regional units in the depleted upper mantle revealed by an isotope study of the South-West Indian Ridge, *Nature*, *315*, 196–199, doi:10.1038/315196a0.

Hamelin, B., and C. J. Allègre (1988), Lead isotope study of orogenic lherzolite massifs, *Earth Planet. Sci. Lett.*, *91*, 117–131, doi:10.1016/0012-821X(88)90155-0.

Hamelin, B., G. Manhes, F. Albarede, and C. J. Allègre (1985), Precise lead isotope measurements by the double spike technique: A reconsideration, *Geochim. Cosmochim. Acta*, *49*, 173–182, doi:10.1016/0016-7037(85)90202-9.

Hart, S. R. (1984), A large-scale isotope anomaly in the Southern Hemisphere mantle, *Nature*, *309*, 753–757, doi:10.1038/309753a0.

Hart, S. R., and C. Brooks (1970), Rb-Sr mantle evolution models, *Year Book Carnegie Inst. Washington*, *68*, 426–429.

Hart, S. R., J.-G. Schilling, and J. L. Powell (1973), Basalts from Iceland and along the Reykjanes Ridge: Sr isotope geochemistry, *Nature Phys. Sci.*, *246*, 104–107.

Hart, S. R., J. Blusztajn, H. J. B. Dick, P. S. Meyer, and K. Muehlenbachs (1999), The fingerprint of seawater circulation in a 500-meter section of ocean crust gabbros, *Geochim. Cosmochim. Acta*, *63*(23–24), 4059–4080, doi:10.1016/S0016-7037(99)00309-9.

Hartnady, C. J. H., and A. P. le Roex (1985), Southern Ocean hotspot tracks and the Cenozoic absolute motion of the African, Antarctic, and South American plates, *Earth Planet. Sci. Lett.*, *75*, 245–257, doi:10.1016/0012-821X(85)90106-2.

Harvey, J., A. Gannoun, K. W. Burton, N. W. Rogers, O. Alard, and I. J. Parkinson (2006), Ancient melt extraction from the oceanic upper mantle revealed by Re-Os isotopes in abyssal peridotites form the Mid-Atlantic Ridge, *Earth Planet. Sci. Lett.*, *244*, 606–621, doi:10.1016/j.epsl.2006.02.031.

Hellebrand, E., J. E. Snow, S. Mostefaoui, and P. Hoppe (2005), Trace element distribution between orthopyroxene and clinopyroxene in peridotites from the Gakkel Ridge: A SIMS and NanoSIMS study, *Contrib. Mineral. Petrol.*, *150*, 486–504, doi:10.1007/s00410-005-0036-5.

Hirschmann, M. M., and E. M. Stolper (1996), A possible role for garnet pyroxenite in the origin of the "garnet signature" in MORB, *Contrib. Mineral. Petrol.*, *124*, 185–208, doi:10.1007/s004100050184.

Hofmann, A. W. (1988), Chemical differentiation of the Earth: The relationship between mantle, continental crust, and oceanic crust, *Earth Planet. Sci. Lett.*, *90*, 297–314, doi:10.1016/0012-821X(88)90132-X.

Hofmann, A. W. (1997), Mantle geochemistry: The message from oceanic volcanism, *Nature*, *385*, 219–229, doi:10.1038/385219a0.

Holm, P. M. (2002), Sr, Nd and Pb isotopic composition of in situ lower crust at the Southwest Indian Ridge: Results from ODP Leg 176, *Chem. Geol.*, *184*, 195–216, doi:10.1016/S0009-2541(01)00364-3.

Hosford, A., M. Tivey, T. Matsumoto, H. Dick, H. Schouten, and H. Kinoshita (2003), Crustal magnetization and accretion at the Southwest Indian Ridge near the Atlantis II fracture zone, 0–25 Ma, *J. Geophys. Res.*, *108*(B3), 2169, doi:10.1029/2001JB000604.

Ishikawa, A., T. Kuritani, A. Makishima, and E. Nakamura (2007), Ancient recycled crust beneath the Ontong Java Plateau: Isotopic evidence from garnet clinopyroxenite xenoliths, Malaita, Solomon Islands, *Earth Planet. Sci. Lett.*, *259*, 134–148, doi:10.1016/j.epsl.2007.04.034.

Jacob, D., E. Jagoutz, D. Lowry, D. Mattey, and G. Kudrjavtseva (1994), Diamondiferous eclogites from Siberia: Remnants of Archean oceanic crust, *Geochim. Cosmochim. Acta*, *58*(23), 5191–5207, doi:10.1016/0016-7037(94)90304-2.

Janney, P. E., A. P. le Roex, and R. W. Carlson (2005), Hafnium isotope and trace element constraints on the nature of mantle heterogeneity beneath the central Southwest Indian Ridge (13°E to 47°E), *J. Petrol.*, *46*(12), 2427–2464, doi:10.1093/petrology/egi060.

Johnson, K. T. M., and H. J. B. Dick (1992), Open system melting and temporal and spatial variation of peridotite and basalt at the Atlantis II Fracture Zone, *J. Geophys. Res.*, *97*(B6), 9219–9241, doi:10.1029/92JB00701.

Johnson, K. T. M., H. J. B. Dick, and N. Shimizu (1990), Melting in the oceanic upper mantle: An ion microprobe study of diopsides in abyssal peridotites, *J. Geophys. Res.*, *95*, 2661–2678, doi:10.1029/JB095iB03p02661.

Juteau, T., E. Berger, and M. Cannat (1990), Serpentinized, residual mantle peridotites from the M. A. R. median valley, ODP Hole 670A (21°10′N, 45°02′W, Leg 109): Primary mineralogy and geothermometry, *Proc. Ocean Drill. Program Sci. Results*, *106/109*, 27–45.

Kelemen, P. B., G. M. Yogodzinski, and D. W. Scholl (2003), Along-strike variation in lavas of the Aleutian island arc: Implications for the genesis of high Mg andesite and the continental crust, in *The Subduction Factory*, *Geophys. Monogr. Ser.*, vol. 138, edited by J. Eiler, pp. 223–276, AGU, Washington, D. C.

Kellogg, J. B., S. B. Jacobsen, and R. J. O'Connell (2002), Modeling the distribution of isotopic ratios in geochemical reservoirs, *Earth Planet. Sci. Lett.*, *204*, 183–202, doi:10.1016/S0012-821X(02)00981-0.

Kempton, P. D., and C. J. Stephens (1997), Petrology and geochemistry of nodular websterite inclusions in harzburgite, Hole 920D, *Proc. Ocean Drill. Program Sci. Results*, *153*, 321–331.

Kempton, P. D., C. J. Hawkesworth, and M. Fowler (1991), Geochemistry and isotopic composition of gabbros from layer 3 of the Indian Ocean crust, Hole 735B, *Proc. Ocean Drill. Program, Sci. Results*, *118*, 127–143.

Kobayashi, K., R. Tanaka, T. Moriguti, K. Shimizu, and E. Nakamura (2004), Lithium, boron and lead isotope systematics of glass inclusions in olivines from Hawaiian lavas: Evidence for recycled components in the Hawaiian plume, *Chem. Geol.*, *212*, 143–161, doi:10.1016/j.chemgeo.2004.08.050.

Kumagai, H., H. J. B. Dick, and I. Kaneoka (2003), Noble gas signatures of abyssal gabbros and peridotites at an Indian Ocean core complex, *Geochem. Geophys. Geosyst.*, *4*(12), 9107, doi:10.1029/2003GC000540.

Kuritani, T., and E. Nakamura (2002), Precise isotope analysis of nanogram-level Pb use of double spikes, *Chem. Geol.*, *186*, 31–43, doi:10.1016/S0009-2541(02)00004-9.

Kuritani, T., and E. Nakamura (2003), Highly precise and accurate isotopic analysis of small amounts of Pb using ^{205}Pb-^{204}Pb and ^{207}Pb-^{204}Pb, two double spikes, *J. Anal. At. Spectrom.*, *18*, 1464–1470, doi:10.1039/b310294g.

Kurz, M. D., A. P. le Roex, and H. J. B. Dick (1998), Isotope geochemistry of the oceanic mantle near the Bouvet triple junction, *Geochim. Cosmochim. Acta*, *62*(5), 841–852, doi:10.1016/S0016-7037(97)00383-9.

Langmuir, C. H., E. M. Klein, and T. Plank (1992), Petrological systematics of mid-ocean ridge basalts: Constraints on melt generation beneath ocean ridges, in *Melt Flow and Melt Generation at Mid-Ocean Ridges*, *Geophys. Monogr. Ser.*, vol. 71, edited by J. Phipps Morgan, D. K. Blackman, and J. M. Sinton, pp. 183–280, AGU, Washington, D. C.

Lee, C.-T. A., A. Harbert, and W. P. Leeman (2007), Extension of lattice strain theory to mineral/mineral rare-Earth element partitioning: An approach for assessing disequilibrium and developing internally consistent partition coefficients between olivine, orthopyroxene, clinopyroxene and basaltic melt, *Geochim. Cosmochim. Acta*, *71*, 481–496, doi:10.1016/j.gca.2006.09.014.

Lee, K.-L. (1997), Petrological and geochemical studies of an abyssal peridotite from the Atlantis II Fracture Zone, M.S. thesis, MIT/WHOI Joint Program, Woods Hole, Mass.

Lehnert, K., Y. Su, C. H. Langmuir, B. Sarbas, and U. Nohl (2000), A global geochemical database structure for rocks, *Geochem. Geophys. Geosyst.*, *1*(5), 1012, doi:10.1029/1999GC000026.

le Roex, A. P., H. J. B. Dick, A. J. Erlank, A. M. Reid, F. A. Frey, and S. R. Hart (1983), Geochemistry, mineralogy and petrogenesis of lavas erupted along the Southwest Indian Ridge between the Bouvet Triple Junction and 11°East, *J. Petrol.*, *24*(3), 267–318.

le Roex, A. P., H. J. B. Dick, and R. T. Watkins (1992), Petrogenesis of anomalous K-enriched MORB from the Southwest Indian Ridge: 11°53′E to 14°38′E, *Contrib. Mineral. Petrol.*, *110*, 253–268, doi:10.1007/BF00310742.

Ligi, M., et al. (1997), Death and transfiguration of a triple junction in the South Atlantic, *Science*, *276*, 243–245, doi:10.1126/science.276.5310.243.

Liu, C.-Z., J. E. Snow, E. Hellebrand, G. E. Brügmann, A. B. von der Handt, and A. W. Hofmann (2008), Ancient, highly heterogeneous mantle beneath Gakkel ridge, Arctic Ocean, *Nature*, *452*, 311–316, doi:10.1038/nature06688.

Lugmair, G. W., and R. W. Carlson (1978), The Sm-Nd history of KREEP, *Proc. Lunar Planet. Sci. Conf.*, *9th*(1), 689–704.

Maclennan, J. (2008), Lead isotope variability in olivine-hosted melt inclusions from Iceland, *Geochim. Cosmochim. Acta*, *72*, 4159–4176, doi:10.1016/j.gca.2008.05.034.

Mahoney, J. J., J. H. Natland, W. M. White, R. Poreda, S. H. Bloomer, R. L. Fisher, and A. N. Baxter (1989), Isotopic and geochemical provinces of the western Indian Ocean spreading centers, *J. Geophys. Res.*, *94*(B4), 4033–4052, doi:10.1029/JB094iB04p04033.

Mahoney, J., A. P. le Roex, Z. Peng, R. L. Fisher, and J. H. Natland (1992), Southwestern limits of Indian Ocean ridge mantle and the origin of low ^{206}Pb/^{204}Pb mid-ocean ridge basalt: Isotope systematics of the central Southwest Indian Ridge (17°–50°E), *J. Geophys. Res.*, *97*(B13), 19,771–19,790, doi:10.1029/92JB01424.

Makishima, A., and E. Nakamura (1997), Suppression of matrix effects in ICP-MS by high power operation of ICP: Application to precise determination of Rb, Sr, Y, Cs, Ba, REE, Pb, Th and U at ng g^{-1} levels in milligram silicate samples, *Geostand. Newsl.*, *21*(2), 307–319, doi:10.1111/j.1751-908X.1997.tb00678.x.

Makishima, A., and E. Nakamura (2006), Determination of major, minor and trace elements in silicate samples by ICP-QMS and ICP-SFMS applying isotope dilution-internal standardisation (ID-IS) and multi-stage internal standardisation, *Geostand. Geoanal. Res.*, *30*, 245–271, doi:10.1111/j.1751-908X.2006.tb01066.x.

Makishima, A., E. Nakamura, and T. Nakano (1999), Determination of zirconium, niobium, hafnium and tantalum at ng g^{-1} levels in geological materials by direct nebulisation of sample HF solution into FI-ICP-MS, *Geostand. Newsl.*, *23*(1), 7–20, doi:10.1111/j.1751-908X.1999.tb00555.x.

McDonough, W. F., and F. A. Frey (1989), Rare Earth elements in upper mantle rocks, in *Geochemistry and Mineralogy of Rare Earth Elements*, *Rev. Mineral.*, vol. 21, edited by B. R. Lipin and G. A. McKay, pp. 99–145, Mineral. Soc. of Am., Reston, Va.

McDonough, W. F., and S. Sun (1995), The composition of the Earth, *Chem. Geol.*, *120*, 223–253, doi:10.1016/0009-2541(94)00140-4.

McKenzie, D. P. (1969), Speculations on the consequences and causes of plate motions, *Geophys. J. R. Astron. Soc.*, *18*, 1–32.

Meyzen, C. M., J. N. Ludden, E. Humler, B. Luais, M. J. Toplis, C. Mével, and M. Storey (2005), New insights into the origin and distribution of the DUPAL isotope anomaly in the Indian Ocean mantle from MORB of the Southwest Indian Ridge, *Geochem. Geophys. Geosyst.*, *6*, Q11K11, doi:10.1029/2005GC000979.

Meyzen, C. M., J. Blichert-Toft, J. N. Ludden, E. Humler, C. Mével, and Albarède (2007), Isotopic portrayal of the Earth's upper mantle flow field, *Nature*, *447*, 1069–1074, doi:10.1038/nature05920.

Montési, L. G. J., and M. D. Behn (2007), Mantle flow and melting underneath oblique and ultraslow mid-ocean ridges, *Geophys. Res. Lett.*, *34*, L24307, doi:10.1029/2007GL031067.

Morgan, W. J. (1983), Hotspot tracks and the early rifting of the Atlantic, *Tectonophysics*, *94*, 123–139, doi:10.1016/0040-1951(83)90013-6.

Morishita, T., J. Maeda, S. Miyashita, H. Kumagai, T. Matsumoto, and H. J. B. Dick (2007), Petrology of local concentration of chromian spinel in dunite from the slow-spreading Southwest Indian Ridge, *Eur. J. Mineral.*, *19*, 871–882, doi:10.1127/0935-1221/2007/0019-1773.

Mukasa, S. B., J. W. Shervais, H. G. Wilshire, and J. E. Nielson (1991), Intrinsic Nd, Pb and Sr isotopic heterogeneities exhibited by the Lherz Alpine Peridotite Massif, French Pyrenees, *J. Petrol.*, Special Lherzolites Issue, 117–134.

Nakamura, E., A. Makishima, T. Moriguti, K. Kobayashi, C. Sakaguchi, T. Yokoyama, R. Tanaka, T. Kuritani, and H. Takei (2003), Comprehensive geochemical analyses of small amounts (<100 mg) of extraterrestrial samples for the analytical competition related to the sample return mission MUSES-C, *Tech. Rep. SP 16*, Inst. of Space and Astron. Sci., Sagamihara, Japan.

O'Nions, R. K., and R. J. Pankhurst (1974), Petrogenetic significance of isotope and trace element variations in volcanic rocks from the Mid-Atlantic, *J. Petrol.*, *15*(3), 603–634.

O'Nions, R. K., P. J. Hamilton, and N. M. Evensen (1977), Variations in ^{143}Nd/^{144}Nd and ^{87}Sr/^{86}Sr ratios in oceanic basalts, *Earth Planet. Sci. Lett.*, *34*, 13–22, doi:10.1016/0012-821X(77)90100-5.

Pearson, D. G., G. R. Davies, and P. H. Nixon (1993), Geochemical constraints on the petrogenesis of diamond facies pyroxenites from the Beni Bousera Peridotite Massif, north Morocco, *J. Petrol.*, *34*(1), 125–172.

Phipps Morgan, J., and W. J. Morgan (1999), Two-stage melting and the geochemical evolution of the mantle: A recipe for mantle plum-pudding, *Earth Planet. Sci. Lett.*, *170*, 215–239, doi:10.1016/S0012-821X(99)00114-4.

Piccardo, G. B., B. Messiga, and R. Vannucci (1988), The Zabargad peridotite-pyroxenite association: Petrological constraints on its evolution, *Tectonophysics*, *150*, 135–162, doi:10.1016/0040-1951(88)90299-5.

Polvé, M., and C. J. Allègre (1980), Orogenic lherzolite complexes studied by ^{87}Rb-^{87}Sr: A clue to understand the mantle convection processes?, *Earth Planet. Sci. Lett.*, *51*, 71–93, doi:10.1016/0012-821X(80)90258-7.

Prestvik, T., S. Goldberg, and G. G. Goles (1999), Petrogenesis of the volcanic suite of Bouvetøya (Bouvet Island), South Atlantic, *Nor. Geol. Tidsskr.*, *79*, 205–218, doi:10.1080/002919699433663.

Python, M., and G. Ceuleneer (2003), Nature and distribution of dykes and related melt migration structures in the mantle section of the Oman ophiolite, *Geochem. Geophys. Geosyst.*, *4*(7), 8612, doi:10.1029/2002GC000354.

Reid, I., and H. R. Jackson (1981), Oceanic spreading rate and crustal thickness, *Mar. Geophys. Res.*, *5*, 165–172.

Saal, A. E., S. R. Hart, N. Shimizu, E. H. Hauri, and G. D. Layne (1998), Pb isotopic variability in melt inclusions from oceanic island basalts, Polynesia, *Science*, *282*, 1481–1484, doi:10.1126/science.282.5393.1481.

Salters, V. J. M., and H. J. B. Dick (2002), Mineralogy of the mid-ocean-ridge basalt source from neodymium isotopic composition of abyssal peridotites, *Nature*, *418*, 68–72, doi:10.1038/nature00798.

Salters, V. J. M., and A. Stracke (2004), Composition of the depleted mantle, *Geochem. Geophys. Geosyst.*, *5*, Q05B07, doi:10.1029/2003GC000597.

Serri, G., R. Hébert, and R. Hekinian (1988), Petrology of a plagioclase-bearing olivine websterite from the Gorringe Bank (northeastern Atlantic Ocean), *Can. J. Earth Sci.*, *25*, 557–569.

Seyler, M., M. Cannat, and C. Mével (2003), Evidence for major-element heterogeneity in the mantle source of abyssal peridotites from the Southwest Indian Ridge (52° to 68°E), *Geochem. Geophys. Geosyst.*, *4*(2), 9101, doi:10.1029/2002GC000305.

Seyler, M., J.-P. Lorand, M. J. Toplis, and G. Godard (2004), Asthenospheric metasomatism beneath the mid-ocean ridge: Evidence from depleted abyssal peridotites, *Geology*, *32*(4), 301–304, doi:10.1130/G20191.1.

Shannon, R. D. (1976), Revised effective ionic radii and systematic studies of interatomic distances in halides and chalcogenides, *Acta Crystallogr., Sect. A Cryst. Phys. Diffr. Theor. Gen. Crystallogr.*, *32*, 751–767, doi:10.1107/S0567739476001551.

Shervais, J. W., and S. B. Mukasa (1991), The Balmuccia Orogenic Lherzolite Massif, Italy, *J. Petrol.*, Special Lherzolite Issue, 155–174.

Shimizu, N., and G. D. Layne (2003), Large local heterogeneities of the MORB source mantle: Melt inclusion Pb isotope studies, *Geochim. Cosmochim. Acta*, *67*, A431.

Shimizu, N., K. Kobayashi, T. Sisson, G. Layne, E. Nakamura, and M. Kurz (2005), Evolution of diverse mantle sources for the Kilauea Volcano over 270 ka, *Eos Trans. AGU*, *86*(52), Fall Meet. Suppl., Abstract V22A-07.

Sleep, N. H. (1975), Formation of oceanic crust: Some thermal constraints, *J. Geophys. Res.*, *80*(29), 4037–4042, doi:10.1029/JB080i029p04037.

Sneeringer, M., S. R. Hart, and N. Shimizu (1984), Strontium and samarium diffusion in diopside, *Geochim. Cosmochim. Acta*, *48*, 1589–1608, doi:10.1016/0016-7037(84)90329-6.

Snow, J. E. (1993), The isotope geochemistry of abyssal peridotites and related rocks, Ph.D. thesis, MIT/WHOI Jt. Program, Woods Hole, Mass.

Snow, J. E., S. R. Hart, and H. J. B. Dick (1994), Nd and Sr isotope evidence linking mid-ocean-ridge basalts and abyssal peridotites, *Nature*, *371*, 57–60, doi:10.1038/371057a0.

Standish, J. J. (2006), The influence of ridge geometry at the ultraslow-spreading Southwest Indian Ridge (9°–25°E): Basalt composition sensitivity to variations in source and process, Ph.D. thesis, MIT/WHOI Jt. Program, Woods Hole, Mass.

Standish, J. J., H. J. B. Dick, P. J. Michael, W. G. Melson, and T. O'Hearn (2008), MORB generation beneath the ultraslow spreading Southwest Indian Ridge (9–25°E): Major element chemistry and the importance of process versus source, *Geochem. Geophys. Geosyst.*, *9*, Q05004, doi:10.1029/2008GC001959.

Stolper, E. (1980), A phase diagram for mid-ocean ridge basalts: Preliminary results and implications for petrogenesis, *Contrib. Mineral. Petrol.*, *74*, 13–27, doi:10.1007/BF00375485.

Su, Y., and C. H. Langmuir (2003), Global MORB chemistry compilation at the segment scale, Ph.D. thesis, Dep. of Earth and Environ. Sci., Columbia Univ., New York.

Sun, S.-S. (1980), Lead isotopic study of young volcanic rocks from mid-ocean ridges, ocean islands and island arcs, *Philos. Trans. R. Soc. London, Ser. A*, *297*, 409–445, doi:10.1098/rsta.1980.0224.

Tanaka, R., A. Makishima, H. Kitagawa, and E. Nakamura (2003), Suppression of Zr, Nb, Hf and Ta coprecipitation in flouride compounds for determination in Ca-rich materials, *J. Anal. At. Spectrom.*, *18*, 1458–1463, doi:10.1039/b309948b.

Taylor, S. R., and S. M. McLennan (1995), The geochemical evolution of the continental crust, *Rev. Geophys.*, *33*(2), 241–265, doi:10.1029/95RG00262.

Todt, W., R. A. Cliff, A. Hanser, and A. W. Hofmann (1996), Evaluation of a ^{202}Pb-^{205}Pb double spike for high-precision lead isotope analysis, in *Earth Processes: Reading the Isotopic Code*, *Geophys. Monogr. Ser.*, vol. 95, edited by A. Basu and S. Hart, pp. 429–437, AGU, Washington, D. C.

van Keken, P. E., E. H. Hauri, and C. J. Ballentine (2002), Mantle mixing: The generation, preservation, and destruction of chemical heterogeneity, *Annu. Rev. Earth Planet. Sci.*, *30*, 493–525, doi:10.1146/annurev.earth.30.091201.141236.

Van Orman, J. A., T. L. Grove, and N. Shimizu (2001), Rare Earth element diffusion in diopside: Influence of temperature, pressure, ionic radius, and an elastic model for diffusion in silicates, *Contrib. Mineral. Petrol.*, *141*, 687–703.

Van Orman, J. A., T. L. Grove, N. Shimizu, and G. D. Layne (2002), Rare Earth element diffusion in a natural pyrope single crystal at 2.8 GPa, *Contrib. Mineral. Petrol.*, *142*, 416–424.

White, W. M., and A. W. Hofmann (1982), Sr and Nd isotope geochemistry of oceanic basalts and mantle evolution, *Nature*, *296*, 821–825, doi:10.1038/296821a0.

Witt-Eickschen, G., and H. S. C. O'Neill (2005), The effect of temperature on the equilibrium distribution of trace elements between clinopyroxene, orthopyroxene, olivine and spinel in upper mantle peridotite, *Chem. Geol.*, *221*, 65–101, doi:10.1016/j.chemgeo.2005.04.005.

Workman, R. K., and S. R. Hart (2005), Major and trace element composition of the depleted MORB mantle (DMM), *Earth Planet. Sci. Lett.*, *231*, 53–72, doi:10.1016/j.epsl.2004.12.005.

Yoshikawa, M., and E. Nakamura (1993), Precise isotope determination of trace amounts of Sr in magnesium-rich samples, *J. Mineral. Petrol. Econ. Geol.*, *88*, 548–561.

Zindler, A., and S. Hart (1986), Chemical geodynamics, *Annu. Rev. Earth Planet. Sci.*, *14*, 493–571, doi:10.1146/annurev.ea.14.050186.002425.

Zindler, A., H. Staudigel, S. R. Hart, and S. Goldstein (1983), Nd and Sr isotopic study of a mafic layer from Ronda ultramafic complex, *Nature*, *304*, 226–230, doi:10.1038/304226a0.

H. J. B. Dick and N. Shimizu, Department of Geology and Geophysics, Woods Hole Oceanographic Institution, Woods Hole, MA 02543, USA.

E. Nakamura and C. Sakaguchi, Institute for Study of the Earth's Interior, Okayama University at Misasa, Misasa, Tottori 682-0193, Japan.

J. M. Warren, Department of Terrestrial Magnetism, Carnegie Institution of Washington, 5241 Broad Branch Rd., NW, Washington, DC 20015, USA. (jwarren@dtm.ciw.edu)